PhD Dissertation

Compressive Sensing Applied to High Resolution Imaging by Synthetic Aperture Radar

（コンプレッシブ・センシングによる
合成開口レーダの高分解能化）

Submitted to
Graduate School of Environmental Studies
Tohoku University

by
RIAFENI KARLINA

Supervised by

Prof. Motoyuki Sato

Dissertation Committee
Prof. Motoyuki Sato (Tohoku Univ.)
Prof. Hiroshi Asanuma (Tohoku Univ.)
Prof. Hiroshi Takahashi (Tohoku Univ.)
Prof. Akira Hirose (The Univ. of Tokyo)

August, 2013

Table of Contents

List of Abbreviations

AGC	: Automatic Gain Control	
ALIS	: Advanced Landmine Imaging System	
BPF	: Band Pass Filter	
CoSaMP	: Compressed Sampling Matching Pursuit	
CPU	: Central Processing Unit	
CS	: Compressive Sensing	
FFT	: Fast Fourier Transform	
GB-SAR	: Ground-Based Synthetic Aperture Radar	
GPR	: Ground Penetrating Radar	
IFFT	: Inverse Fast Fourier Transform	
ISAR	: Inverse Synthetic Aperture Radar	
LS	: Least Square	
MD	: Metal Detector	
MIMO	: Multi Input Multi Output	
ML	: Marginal Likelihood	
OMP	: Orthogonal Matching Pursuit	
POD	: Probability of Detection	
RVM	: Relevance Vector Machine	
SAR	: Synthetic Aperture Radar	
SCR	: Signal to Clutter Ratio	
SFCW	: Stepped-Frequency Continuous Wave	
VNA	: Vector Network Analyzer	

List of Figures

List of Tables

1. Introduction

1.1.   Research Background

Sensing and compression is a common process in many aspect of modern life. Sensing is a process of acquiring information from a source, for example the mechanism in a digital camera to acquire the value of each pixel in the image. To get accurate and good information, there are many requirements in sensing process. In digital data processing, a Nyquist criterion requires that a signal is sampled at least by twice the maximum frequency of the signal. In most cases, this resulted in a huge amount of data, which is make it difficult for further processing or require huge memory for saving.

The solution for this problem is given by compression. Many researches in signal processing found that most of the signal can be represented in another form where it has a sparse or compressible representation, by transform coding. By sparse signal it means that most of the information in the signal is contained in a very small number of its components. The rest of the signal components contain less or no information, that it can be discarded without significant loss of information. By keeping only the values and the location of its largest components, the signal can be transformed back to its original form without loss of information. This process is very common in file (e.g. image, audio and video) compression, and wireless communication. The example of transform coding schemes includes JPEG, JPEG2000, MP3, and MPEG [1].
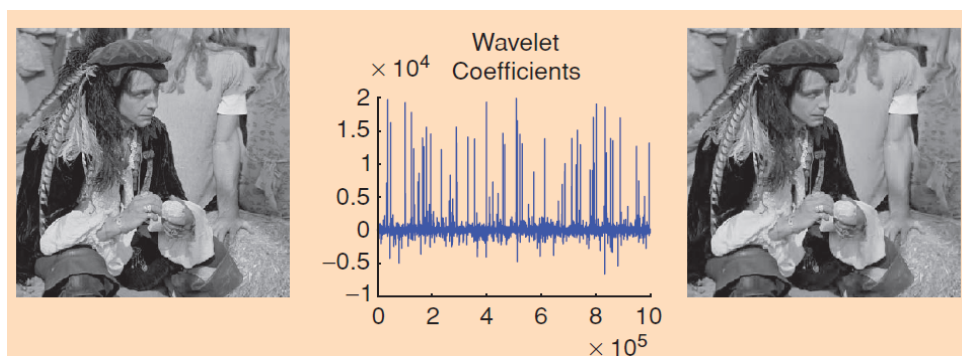
Fig. 1.1. Compression of an image by wavelet coding [2]

Fig. 1.1 shows an example of image compression by using the wavelet transform. The image in the left side shows the original image, and the middle image shows the wavelet coefficients of the image. It is shown that only a small number of wavelet coefficients have large values, while most of the coefficients have small values around zero. Thus this image can be regarded as a compressible signal. The figure on the right side shows the reconstructed image by using only 2.5% of the largest wavelet coefficients. Compared to the original image, the reconstructed image does not show significant degradation of the quality.

The explained sensing and compression process has been able to solve the data storage and data transfer problem. However, there are still some problems in the implementation. First, the system still requires the dense sampling during the data acquisition. Second, it requires huge computation resources to calculate all the coefficients of the signal in its sparse representation, eventhough most of the coefficients with small values will be discarded later. And third, the components with large values must be saved or transferred together with their locations, that requires extra memory for storage or bandwidth resource in data transmission.
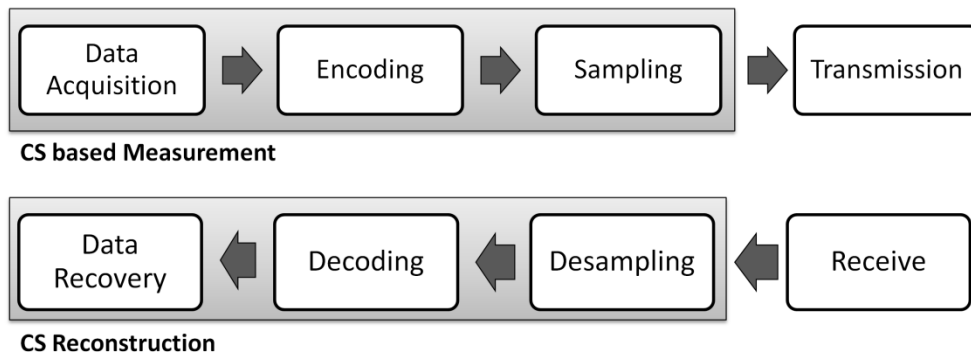
Fig. 1.2. Traditional sensing-compression process and CS system

An advancement in signal processing found that the sampling can be directly performed during the data acquisition for the signal which has sparse representation in another domain. This new technology is known as Compressive Sensing (CS). Fig. 1.2 shows the comparison between the traditional sensing and compression process with the CS system. It is shown that CS system combined the three steps, i.e. data acquisition, encoding and sampling, in a single step by directly acquiring the sampled data during measurement. This will reduce the requirement during the data acquisition and reduce computation burden for coding the signal. By using CS, the number of sample needed

during measurement can be reduced, even much lower than traditionally required by Nyquist sampling criterion. Eventhough the number of sample is very small, the full information can be approximated by exploiting the sparsity of the signal. CS theory has been widely implemented in many applications, such as single pixel camera [3], MRI image reconstruction [4]-[5], channel estimation in wireless communication [6]-[7] and radar imaging [8].

In this study, the implementation of CS is evaluated for the application in Synthetic Aperture Radar (SAR). The fundamental purpose of a SAR system is to image the target located in the imaging area. Therefore, if the target is small compared to the whole imaging area, the SAR imaging can be regarded as a sparse problem where the implementation of CS is highly possible. This thesis discusses the implementation of CS for SAR system, including Ground Based-SAR (GB-SAR) and Ground Penetrating Radar (GPR)

1.2. Synthetic Aperture Radar

Synthetic Aperture Radar (SAR) system is a radar system that synthesizes a large aperture antenna from the antenna scanning to derive high resolution radar image. A large aperture antenna is needed in order to acquire high azimuth resolution of a radar image. However, a large aperture antenna will cause high manufacture and operational cost. SAR system solve this problem by using smaller aperture antenna with wider beam, acquiring radar signal along a survey line and performing SAR processing to generate a focused radar image.
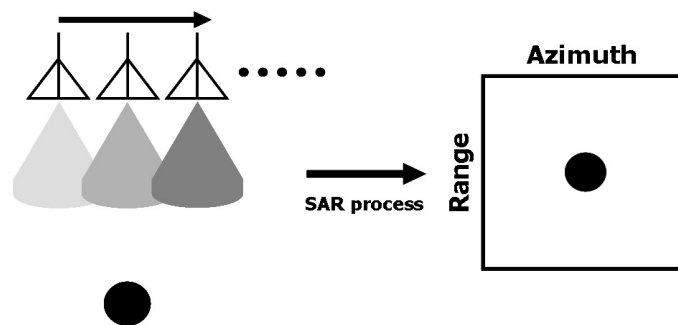
Fig. 1.3. Conceptual Sketch of SAR [9]

Using Fourier based SAR image reconstruction, the azimuth resolution of the radar system can be increased significantly compared to real aperture radar. The azimuth

resolution is given by (1.1), with ρ_{az} is the azimuth resolution in SAR system, and D is the size of the aperture antenna used in the SAR system. This equation shows that in SAR system, the azimuth resolution is not dependent on the distance between the sensor and the target. And, unlike real aperture radar system, in SAR system, the smaller aperture antenna with wide beam will give finer azimuth resolution in the radar image.

$$\rho_{az} = D\!\!\diagup\!\!_2 \qquad\qquad (1.1)$$

The range resolution of a SAR system is dependent on the bandwidth of the system, as given by (1.2). To acquire finer range resolution, the wider bandwidth is required, leads to a huge amount of data and a longer data acquisition time during measurement.

$$\Delta R = \frac{v}{2B} \qquad\qquad (1.2)$$

SAR system has been applied for airborne and spaceborne remote sensing, GB-SAR and GPR. This thesis will focus on the GB-SAR which is used for observation of the target on the ground, and GPR which is used for subsurface observation.

1.3. Nyquist Sampling Criterion

In order to acquire high quality SAR image and to avoid the spatial aliasing problem, the SAR measurement has to satisfy several requirements given by the Nyquist sampling theorem. The radar data has to be acquired at equally spaced observation points and the spatial space has to be less or equal the half of the minimum wavelength of the radar signal [10]. This requirement is shown in (1.3), with Δx is the maximum distance between two data acquisition points and $\lambda_{\min}$ is the minimum wavelength of the signal.

If the measurement violates these requirements, the SAR image will have poor resolution and may generate artifacts in the image.

$$\Delta x \le \frac{\lambda_{\min}}{2} \qquad\qquad (1.3)$$

There are many kinds of waveform that can be used in radar system, such as impulse, chirp, Frequency Modulated Continuous Wave (FMCW), and Stepped Frequency Continuous Wave (SFCW). In this thesis, the SAR system is implemented on SFCW radar. In SFCW radar, narrowband signal is transmitted sequentially with the increment of frequency in each transmition. The reflected signal for each narrowband signal is recorded and is processed to form the radar image. Therefore, the frequency response measured by SFCW radar is sampled in frequency domain with a sampling interval Δf. In this situation, the Nyquist sampling criterion needs to be satisfy for unambiguous reconstruction, as given in (1.4), with v is the wave velocity in the medium, and R_m is the required unambiguous range in the radar image.

$$\Delta f < \frac{v}{2R_m} \tag{1.4}$$

To acquire high range resolution, the radar signal needs to have a large bandwidth resulting in a large number of the frequency information that needs to be measured. The large bandwidth also resulted in the higher value of the maximum frequency in the signal, then the minimum wavelength of the signal will be smaller. This will cause the Nyquist theorem to require more dense spatial data and become more difficult to satisfied. For example, in GPR survey with the wave velocity in the subsurface is 0.12m/ns and frequency range of the SFCW signal is 100 MHz to 6 GHz, the required spatial space is about 1 cm. This requirement will lead to long data acquisition time, especially in 3D survey, where the B-scan should be repeated for every 1 cm offset. For 1m by 1m survey, the B-scan should be repeated for 100 times, which is a lot of work and time.

1.4. Research Objectives

As has been explained in the previous section, SAR system required some strict requirements in order to produce high quality radar image. In addition, the data acquisition process itself is not easy, especially for the case of GPR survey. The traditional Nyquist theory required that the data is acquired at a gridded position which is difficult to perform in real measurement. GPR survey usually uses an odometer to guide the antenna movement, so it will move in a straight line. But in reality, the accuracy of this system is not good, it is difficult to make the antenna move in a perfectly straight line. An improvement is made by using the high accuracy positioning

system, for example the Rotary Laser Positioning System (RLPS), GPS, Total Station, etc, to accurately record the position of the antenna during the data acquisition [11]. However, eventhough the accurate position is now available, after data acquisition, the data is usually interpolated to acquire a gridded data, before performing migration process.

By implementing CS to SAR system, not only the cost of the data acquisition can be reduced, the problem of ungridded data can also be solved. CS based SAR system can directly produce SAR image by using randomly acquired data, so there is no need to make the antenna move in a straight line and also no need to do interpolation to make a gridded data.

However, compared to the conventional SAR imaging, CS has some problems, especially in GPR application. CS system is very sensitive to noise and clutter which usually high in GPR application. It is also sensitive to inaccurate estimation of wave velocity in the medium, which is usually cannot be perfectly known in GPR applications. Another problem is if the target is not exactly a point target, it is observed that CS cannot reconstruct the perfect shape and size of the target, which cause difficulty in interpreting the nature of the target. This can cause a problem of implementing CS for landmine detection, since it is difficult to differentiate the reflection of a landmine from the reflection of other objects.

Thus, the main objective of this thesis is to:
1. Investigate the implementation of CS for SAR system and optimizing the data acquisition method and CS algorithm for a detection of a specific known target.
2. Propose model based CS to acquire better image reconstruction and characterization in landmine detection case.

1.5. Content of Thesis

The structure of the thesis is shown in Fig. 1.4. In chapter one, the research background is presented. This chapter discusses the SAR system and conventional sampling requirement for high resolution image reconstruction. The advantages and limitations of the implementation of CS to SAR system has also been presented, which leads to the objective of this research to improve the performance of CS-SAR system.

Chapter 2 introduces the basic theory of CS and the implementation of CS for 2-dimensional image reconstruction by SAR system. The derivation of the representation matrix and the sampling schemes for CS-SAR system is discussed. The existing algorithms to solve CS problem is also presented. The performance of CS system is validated by using an example of CS reconstruction using a laboratory experiment with GB-SAR system.

Chapter 3 presents the implementation of CS for 2-dimensional scan GB-SAR system to reconstruct 3D radar image. The motivation of this work is because CS implementation in 2D survey is much more advantageous in reducing the work and time during data acquisition. The performance of CS reconstruction using convex programming is discussed, including the important parameter such as the number of sample, the noise parameter, and the processing time.

Chapter 4 discussed the implementation of CS for the detection and localization of subsurface target using GPR system. This chapter explained the difficulty of image reconstruction in GPR system, which is highly distorted by noise, clutter, signal attenuation and the inaccurate estimation of wave velocity in the medium. In order to mitigate the problem, a new data acquisition technique which main purpose to reduce the spatial sampling is proposed. A modified CS algorithm based on Bayesian learning is also proposed for the detection of a specific known target.

Chapter 5 discussed the implementation of CS to landmine detection. A model based CS which works by exploiting the signal characteristic is proposed to improve the image reconstruction by CS especially for landmine detection case. The landmine is modeled as a group of several pixels with large values. The proposed algorithm is validated using laboratory experiment and real data sets from a landmine field in Cambodia.

Finally chapter 6 summarizes the preceding chapters and presents recommendations for further improvement of the research work.
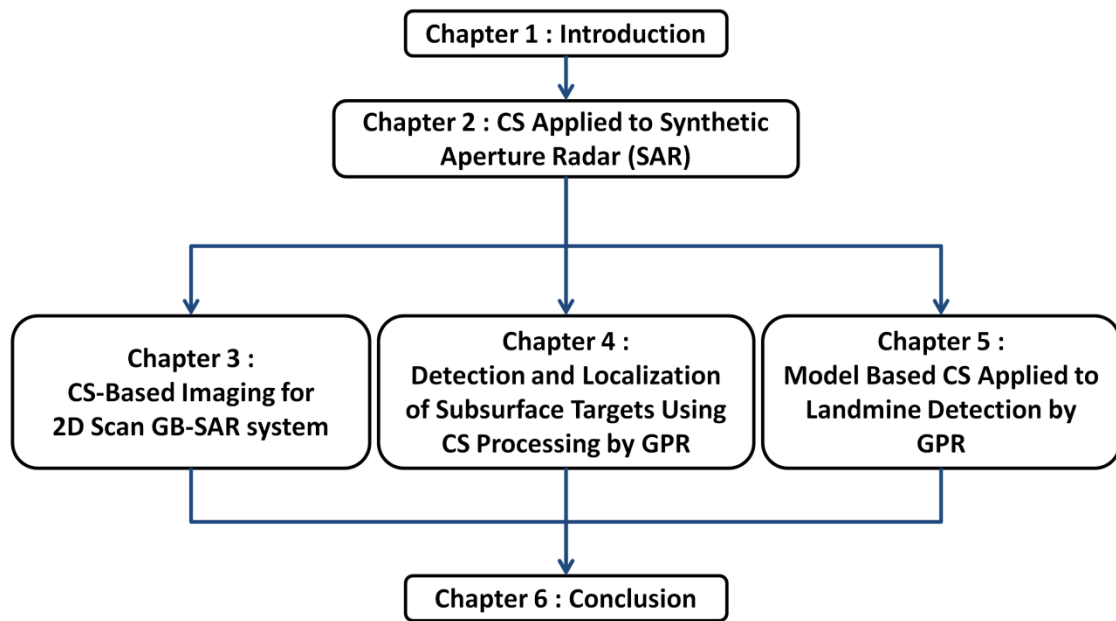
Fig. 1.4. Structure of this thesis

2. Compressive Sensing Applied to Synthetic Aperture Radar

2.1. Introduction

The theory of CS has been clearly explained in [2],[12]-[14]. Based on the CS theory, the possibility of applying CS to radar imaging has been investigated in some papers. Yoon *et al* [15] and Huang *et al* [16] showed that CS could be applied for a through-wall radar imaging system. Lagunas *et al* [17] presented an improvement in CS based through-wall radar imaging by developing a joint wall mitigation and CS processing for indoor image reconstruction. Ahmad *et al* [18] applied change detection to CS framework for the detection and localization of human targets using the through-wall radar imaging.

Several other studies on CS application for SAR systems have also been conducted. Zhu *et al* proposed a CS approach to SAR tomography (TomoSAR) in [19] and developed a CS-based spectral estimation algorithm for spaceborne tomographic SAR application in [20]. Budillon *et al* [21] proposed a 3D SAR imaging method based on CS for multipass SAR signals. It is shown that the number of required measurement can be reduced since the image to be focused has usually a sparse representation along the elevation direction. Xilong *et al* [22] demonstrated the applicability of CS implementation for three dimensional SAR imaging using a real SAR datasets. Yang *et al* [23] proposed a random-frequency SAR imaging scheme based on CS. It is demonstrated that the proposed method can overcome the limitation of the available imaging range width in conventional stepped-frequency techniques for SAR, while maintaining the range and azimuth resolution of the image.

The implementation of CS has also been investigated as a solution to improve resolution in ISAR (Inversed Synthetic Aperture Radar) imaging. In conventional ISAR imaging, the observing interval should be long enough so that high cross-range resolution can be obtained by coherent processing. This resolution is dependent on both the Coherent Processing Interval (CPI) and target rotational motion [24]. However, during ISAR data acquisition, long CPI may be unachievable since the target usually uncooperative and

maneuvering. And during long CPI, target-motion compensation should be more complex due to nonuniformly rotating motion and fluctuation of reflection characteristics with respect to the viewing angle change [25]. Therefore, an imaging technique using CS is proposed by Zhang *et al* [24] to acquire high cross-range resolution in ISAR with very limited measurement data during short CPI. An improved algorithm is proposed in [25] to increase the performance of CS-based high resolution ISAR imaging to overcome strong noise and clutter in ISAR data. Wang *et al* [26] proposed to adopt CS for ISAR imaging not only in the cross-range direction, but also in range direction which enable high range resolution imaging by transmitting only a few probing frequencies instead of a wideband signal.

Another implementation of CS is proposed for Multiple-Input Multiple Output (MIMO) radar system by Y. Yu *et al* [27]. Assuming the targets are sparsely located in the angle-Doppler space, the superior resolution of MIMO radar with far fewer samples can be achieved by CS processing. In [28], Y. Yu *et al* proposed an optimal measurement matrix design for MIMO radar imaging to improve the detection performance offered by the random Gaussian measurement matrix typically used in CS problem. C.Y. Chen *et al* [29] proposed a waveform design method for MIMO radar to reduce the correlation between target responses, because small correlation between the target responses is required to effectively reconstruct the target scene by CS techniques. And a CSSF MIMO radar (Compressive-Sensing and Step-Frequency Based MIMO) is proposed by Y. Yu *et al* in [30]. This approach applies the technique of step frequency to CS based MIMO radar, which enables high resolution range, angle and Doppler estimation while transmitting narrowband pulses.

The implementation of CS for SFCW GPR system has been demonstrated by Gurbuz *et al* [31] and Suksmono *et al* [32]. These studies proved through simulation and experiment that CS can recover the GPR image with higher resolution and less clutter than the conventional processing with much less measurement. Several interesting approaches to further increase the performance of CS system have also been published, such as the use of the radon transform to increase the target sparsity in line structure detection using GPR system [33]. And Tuncer *et al* proposed a method to remove ground reflection using the sampled frequency measurement data in a CS GPR system [34].

The possibility to expand and improve the implementation of CS in radar imaging field

is still widely possible. However, in order to be able to expand and improve the implementation of CS to radar imaging, it is important to understand the fundamental theory of CS. This chapter provides some basic explanations about the CS theory and how to implement the CS theory in image reconstruction by SAR.

2.2.   Compressive Sensing

Compressive sensing is an advance signal processing with the purpose to recover full information from a very small number of measurements. [2] explains two requirements for CS to work. First, the signal should be sparse in one domain and the measurement is conducted in another transform domain. Sparse signal means a signal that has a very small number of high value components, while the other components are zeros or negligible.

The sparse basis or the representation matrix is defined as the relation between the signal in the measurement domain with the signal in its sparse domain. If s is the full signal to be measured, and α is the same signal represented in the sparse domain, then Ψ is the sparse basis or representation matrix.

$$s = \Psi \alpha \qquad (2.1)$$

The second requirement is the incoherency between the sampling matrix and the representation basis. The sampling process is performed by selecting some samples of the signal in its measurement domain. Or mathematically, the sampling process is performed by multiplying each side of the equation (2.1) with a sampling matrix Φ, as shown in (2.2). In (2.2), y is defined as the sampled measurement data. It can be concluded that for CS to work, α should be sparse and Φ should be incoherent with Ψ.

$$y = \Phi s = \Phi \Psi \alpha \qquad (2.2)$$

CS finds solution by exploiting the sparsity of the signal, by searching for the sparsest solution among the possible solutions. Methematically, CS finds solution by minimizing ℓ_0 norm as shown in (2.3). ℓ_0 norm simply calculates the number of the non-zero components of a variable, as written in (2.4)

$$\min \|\boldsymbol{\alpha}\|_0 \text{ subject to } \boldsymbol{y} = \boldsymbol{\Phi\Psi\alpha} \tag{2.3}$$

$$\|\boldsymbol{\alpha}\|_0 = \sum_i 1_{\alpha_i \neq 0} \tag{2.4}$$

Fig. 2.1(a) shows an example of a sparse signal in frequency domain ($F(\omega)$). This signal can be transformed to time domain ($f(t)$) shown in Fig. 2.1(b), where the information is scattered at all time. In CS based measurement, the measurement is conducted in time domain, the sparsity is in frequency domain, and the representation matrix is given by the Fourier transform.

Fig. 2.2 shows an example of signal reconstruction by CS. Suppose there are some sparse samples in time domain shown with black dots in Fig. 2.2(a). There are many possible solutions in reconstructing the full signal, for example the signal shown with a solid line (i.e. solution 1) and the signal shown with a dashed line (i.e. solution 2). However, solution 1 has sparse representation in frequency domain, while the solution 2 has frequency components scattered at many frequencies. Therefore, CS chooses the solution 1 as a solution, since it is the sparsest solution.

(a)   (b)
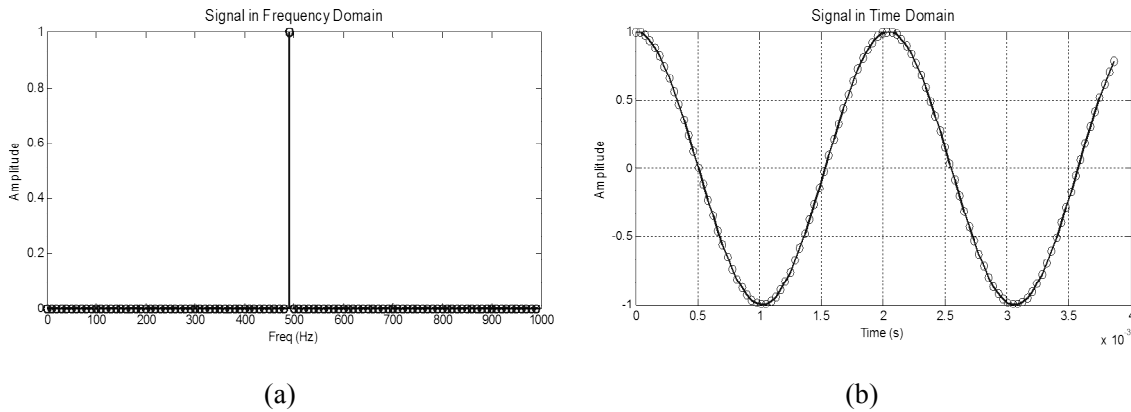
Fig. 2.1. (a) Signal in frequency domain, (b) Signal in time domain

(a)

(b)

(c)
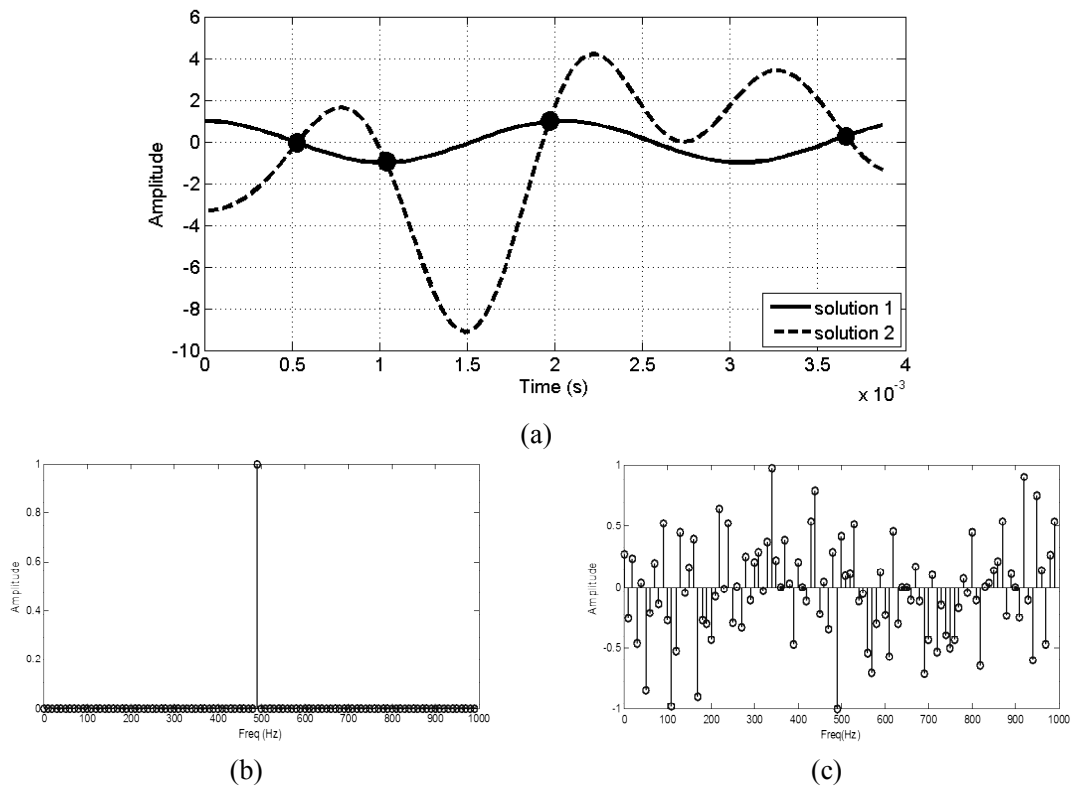
Fig. 2.2 Example of signal reconstruction by CS. (a) Samples in time domain, shown by black dots, and two possible solutions, (b) Frequency domain representation of solution 1, (c) Frequency domain representation of solution 2

The importance of incoherent sampling can be explained by an example shown in Fig. 2.3. In this example, the signal is uniformly sampled in time domain, shown with the black dots. Both of the two possible solutions have sparse representation in frequency domain. Therefore, in this case, CS cannot find the solution.

This example shows the importance of incoherent sampling in CS reconstruction. The incoherency makes sure that the chosen samples can provide the unlikeliness between possible solutions in CS reconstruction. It is straightforward that uniform sampling does not satisfy the incoherency requirement, since by uniform sampling, the signal with double frequency cannot be differentiate.

The problem may arise of how to choose the incoherent sampling matrix during the measurement. Fortunately, the CS theory stated that a random matrix is incoherent with any basis matrix Ψ with high probability. This theorem leads to the easy implementation of CS in real applications, since we only need to do random sampling

13

during the measurement.
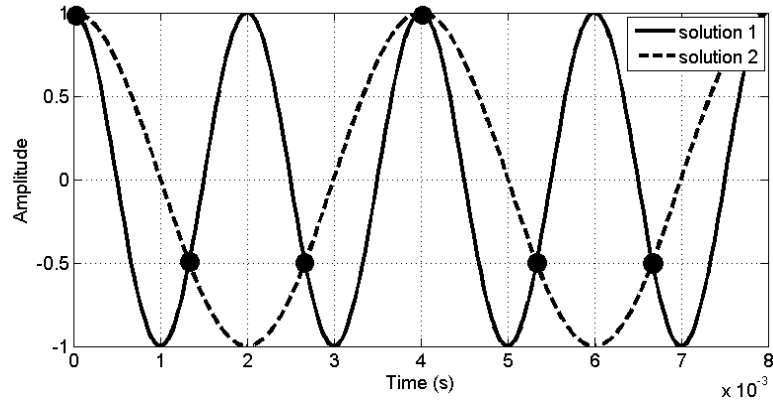
(a)
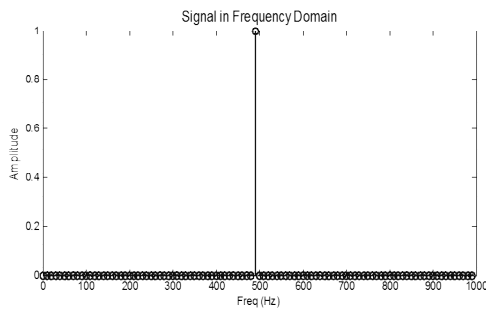
(b)
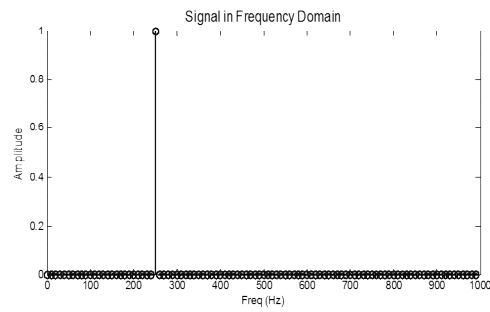
(c)

Fig. 2.3. Example of failed signal reconstruction by CS. (a) Signal with uniform sampling and two possible solutions, (b) Frequency domain representation of solution 1, (c) Frequency domain representation of solution 2

2.3.   Implementation of CS to SAR Imaging

SAR system works by transmitting an electromagnetic wave and recording the reflected wave from the object target in the observed area. This process is performed at several observation points along the survey line. And by conventional processing, the separation between each observation points has to satisfy Nyquist criterion.

The electromagnetic wave reflected by a target with reflection coefficient σ is the delayed version of the transmitted wave, as given by

$$s_r = \sigma A \exp(-jkr) \tag{2.5}$$

14

with A is the strength of the transmitted signal, s_r is the received wave, k is the propagation constant, and r is the two way propagation distance from the Tx antenna to the target and from the target to the Rx antenna.

For an SFCW radar signal, the reflected signal is observed at several frequency points. The received signal at m-th frequency point is given by (2.6), with τ is the two way propagation delay.

$$s_r(m) = \sigma A \exp(-jk_m r) = \sigma A \exp\left(-j\frac{2\pi f_m}{v} r\right)$$

$$s_r(m) = \sigma A \exp(-j2\pi f_m \tau)$$

(2.6)
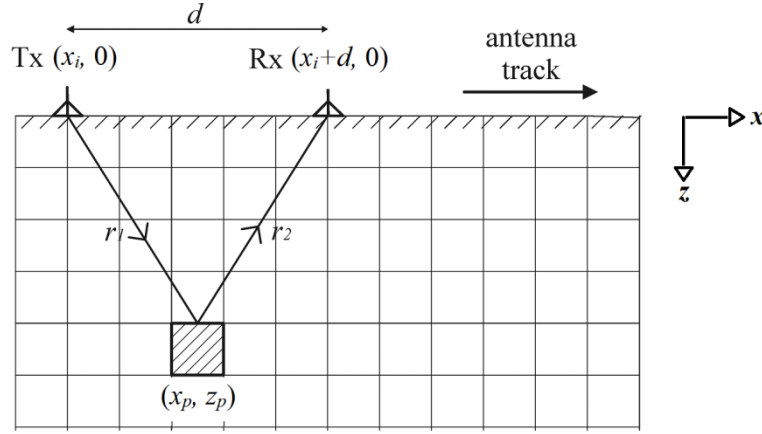
Fig. 2.4. The coordinate definition of antennas and the imaged pixel during image reconstruction in SAR system

In SAR system, the SFCW data is acquired at a number of observation points along the survey line. Consider a condition shown in Fig. 2.4, where Tx and Rx antennas are located in x axis, separated by a distance d, and the SAR data is acquired along the x axis. The received SAR data is sampled at both spatial and frequency domain as specified by (2.7).

$$s_r(i,m) = \sigma \exp(-j2\pi f_m \tau_i)$$

(2.7)

for $0 \leq m \leq M-1$, where $s_r(i,m)$ is the signal received at the the m-th frequency point and the antenna is located at the i-th scan position (x_i). σ is the reflection coefficient of the target, and τ is the propagation delay between the target and the antenna, and M is the number of frequency points used in SFCW signal.

Propagation delay (τ) is defined by (2.8), with r is the two way propagation distance between the transmitter antenna to the target located at (x_t, z_t) and from the target to the receiver antenna. c is the signal propagation velocity in the air ($c = 3 \times 10^8$ m/s) and d is the separation between transmitter and receiver antenna.

$$\tau_i = r_i / c$$

$$r_i = r_1 + r_2 = \sqrt{(x_t - x_i)^2 + (z_p)^2} + \sqrt{(x_t - x_i - d)^2 + (z_p)^2} \tag{2.8}$$

The SAR image can be reconstructed by dividing the imaging area into several pixels with proper resolution as shown in Fig. 2.4. The electromagnetic reflectivity in each pixel can be calculated using Fourier based SAR processing as shown in (2.9).

$$p(x_p, z_p) = \frac{1}{NM} \sum_{i=0}^{N-1} \sum_{m=0}^{M-1} s_r(i, m) \exp(-j2\pi f_m r_{i,p} / c) \tag{2.9}$$

for $0 \le x_p \le N_x^p - 1$, and $0 \le z_p \le N_z^p - 1$, with N_x^p and N_z^p is the total number of pixel in x and z direction. $p(x_p, z_p)$ is the estimation of electromagnetic reflectivity of the object located at pixel (x_p, z_p) in SAR image, $s_r(i, m)$ is the signal received when the antenna is located at (x_i) and the m-th frequency point, N is the number of observation points and M is the number of frequency points. With the antenna track as a reference ($z = 0$), $r_{i,p}$ is the propagation distance between transmitter antenna at position $(x_i, 0)$ to the pixel at position (x_p, z_p) and from the pixel to the receiver antenna at position $(x_i + d, 0)$, with d is the separation distance between the transmitter and receiver antenna.

The pixel which contains a target will have high p value. Otherwise for the pixel which contains no target, p should have zero value. If the size of the target is much smaller than the whole imaging area, only small amount of pixels have high p value, then p is a sparse matrix. Therefore, CS can be applied for this imaging problem.

2.3.1. Representation Matrix

The first step to implement CS to SAR imaging is to define the measurement domain and the sparse domain of the signal. The representation matrix can be defined as the relation between these two variables. In SAR imaging, the signal is measured in spatial-frequency domain, given by a two dimensional s_r matrix. And as explained before, the sparse signal is given by the electromagnetic reflectivity of each pixels, given by a two dimensional p matrix. The representation matrix Ψ can be derived from the relation between s_r and p.

$$s_r = \Psi p \qquad (2.10)$$

To be able to define Ψ, the two dimensional s_r and p matrices should be transformed into a one column vector by concatenating their column. Using the resulted one column vectors, Ψ can be derived, as shown in (2.13).

$$s_r = [s_r(1,1); s_r(2,1); ...; s_r(N,1); s_r(1,2); s_r(2,2); ...; s_r(N,M)] \qquad (2.11)$$

$$p = [p(1,1); p(2,1); ...; p(N_x^p,1); p(1,2); p(2,2); ...; p(N_x^p, N_z^p)] \qquad (2.12)$$

$$\Psi(k,l) = \exp(-2\pi f_k \tau_{k,l}) \qquad (2.13)$$

Since s_r and p has been transformed into one column vectors, we need to define which frequency is used in the k-th column of s_r $\left(f_k\right)$, the antenna position corresponding to the k-th column of s_r $\left(x_i^k, 0\right)$, and the pixel position corresponding to the l-th column of p $\left(x_p^l, y_p^l, z_p^l\right)$, as given below, with $\lceil a \rceil = \text{ceiling}(a)$, which gives the smallest integer greater than or equal to a.

$$f_k = f\left(\left\lceil \frac{k}{N} \right\rceil\right) \qquad (2.14)$$

$$\tau_{k,l} = \left(\sqrt{\left(x_p^l - x_i^k\right)^2 + z_p^{l\,2}} + \sqrt{\left(x_p^l - x_i^k - d\right)^2 + z_p^{l\,2}}\right) \Big/ c \qquad (2.15)$$

17

$$x_p^l = x_p\left(l - \left(N_x^p\left(\left\lceil l/N_x^p \right\rceil - 1\right)\right)\right) \tag{2.16}$$

$$z_p^l = z_p\left(\left\lceil \frac{l}{N_x^p} \right\rceil\right) \tag{2.17}$$

$$x_i^k = x_i^k = x_i\left(k - \left(N\left(\left\lceil k/N \right\rceil - 1\right)\right)\right) \tag{2.18}$$

2.3.2. Sampling Matrix

The selection of sampling matrix is an important step in CS processing, because it is required that the sampling matrix should be incoherent with the sparse basis. Fig. 2.5 shows two examples of sampling schemes that can be used in SFCW radar measurement. The vertical axis shows the antenna position along the survey line, and the horizontal axis shows the frequency points. The black box shows the selected measurement data to be used in CS processing.

Sampling scheme 1 shown in Fig. 2.5(a) is a random matrix, where the observation points and frequency points are randomly selected. It has been known that a random matrix is incoherent with any sparse basis with high probability. But by using this sampling scheme, even though the number of data is highly reduced, the number of the observation points is not significantly reduced. In radar system, reducing the observation points is more crucial in reducing the data acquisition time, especially in 2D survey.

For further shorten the data acquisition time, sampling scheme 2 shown in Fig. 2.5(b) has also been proven to give good results. In sampling scheme 2, the same set of frequency bins are used for all selected observation points. This sampling scheme has two advantages. First, the number of observation point can be significantly reduced. Second, the hardware implementation will be easier, since the same frequency set is used for all data acquisition points.
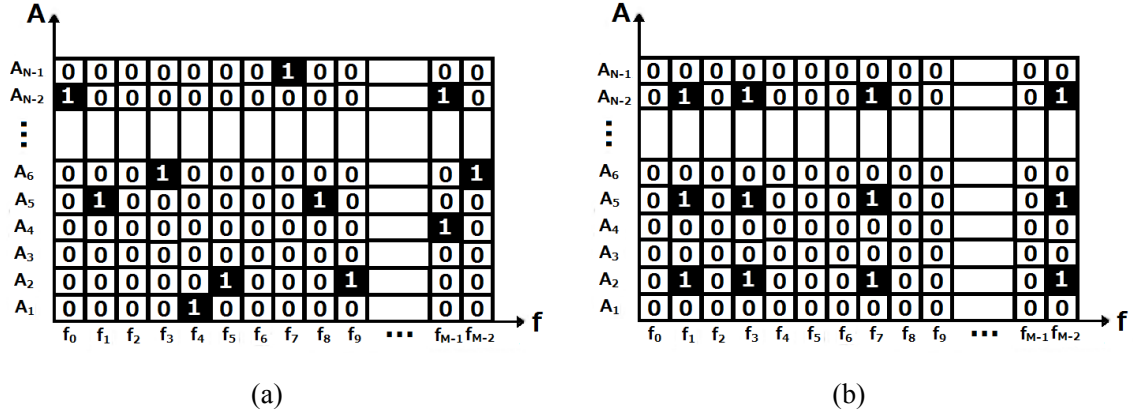
Fig. 2.5. Two examples of sampling matrix in CS applied to SAR. (a) Sampling schemes 1, (b) Sampling scheme 2 [16]

Mathematically, the sampling process is performed by multiplying the sampling matrix Φ to both side of Equation (2.10). The sampling matrix Φ is given by a two dimensional matrix, which has '1' value for the chosen sample and '0' otherwise. By defining y as the sampled measurement data, and $\mathbf{A}$ as the multiplication between Φ and Ψ, the CS problem for SAR imaging can be written below:

$$\Phi s_r = \Phi \Psi p$$
$$y = \mathbf{A}p \tag{2.19}$$

2.3.3. CS Algorithms

As explained in (2.3) CS finds solution by minimizing the ℓ_0 norm of the sparse problem. However, mathematically ℓ_0 norm is difficult to solve. There are two solutions to solve this problem. First, by simplifying the ℓ_0 norm into the minimization of ℓ_1 norm of the sparse problem, with ℓ_1 norm is the summation of each component in the sparse variable. ℓ_1 norm can be easily solved by linear programming. Equation (2.3) can be modified into ℓ_1 norm minimization as show below.

$$\hat{\alpha} = \arg\ \min \|\alpha\|_1 \ \text{subject to}\ y = \Phi\Psi\alpha \tag{2.20}$$

$$\|x\|_1 = \sum_i |x_i| \tag{2.21}$$

However, Equation (2.20) is only valid for the noiseless measurement. In SAR survey, the datasets always contains noise and clutter, therefore the noise parameter should be

19

included in the problem. Therefore, for the implementation in SAR imaging, the sparse solution can be derived by solving a modified convex optimization problem, called the Dantzig Selector as shown in (2.22). Another possible solution can also be derived by constraining the ℓ_2 norm of the measurement error, as shown in (2.23). ε_1 and ε_2 are the regularization parameters which is dependent on the noise level in the measurement.

$$\hat{\boldsymbol{p}} = \arg \min \|\boldsymbol{p}\|_1 \text{ subject to} \|\mathbf{A}^T(\boldsymbol{y} - \mathbf{A}\boldsymbol{p})\|_\infty \leq \varepsilon_1 \qquad (2.22)$$

$$\hat{\boldsymbol{p}} = \arg \min \|\boldsymbol{p}\|_1 \text{ subject to } \|\boldsymbol{y} - \mathbf{A}\boldsymbol{p}\|_2 \leq \varepsilon_2 \qquad (2.23)$$

with ℓ_2 norm is defined below :

$$\|\boldsymbol{x}\|_2 = \sqrt{\sum_i |x_i|^2} \qquad (2.24)$$

There are many algorithms has been developed to solve these ℓ_1 minimization problem, such as Basis Pursuit, Convex Programming, etc.

The second alternative to solve the CS problem is by using Greedy algorithm which works in iterations. In each iteration, the algorithms estimate one or some non-zero component/s and in the next iterations the algorithms estimate another non-zero components from the signal residual. Some of the Greedy algorithms that have been developed are OMP (orthogonal matching pursuit), CoSaMP (Compressed Sampling Matching Pursuit), Bayesian RVM (relevance vector machine) and many others. Compared to the linear programming, greedy algorithms can find the solution faster.

In this thesis, three greedy algorithms, i.e. OMP, CoSaMP, and Bayesian RVM, will be explained and discussed.

1)   Orthogonal Matching Pursuit (OMP)

Initialization		Signal Proxy		Augment Support
$r = y,\ t = 0$ $\text{supp} = \varnothing$	→	$t = t+1,\quad x_p = A^T r_{t-1}$ $\lambda_t = \arg\max(x_p)$	→	$\text{supp}_t = \text{supp}_{t-1} \cup \lambda_t$ $\mathbf{A}_t = \mathbf{A}_{t-1} \cup \mathbf{A}(:,\lambda_t)$

$t < S$

Break		New Residual		LS Estimation
$t = S$	←	$r = y - \mathbf{A}_t \hat{p}_t$	←	$\hat{p}_t = \mathbf{A}_t^{+} y$
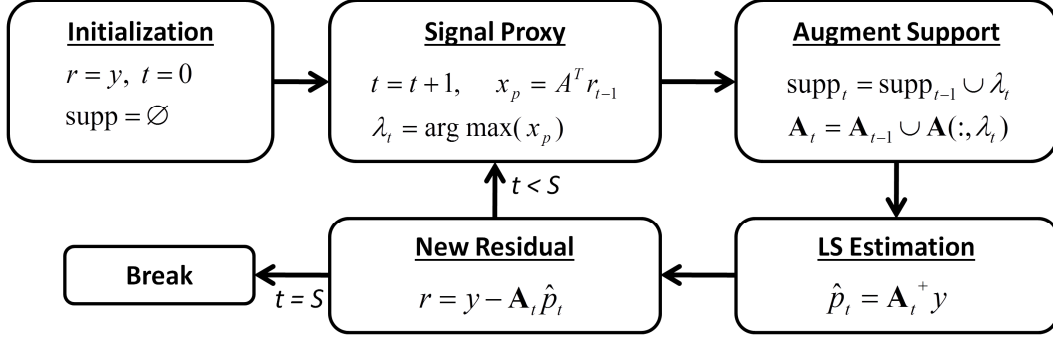
Fig. 2.6. OMP Algorithm

The algorithm of OMP is proposed by Mallat *et al* [37] and analyzed by Gilbert *et al* in [38]. The algorithm can be explained using the flowchart shown in Fig. 2.6. In each iteration, OMP estimates the index of the largest component of the non-zero component from the residual of the signal. The support of the largest component of the signal is estimated by the signal proxy $x_p = \mathbf{A}^T y = \mathbf{A}^T (\mathbf{A}p)$. Since in the CS problem the transformation matrix is an orthogonal matrix, $\mathbf{A}^T \mathbf{A}$ will be close to identity. Therefore from the signal proxy the rough estimation of energy distribution in the sparse signal can be derived. The largest coordinate of $x_p = \mathbf{A}^T \mathbf{A}p$ would correspond to the non-zero entry of p. Thus one support of the sparse signal is derived.

After a support is estimated, the sparse signal estimation is performed using Least Square (LS) by $\hat{p} = \mathbf{A}_t^{+} y$ with $\mathbf{A}_t$ is a matrix which only contains some columns (that is defined in the signal's support) of matrix $\mathbf{A}$, $\mathbf{A}_t^{+}$ is the pseudoinverse of $\mathbf{A}_t$ where $\mathbf{A}_t^{+} = \left(\mathbf{A}_t^{*}\mathbf{A}_t\right)^{-1}\mathbf{A}_t^{*}$. Then the residual of the signal is updated by subtracting the input signal with the last estimated signal. In the next iterations, the residual is used to find the next largest component of the signal, until *S*-sparse estimated signal is achieved. *S* which is the sparsity level of the signal is needed as a prior knowledge in this OMP algorithm. The sparsity level defines the number of non-zero component of the sparse signal to be reconstructed.

Fig. 2.7 shows an example of a time domain signal and its sparse representation in frequency domain. The sparse signal has three non-zero components, therefore the sparsity level $S = 3$. The non-zero components are located at 230Hz, 400Hz, and 540 Hz.

Therefore, the support of the signal is given below:

$$\text{support}(x) = \text{supp}(x) = \{i \mid x_i \neq 0\}$$

$$\text{supp} = [230, 400, 540]$$

(2.25)

(a)   (b)
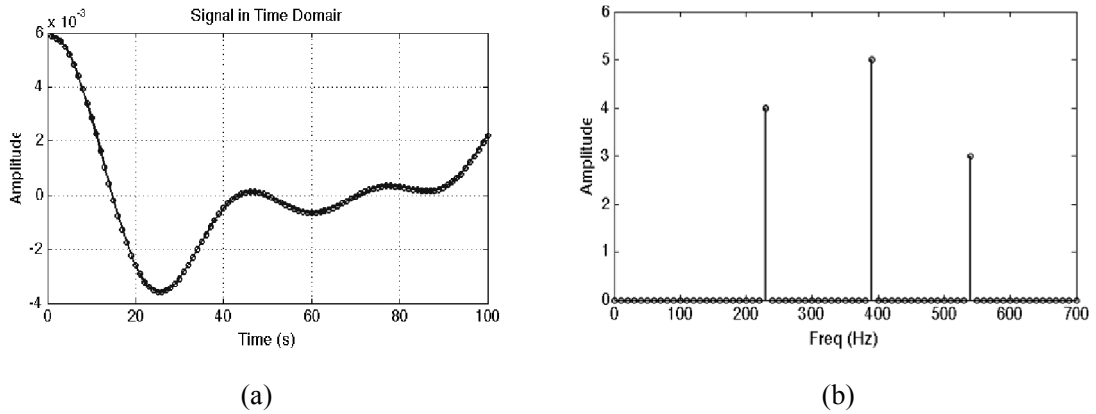
Fig. 2.7. Example of sparse signal with sparsity level 3. (a) Signal in the measurement domain, i.e. time domain signal (b) The sparse representation in frequency domain with sparsity level S = 3

Suppose a sampling process is performed to the time domain signal and the reconstruction process is performed by OMP. Since the sparsity level is three, then the iteration process is performed for three times. The results of each iteration are shown in Fig. 2.8.

22
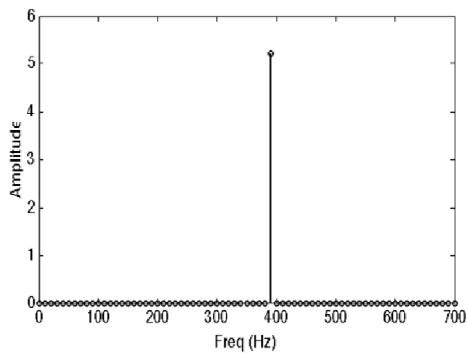
(a)
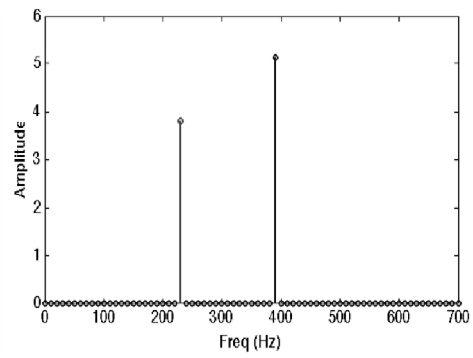
(b)
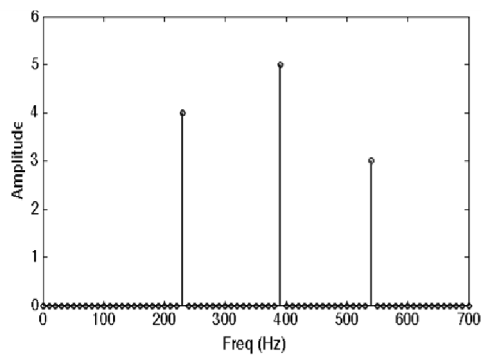
(c)

Fig. 2.8. The result of each OMP iterations. (a) First iteration, supp_1 = [400], (b) Second iteration, supp_2 = [400, 230], (c) Third iteration, supp_3 = [400, 230, 540]

2) Compressed Sensing Matching Pursuit (CoSaMP)
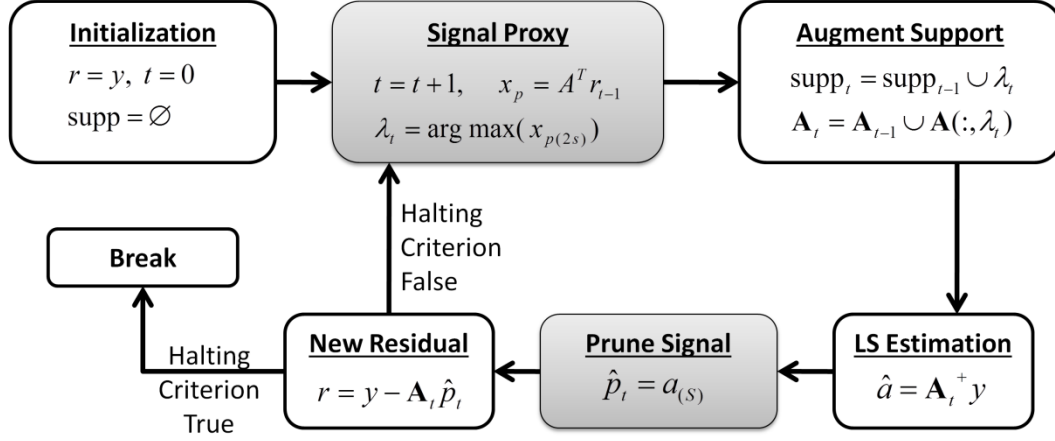
Fig. 2.9. CoSaMP Algorithm

CoSaMP algorithm is proposed by Needell *et al* [39]-[40], and can be explained by flowchart shown in Fig. 2.9. The processing algorithm is almost the same with OMP, the difference is shown by grey boxes in Fig. 2.9. In CoSaMP algorithm, in each iteration, several indexes (2*S*) of the largest components of the signal are estimated at once, using the same signal proxy as the OMP algorithm. The sparse signal estimation is also derived using LS estimation, by multiplying the pseudo inverse of the basis function with the input signal. The estimated signal is then pruned by selecting only the *S* largest components. This pruned signal is used to update the signal residual, which will be used in the next iteration to find the position of 2*S* largest components. The newly estimated supports will be combined with the support from the last iteration before performing LS estimation. This process continues until the halting criterion is satisfied.

3) Bayesian Fast Relevance Vector Machine (RVM)

Fast Bayesian RVM is a CS algorithm works based on Bayesian statistic approach, proposed by Tipping *et al* [41]-[43]. Fig. 2.10 explains the algorithm by using a flowchart. In each iteration, Fast RVM tries to maximize the marginal likelihood (ML) of the Bayesian problem. According to the value of s_m and q_m, one index can be added to the support, re-estimated, or deleted from the support. The change of ML due to this action is calculated, and the execution is performed on the support which gives the largest increase in ML. According to the action chosen (add/delete/re-estimate), the support and the values of some Bayesian parameters (α_{λ_t}, Σ, μ, s_m, q_m) are updated. The iteration

continues until the halting criterion is satisfied.
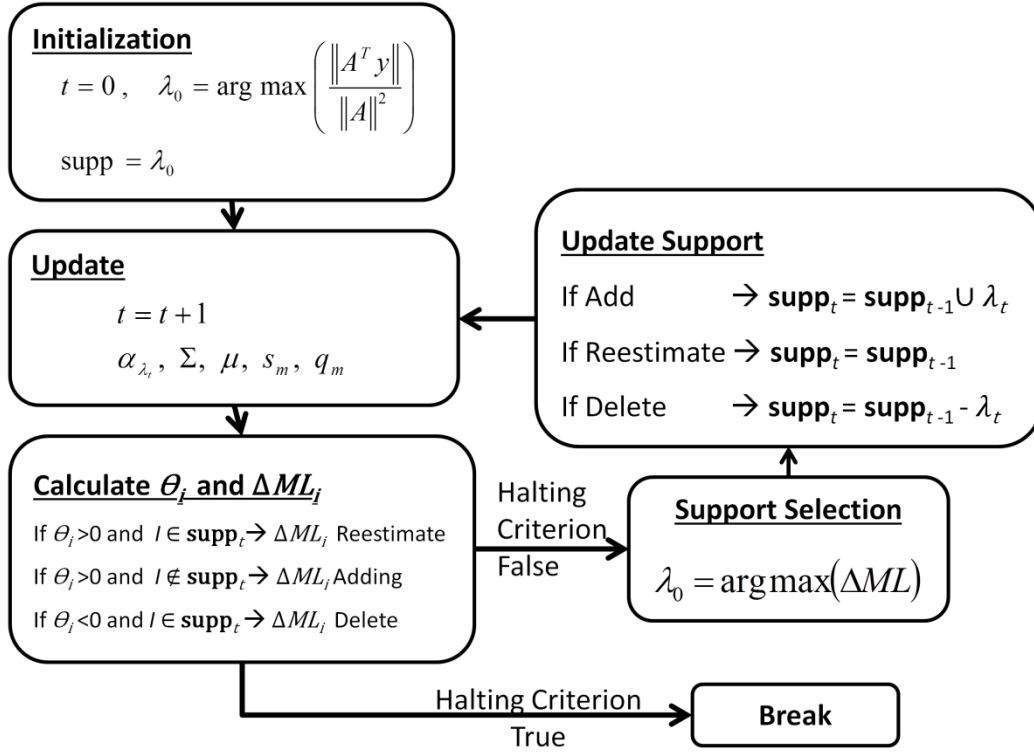
Fig. 2.10. Bayesian Fast RVM Algorithm

2.4. Example of CS Implementation for SAR Imaging

In this chapter, CS will be applied to GB-SAR experimental data received in [45]. GB-SAR system used in this experiment is developed in our lab, consists of Vector Network Analyzer (VNA) working in Stepped Frequency-Continuous Wave (SFCW) mode, a diagonal dual polarized broadband horn antenna, an antenna positioner unit, and a PC-based control unit. As target, a metal sphere of diameter 7.5 cm. SFCW signal uses frequency from 1 GHz to 6 GHz with 1601 frequency points. The data is acquired at 601 observation points with 1 cm scan step. The purpose of the experiment is to observe the azimuth dependency on the reflection, by locating the target in three different positions from the azimuth center of the system as shown in Fig. 2.11.
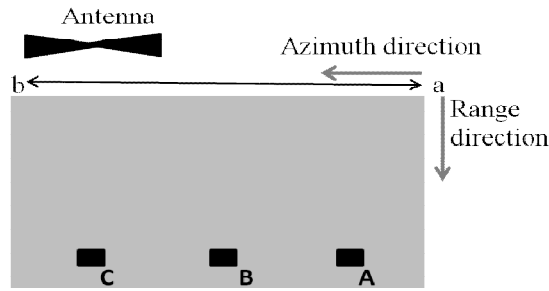
Fig. 2.11. GB-SAR experiment configuration with a purpose to observe azimuth dependency in SAR imaging [45]

CS is simulated by performing the sampling process to the experimental data. Two sampling methods proposed in [16] are used in this work. The first sampling scheme is a random selection of antenna positions and frequency bins separately, as illustrated in Fig. 2.5(a). For the second sampling scheme, like shown in Fig. 2.5(b), is a more organized sampling, conducted by using only 50 antenna positions and same 20 frequency bins for each position. Each set of data were processed by the convex programming by using CVX package developed by Grant and Boyd [36].

Fig. 2.12 (a)-(c) shows the imaging results by conventional SAR processing using all the measurement data. Fig. 2.12(d)-(f) shows the reconstructed image by CS with sampling scheme 1, using 1% sample of the measurement data. And Fig. 2.12(g)-(i) shows CS reconstruction result with sampling scheme 2, using 1% data. The above results show that even with about 1% data, CS can produce images that lead to the same conclusion as the conventional GB-SAR system. As an addition to its faster data acquisition, CS image contains less sidelobes around the target reflection and has less clutter than the image generated with 100% data. We can clearly notice that the reflection of target is not in the exact position if the target is not positioned in the center of azimuth axis (position A and C) and there is also degradation in the intensity of target reflection.

Comparing the resulted images, sampling scheme 1 and 2 gives the same image quality. But in implementation, sampling scheme 2 gives more advantage than sampling scheme 1. By using sampling scheme 2, we should only move antenna for 50 positions out of 101. In GB-SAR system, moving antenna along the track requires time because we need to wait for the antenna to be in a stable position before continuing to gather the data in the next position. And by using only 20 frequency bins out of 641, the scanning time for each position will be much reduced. Further, by choosing the same frequency bins for each

position, the hardware implementation will be easier. However, for sampling scheme 2, the sampling matrix should be more carefully designed, since the probability that sampling scheme 2 is incoherent with the sparse basis, is not as high as sampling scheme 1. For the real application of CS in experiment, the sampling matrix can be designed before doing measurement, by calculating the mutual coherence between the sampling matrix under test and the known sparse basis. The value of mutual coherence should be as low as possible.
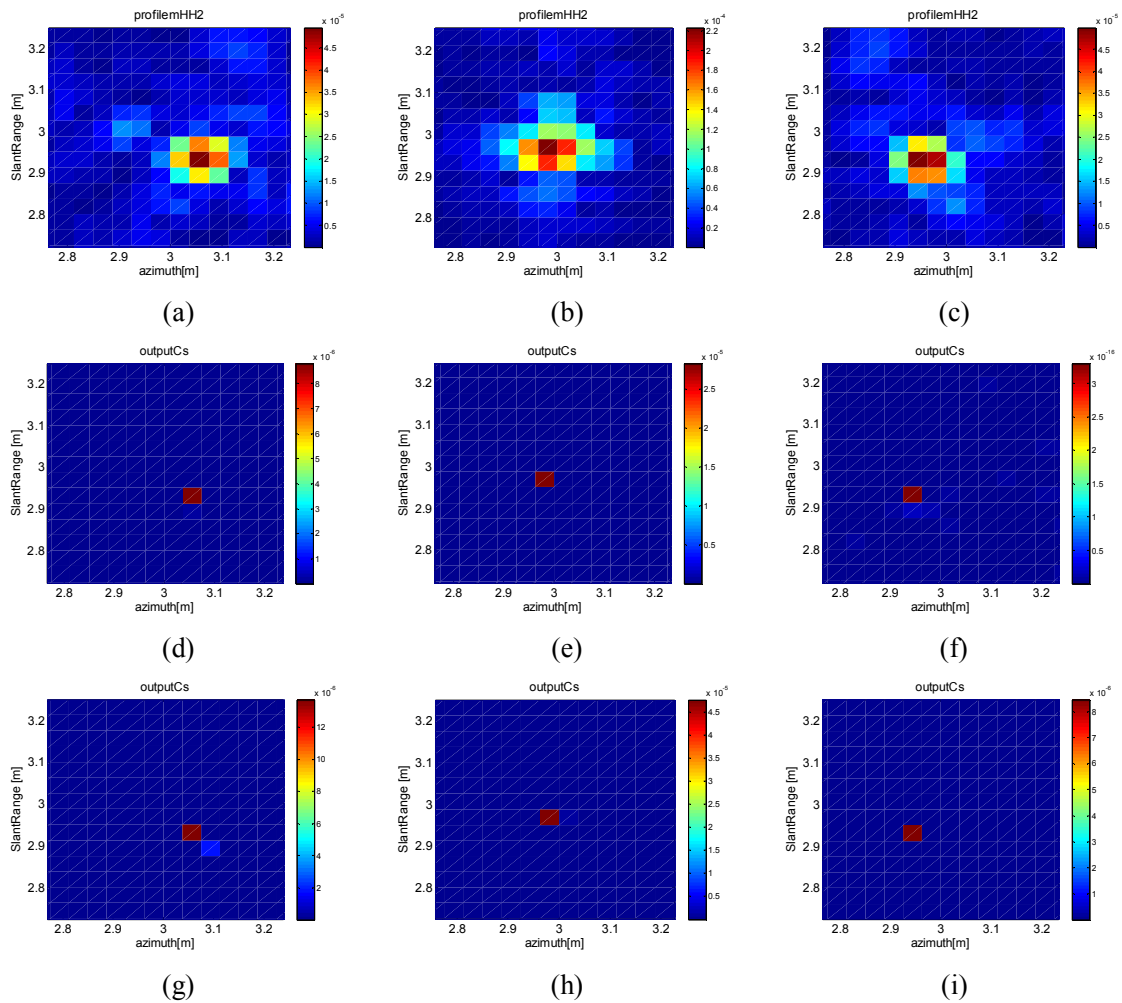
Fig. 2.12. GB-SAR reconstructed image of a sphere located at three different azimuth locations. (a) Reconstructed image by conventional Fourier based SAR, using full data in position A (b) B and (c) C, (d) Reconstructed image by using sampling scheme 1 in position A, (e) B, and (f) C, (g) Reconstructed image by using sampling scheme 2 in position A, (h) B, and (i) C.

In case of CPU processing time, generation of CS image needs much longer time for solving the convex programming. The amount of input data for CS is very low compared

to the conventional system but the process of solving l_1 minimization problem includes iteration process that requires more time. CS image is generated in about 200 seconds, about 20 times longer than image generation using full data showed by Fig. 2.12(a)-(c). However this extra processing time is quite acceptable with the compensation of decreasing of data collection time for moving antenna and scanning through frequency bins.

2.5. Summary

In this chapter the basic theory of CS including the requirement to implement CS, how CS finds solution and some CS algorithms has been presented. It is also explained how to implement CS to SAR imaging by reconstructing the representation matrix and choosing the sampling matrix. An example of implementation of CS to GB-SAR imaging has also been presented by using laboratory experimental data.

3. CS-Based Imaging for 2D Scan GB-SAR System

3.1. Introduction

Ground Based-Synthetic Aperture Radar (GB-SAR) system is a SAR system realized by an antenna moving on a fixed rail on the ground and acquiring data at discrete points along the observation line. GB-SAR system works by transmitting stepped frequency signal in each observation point, and recording the signal response for each frequency. The recorded data is then processed by signal processing to create GB-SAR image that shows electromagnetic properties of the object. Better quality image can be produced by having denser observation points and using wider bandwidth with denser frequency points. However, this will lead to long data collection time and huge amount of data to be processed.

GB-SAR system has also been used for 2D scan application, creating 3D GB-SAR image which gives more specific information about target location in the measured area. 2D scan requires more cost and time in acquiring data and also has higher contribution of measurement noise due to position error, antenna vibration, and other variables.

One solution for this data acquisition problem is Compressive Sensing (CS), which has the ability to reconstruct sparse information from an undersampled and noisy measurement. In this chapter, the study on the implementation of Compressive Sensing (CS) for continuous 2D scan GB-SAR measurement is presented.

3.2. Conventional 3D SAR Image Reconstruction

The 2D Scan GB-SAR system can be used to investigate the electromagnetic behavior of a target with precise location in a 3D plane. The position of target can be predicted by calculating the electromagnetic reflectivity of each pixel in the imaging area. The imaging process can be performed by 3D Fourier based SAR processing which is developed from 2D Fourier based SAR processing explained in Chapter.2.3.
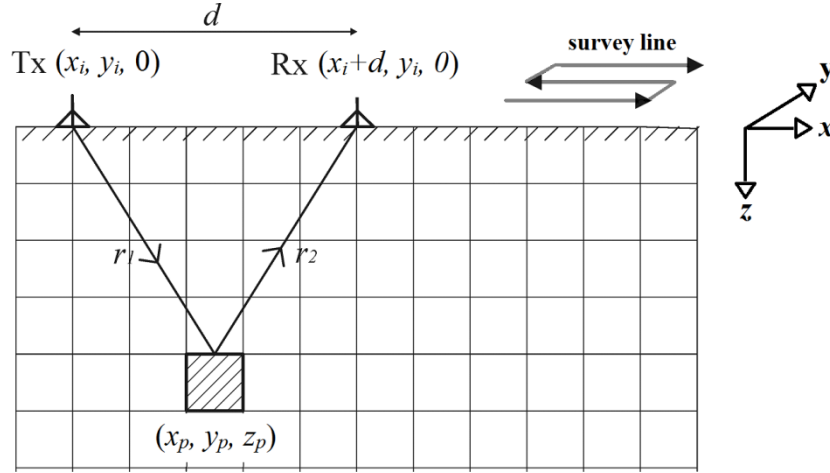
Fig. 3.1. The coordinate definition of antennas and the imaged pixel during 3D image reconstruction in SAR system

In 2D-scan GB-SAR system, the measurement is conducted in 2D plane, and the target is located in 3D imaging area. Consider the data acquisition is acquired in x-y plane by a pair of Tx-Rx antenna separated by d in x axis, as shown in Fig. 3.1. Signal received at one position of antenna track is specified by (3.1).

$$s_r(i,m) = \sigma \exp\left(- j2\pi f_m \tau_i\right) \tag{3.1}$$

for $0 \le m \le M - 1$, where $s_r(i,m)$ is the signal received at the the m-th frequency band and the antenna is located at (x_i, y_i). σ is the reflection coefficient of the target, and τ is the propagation delay between the target and the antenna, and M number of frequency bands used.

Propagation delay (τ) is defined by (3.2), with r is the two-way propagation distance between the transmitter antenna to the target located at (x_t, y_t, z_t) and from the target to the receiver antenna. c is the signal propagation velocity in the air ($c = 3 \times 10^8$ m/s) and d is the separation between transmitter and receiver antenna.

$$\tau_i = r_i / c$$

$$
\begin{aligned}
r_i &= r_1 + r_2 \\
&= \sqrt{(x_t - x_i)^2 + (y_t - y_i)^2 + (z_p)^2} + \sqrt{(x_t - x_i - d)^2 + (y_t - y_i)^2 + (z_p)^2}
\end{aligned}
\tag{3.2}
$$

The 3D image of GB-SAR measurement can be derived by dividing the observed area into some pixels with proper resolution. The value of each pixel can be calculated by processing the data received at all antenna positions and all frequency bands, using the Fourier Based Migration shown in (3.3).

$$p(x_p, y_p, z_p) = \frac{1}{NM} \sum_{i=0}^{N-1} \sum_{m=0}^{M-1} s_r(x_i, y_i, m) \exp(-j2\pi f_m r_{i,p} / c) \tag{3.3}$$

for $0 \le x_p \le N_x^p - 1$, $0 \le y_p \le N_y^p - 1$, $0 \le z_p \le N_z^p - 1$, with $p(x_p, y_p, z_p)$ is the estimation of electromagnetic reflectivity of the object located at pixel (x_p, y_p, z_p) in GB-SAR image, $s_r(x_i, y_i, m)$ is the signal received at the i-th observation point when the antenna is located at (x_i, y_i) and at the m-th frequency point, N is the number of observation points in x-y plane. M is the number of frequency points, and $r_{i,p}$ is the propagation distance between transmitter antenna at position $(x_i, y_i, 0)$ x_a, y_a) to the pixel at position (x_p, y_p, z_p) and from the pixel to the receiver antenna at position $(x_i + d, y_i, 0)$, with d is the separation distance between the transmitter and receiver antenna.

3.3.   Implementation of CS to 2D-Scan GB-SAR System

3.3.1.   Representation Matrix

CS problem can be formulated from the SAR processing at (3.3). In 2D-scan GB-SAR system, the data is sparse in spatial domain, represented with three-dimensional p matrix. The measurement is performed in space-frequency domain, given by three dimensional s_r matrix. To define the representation basis, s_r and p should be modified to be 1-column vectors by concatenating its column, as shown in (3.4) and (3.5).

$$s_r = [s_r(1,1); s_r(2,1); \ldots; s_r(N,1); s_r(1,2); s_r(2,2); \ldots; s_r(N,M)] \tag{3.4}$$

$$p = [p(1,1,1); p(2,1,1); \ldots; p(N_x^p,1,1); \ldots; p(N_x^p, N_y^p,1); \ldots; p(N_x^p, N_y^p, N_z^p)] \tag{3.5}$$

From the relation between s_r and p, the representation basis Ψ can be derived like shown in (3.7).

$$s_r = \Psi p \tag{3.6}$$

$$\psi_{k,l} = \exp(2\pi f_k r_{k,l} / c) \tag{3.7}$$

for $0 \le k \le K - 1$ and $0 \le l \le L - 1$, with $K = NM$ is the number of full measurement data in spatial-frequency domain, and $L = N_y^p N_x^p N_z^p L$ is the total number of pixel in the image.

Since s_r and p has been transformed into one column vectors, we need to define which frequency is used in the k-th column of s_r (f_k), the antenna position corresponding to the k-th column of s_r $\left(x_i^k, y_i^k, 0\right)$, and the pixel position corresponding to the l-th column of p $\left(x_p^l, y_p^l, z_p^l\right)$, as given below

$$f_k = f\left(\left\lceil \frac{k}{N} \right\rceil\right) \tag{3.8}$$

$$r_{(k,l)} = \sqrt{(x_p^l - x_i^k - d)^2 + (y_p^l - y_i^k)^2 + (z_p^l)^2} + \sqrt{(x_p^l - x_i^k)^2 + (y_p^l - y_i^k)^2 + (z_p^l)^2} \tag{3.9}$$

$$x_l^p = x^p\left(l - \left(N_x^p\left(\left\lceil \frac{l}{N_x^p} \right\rceil - 1\right)\right)\right) \tag{3.10}$$

$$y_l^p = y^p\left(\left\lceil \frac{l - \left(N_x^p N_y^p\left(\left\lceil l / N_x^p N_y^p \right\rceil - 1\right)\right)}{N_x^p} \right\rceil\right) \tag{3.11}$$

$$z_l^p = z^p\left(\left\lceil \frac{l}{N_x^p N_y^p} \right\rceil\right) \tag{3.12}$$

$$x_i^k = x_i\left(k - \left(N\left(\lceil k / N \rceil - 1\right)\right)\right) \tag{3.13}$$

$$y_i^k = y_i\left(k - \left(N\left(\lceil k / N \rceil - 1\right)\right)\right) \tag{3.14}$$

3.3.2. Sampling Scheme

To ensure the performance of CS measurement system, the sampling matrix should be chosen carefully in order to make it highly incoherent with the representation basis. Two sampling methods have been proposed, which is random sampling and semi-random sampling. The random sampling chooses random sample in space-frequency domain, while in semi-random sampling, the same set of frequency points is chosen for each randomly selected observation points. The semi-random sampling is easier to implement in hardware and also reduce antenna movement significantly. [16] shows that semi-random sampling works as well as random sampling. However, the semi-random sampling, if not carefully selected, may result in decreasing incoherency between sampling matrix and representation matrix.

In this work, another sampling procedure is implemented and shown in Fig. 3.2. Vertical axis represents the observation points and the horizontal axis represents the frequency points. This sampling scheme works on two steps :

1. Several observation points are randomly selected, as shown in rectangular red box in Fig.3.2.
2. For each observation point, a different set of random frequency points is selected, shows by the black marked box with '1' value in Fig. 3.2.

This scheme can minimize antenna movement, while maximizing the randomness of the sampling matrix.
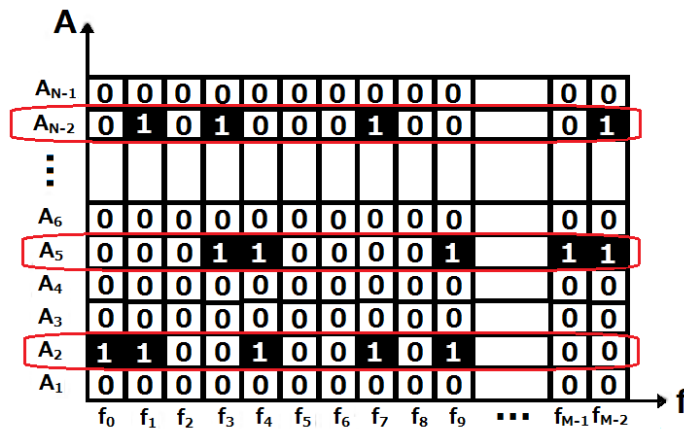
Fig. 3.2. Sampling scheme used to minimize spatial sampling during the measurement.

3.3.3. Noise Parameter (ϵ)

There are two factors that contribute to the noise parameter in CS implementation. First is the measurement noise, due to positioning error, and other disturbances, including clutter. Second is the contribution of the target itself if it is not exactly a sparse target. Sparse target means that there are only a very small number of its elements which has the largest magnitude, and the other elements should be zeros. If the other elements are not zeros, but are negligible, the target can still be regarded as sparse, but the contribution of the small non-zero elements to the noise parameter should be carefully estimated.

Consider p is a not truly sparse N-dimensional matrix. As shown in Fig. 3.3, p_s is the matrix contains the M largest elements of p and another elements are set to zero, and p_e is the matrix contains N-M residual elements with smaller and negligible values of p. The measurement sample y can be shown in equation (3.15), which shows two factors n_e and n_m contributing in CS noise parameter (ϵ).

$$
\begin{aligned}
y &= \mathbf{\Phi\Psi}p + n_m \\
y &= \mathbf{\Phi\Psi}(p_s + p_e) + n_m \\
y &= \mathbf{A}p_s + n_e + n_m
\end{aligned}
\tag{3.15}
$$
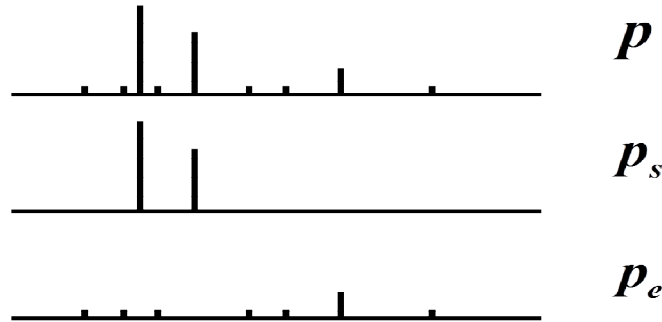
Fig. 3.3. Example of not-truly sparse vector

3.3.4. CS Solution

Each set of data were processed by the convex programming by using CVX package developed by Grant and Boyd [36], available online at http://cvxr.com/cvx/. This software works on convex programming for solving l_1 minimization.

3.4. 2D-Scan GB-SAR Experiment

3.4.1. Experiment Setup

An experiment is conducted using 2-dimensional *xy* positioner. The GB-SAR data is collected at 961 positions, with 31 *x* positions and 31 *y* positions, each separated at 2.5 cm. Two Vivaldi antennas separated at 20 cm is used. Anritsu VNA sweeps from 100 MHz to 4 GHz at 275 frequency points. As the target, a metal sphere with a 3 cm diameter, located about 80 cm above the antenna rail is used.

Fig. 3.4. Configuration of Experiment with xy positioner and Vivaldi antennas
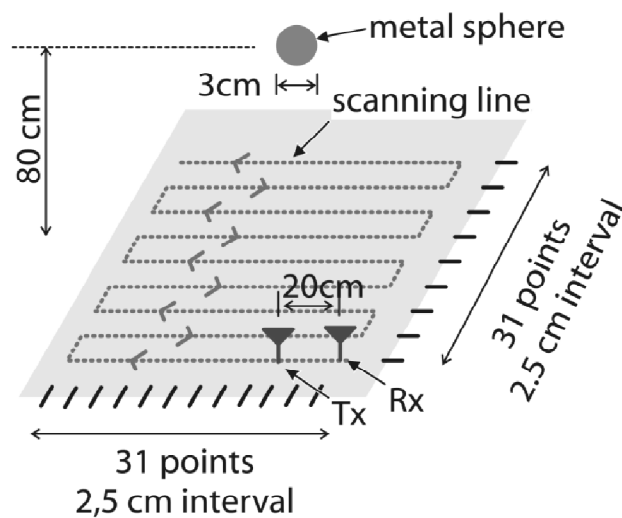
Fig. 3.5. 2D-Scan GB-SAR experiment setup with a metal sphere as a target.

According to the experiment parameter, the Nyquist criterion for spatial sampling for this experiment is calculated in (3.16). From the calculation, the separation between two observation points should be less than 3.75cm. Compared to this value, the experiment has satisfied the Nyquist criterion.

$$\Delta x = \frac{\lambda_{min}}{2} = \frac{c/f_{max}}{2} = \frac{3\times10^8/4\times10^9}{2} = 3.75\,\text{cm} \tag{3.16}$$

The data acquisition is performed using bidirectional and continuous scan, as shown in Fig. 3.6, which means the antennas are moving while the VNA is sweeping along frequency range. This could slightly shift scan position between low frequency component and high frequency component. And bidirectional movement may also give different scan behavior between two consecutive scan lines which have different scan direction. This condition will contribute to noise measurement.
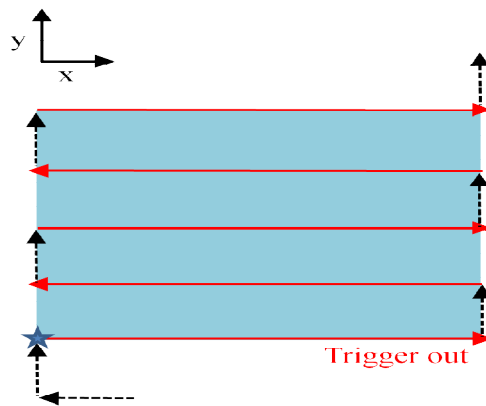
Fig. 3.6. The data acquisition procedures by bidirectional scan

3.4.2.   Pre-Processing of Experiment Data

The measurement data is pre-processed using flow chart shown in Fig. 3.7. The background subtraction is performed, and to remove the noisy part of the signal, the data is also filtered using Band Pass Hamming Filter with center frequency 2 GHz. After this processing, the data will be sampled offline to be used for CS implementation.
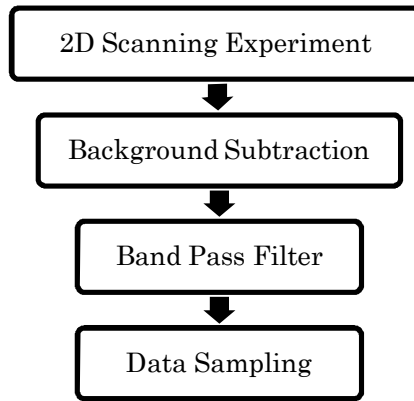
Fig. 3.7. Pre-processing of experimental data

| (a) | (b) |
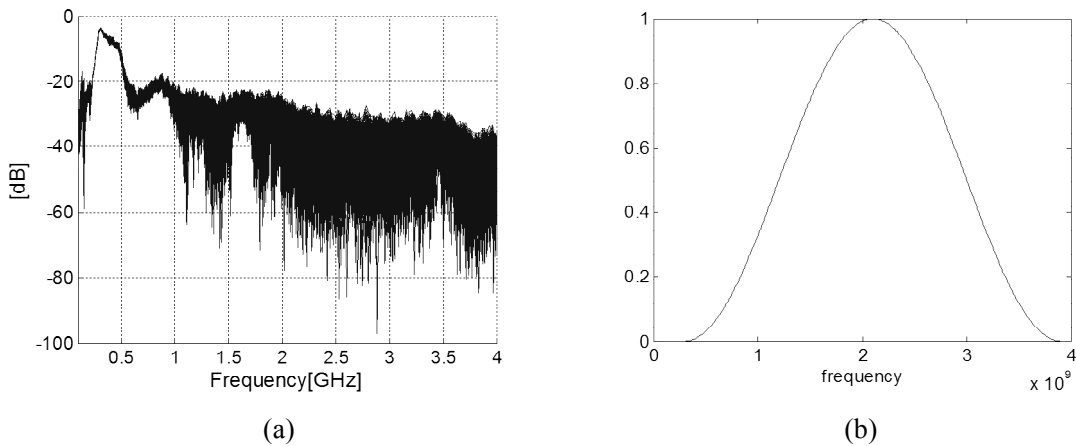
Fig. 3.8. (a) Frequency spectrum of the mesurement data. (b) Hamming window used for BPF

Fig. 3.8(a). shows frequency response of the measured data and Fig. 3.8(b). shows the Band Pass Filter applied in pre-processing. Fig. 3.9 shows the 2D time domain signal received in the center of 13-th position at y axis after each processing step. Time domain raw data is shown in Fig. 3.9(a), and the raw background data is shown in Fig. 3.9(b). The reflection of metal sphere is visible, after the raw data is subtracted with the background data, represented by a hyperbolic curve in Fig. 3.9(c). However, significant amount of noise and clutter can still be seen. Fig. 3.9(d) shows the data after applying Band Pass Filter which reduced the level of noise in the data.
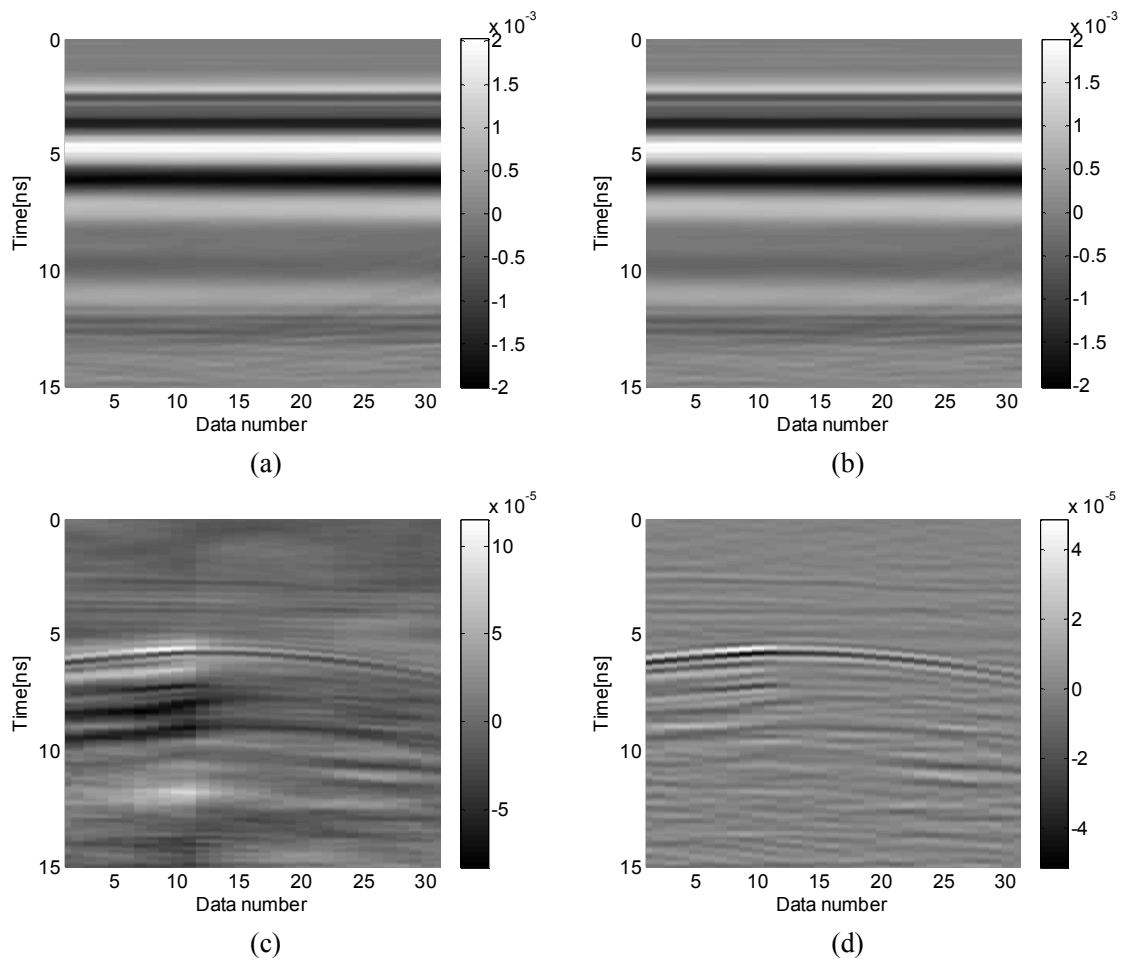
Fig. 3.9. 2D GPR Traces at y(13). (a). Data, (b). Background, (c). After Background Subtraction, (d). After BPF

To check the quality of the experiment data, other pre-processed 2D data at some other positions of y are given in Fig. 3.10, and some other position of x in Fig. 3.11. These figures show that the experiment data still contain residual clutter in some positions. Especially in Fig. 3.11, it is noticed that there are some staggering effect between two consecutive 2D scan lines which occurs because of positioning error and continuous sweep.
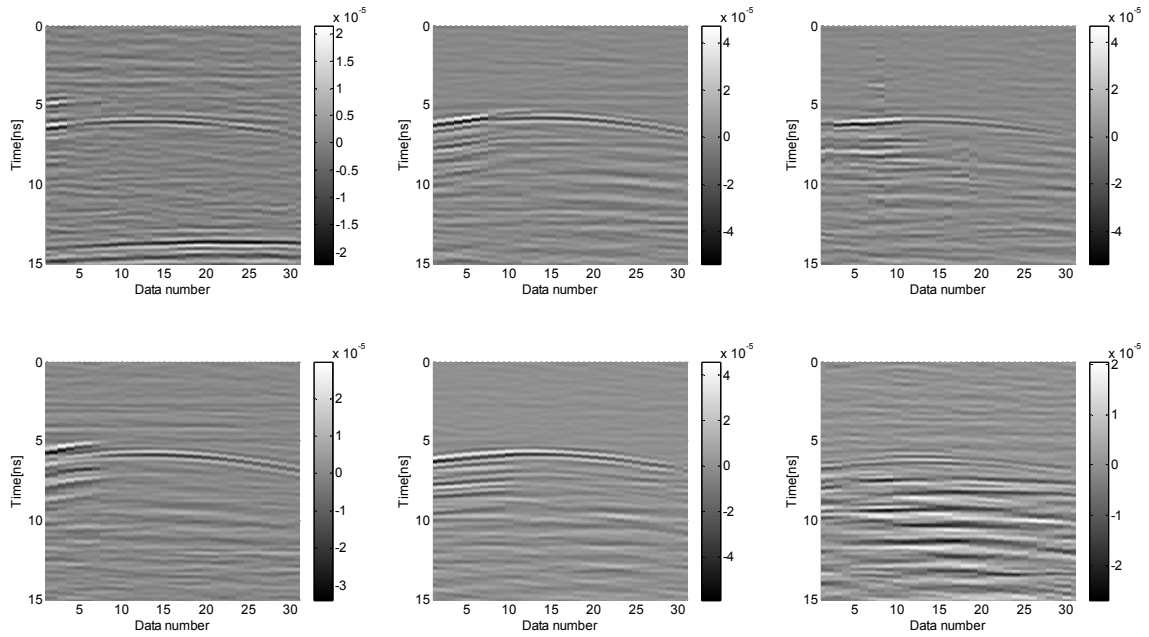
Fig. 3.10. 2D GB-SAR traces at (a). y(6), (b). y(10), (c). y(16), (d). y(19), (e). y(25), (f). y(30)
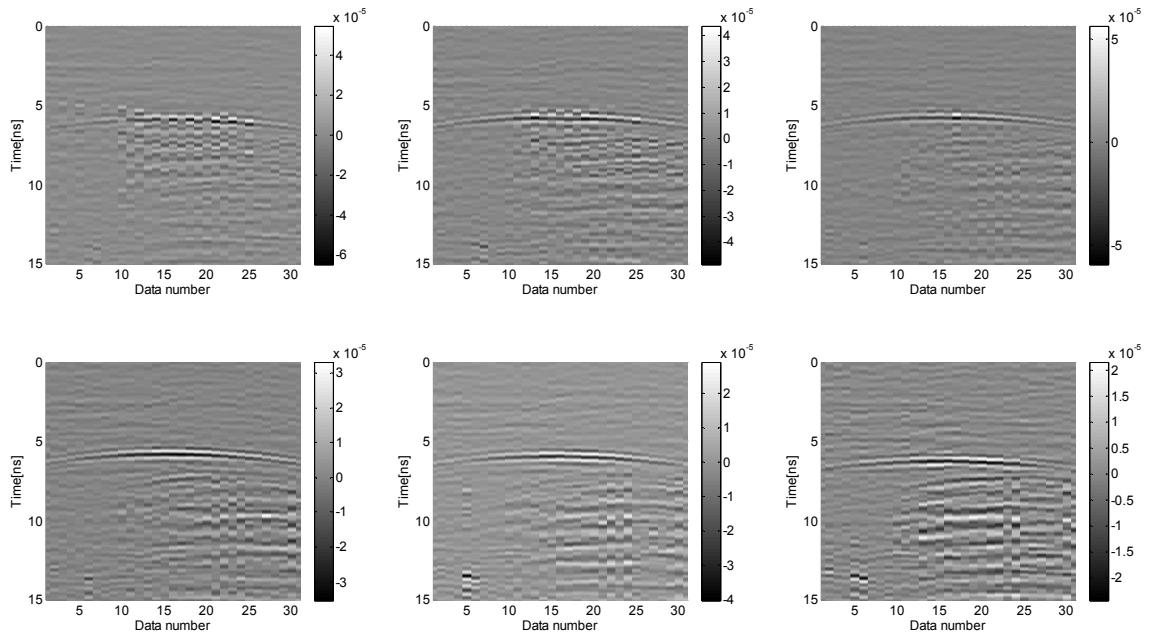
Fig. 3.11. 2D GB-SAR traces at (a). x(6), (b). x(10), (c). y(16), (d). y(19), (e). y(25), (f). y(30)

3.4.3.   Conventional SAR Processing

In conventional measurement techniques, all the received data is used in migration process to reconstruct GB-SAR image. The GB-SAR image contains some pixels in *xyz*

plane, where each pixel shows electromagnetic properties of the object located in that pixel position. In order to show the quality of the image reconstruction, it is important to show the value of each pixel in the image. However, it is difficult to show in the three dimensional figure. Therefore, to show the value of each pixel, the magnitude plot is used in this thesis as shown in Fig. 3.12(a). The magnitude of each pixel in each vertical slice of the three dimensional image in Fig. 3.12(b) is shown in one dimensional line in Fig. 3.12(a).

(a)   (b)
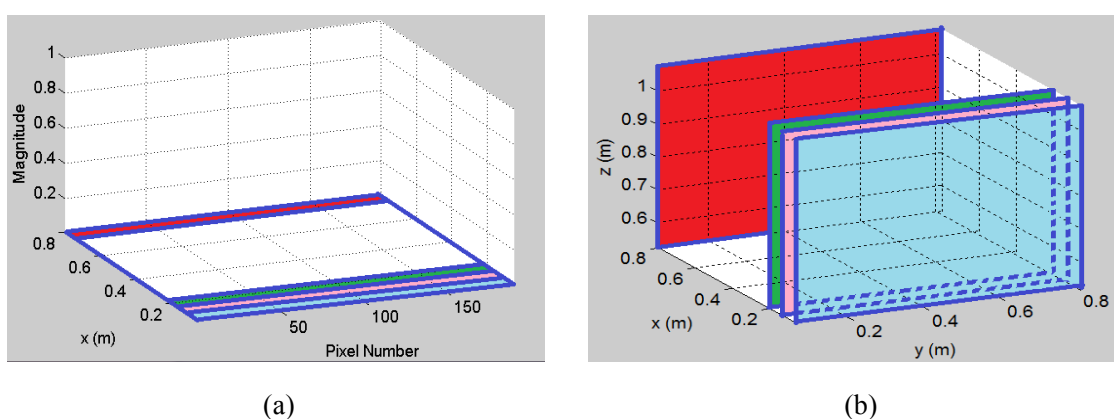
Fig. 3.12. Two images used to evaluate the image reconstruction results, (a). Magnitude plot to show the magnitude of each pixel in each vertical slice, (b) 3D GB-SAR image, shows only pixels which magnitude larger than the defined threshold

By using all measurement data for 3D Fourier Based Migration explained by Equation (3.3), the resulted GB-SAR image is shown in Fig. 3.13. In constructing GB-SAR image, it would be better to use small pixel size to get high resolution image. In this figure, the GB-SAR image is represented with pixel size is 1x1x1 cm.

To evaluate the sparseness of the experiment result, the magnitude of each pixel in 3D GB-SAR image is shown in Fig. 3.13. It is noticed that the target is represented by more than 1 peak value in GB-SAR image. This is because we choose small pixel size. In order for a point target to be represented by only one peak in GB-SAR image, the pixel size should be the same size or bigger than the target size, the target size should be smaller than the resolution of the measurement system, and the target should be exactly located inside one pixel. For CS processing, the pixel size of the image should get more consideration, as will be explained in the next section.

(a)

(b)

(c)

(d)

(e)
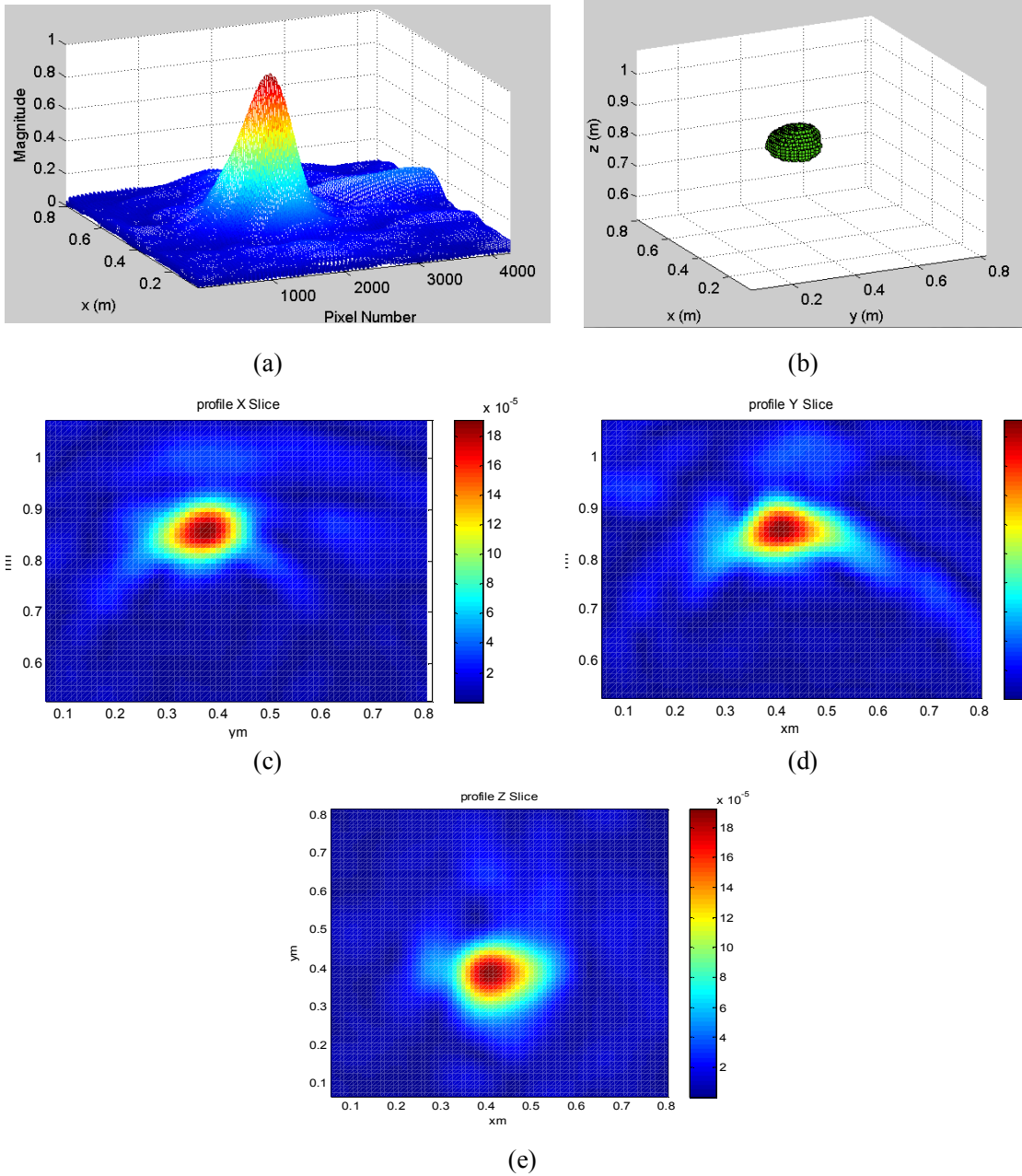
Fig. 3.13. The reconstructed GB-SAR image with 100% data by conventional SAR processing, using pixel size 1x1x1 cm. (a) Magnitude of each pixel of GB-SAR image. (b) 3D GB-SAR image with imaging threshold = 0.5. (c) X Slice. (d) Y slice. (e) Z Slice

3.4.4.   Parameter Selection and Assumption

Before implementing CS to the system, several parameters need to be chosen, which are the sampling matrix, noise parameter, and the pixel size in GB-SAR image. Sampling matrix described in Fig.3.2. is applied to the system. The CS theory has shown that the minimum number of sample needed to get exact reconstruction of the measured object is $C(\mu^2(\boldsymbol{\phi},\boldsymbol{\psi})\log N)Q$, where Q is the number of sparse target and $\mu(\boldsymbol{\phi},\boldsymbol{\psi})$ is the coherence between $\boldsymbol{\phi}$ and $\boldsymbol{\psi}$.

1. Number of Sample

Different number of samples in space and frequency are chosen to show how the number of sample influences the result of CS processing. In this report, three sets of spatial-frequency number of sample are applied; (48,14), (64,18) and (96,27). Because the spatial sample and frequency sample are randomly selected, it is considered that the resulted sampling matrix is incoherent with the representation matrix with high probability.

2. Noise Parameter for Convex Programming

Another parameter that needs to be selected prior to CS processing is the noise parameter (ϵ). The result of CS is very depended on the accuracy of this parameter. In this work, it is assumed that the noise parameter is accurately known, by calculating through inverse equation (3.17), with **A** is the sampling matrix ($\boldsymbol{\Phi}$) multiplied by representation matrix ($\boldsymbol{\Psi}$), and $\boldsymbol{p}_s$ is the expected sparse result as described in equation (3.15), with only 1 value located at the pixel with highest value in GB-SAR image shown in Fig.3.13. The other elements in matrix $\boldsymbol{p}_s$ are set to zero.

$$\varepsilon = \left\| \boldsymbol{y} - \mathbf{A}\boldsymbol{p}_s \right\|_2 \tag{3.17}$$

3. Pixel Size

The last parameter that should be chosen is the size of pixel in GB-SAR image to be generated. A pixel size too small will result in a big matrix of $\boldsymbol{p}_s$, and further require longer CS computation time. And if the pixel size is much smaller than the size of the target, the sparsity of the problem will be reduced. On the other hand, using large pixel size would reduce the resolution of the image. If we have a point target, ideally the the size of pixel is the same as the resolution of the measurement system, and the target is

exactly inside one grid of pixel. If the target is not exactly inside one pixel, the sparsity of the CS problem will be slightly reduced.

(a)

(b)

(c)

(d)

(e)
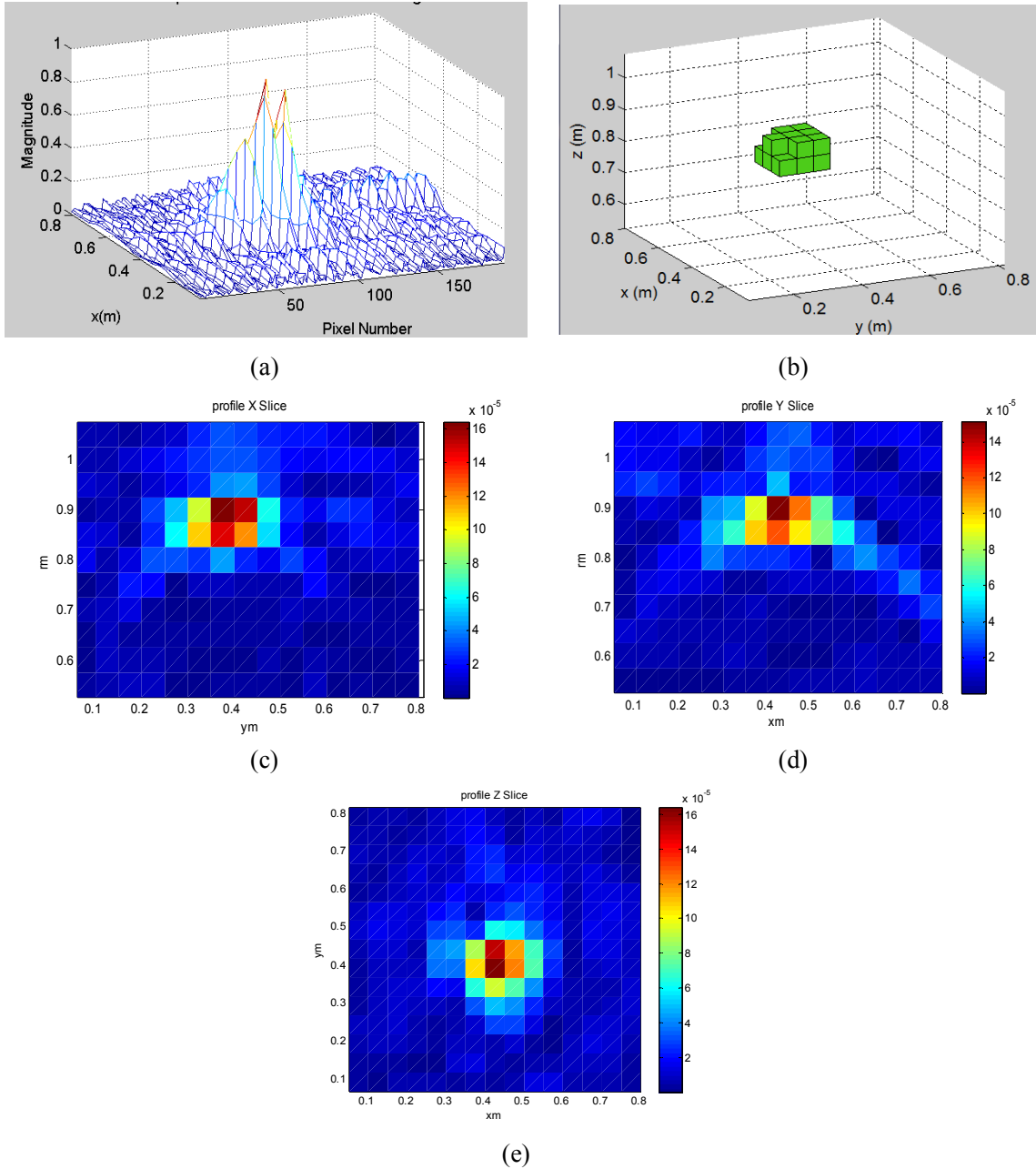
Fig. 3.14. The reconstructed GB-SAR image with 100% data by conventional SAR processing using pixel size 5x5x5 cm. (a) Magnitude of Each Pixel of GB-SAR Image. (b) 3D GB-SAR image with imaging threshold = 0.5. (c) X Slice. (d) Y slice. (e) Z Slice

In this work, the pixel size is set to 5x5x5 cm, the same as the range resolution of the measurement system. But, the spatial resolution of our system seems to be bigger than 5

cm, so that the 3 cm metal sphere is represented by more than 1 peak value in GB-SAR image. The GB-SAR image after resolution reduction and the magnitude of each pixel are presented in Fig. 3.14(a) and Fig. 3.14(b). To get impression about the magnitude distribution in 3D plane, in Fig. 3.14(c)-(d) the slices of GB-SAR image at the center position of the target are shown. It can be seen that after reducing the resolution, the full spatial-frequency measurement still doesn't give a truly sparse result in spatial domain. But the significant highest peak has been reduced to 6, compared with about 3000 another pixel with small values. Since we are only interested for the pixels with highest value in the spatial domain, the other pixels values are to be neglected and considered to contribute to the noise in the measurement.

3.4.5. CS Results : The Effect of Number of Sample

CS results are observed from several times simulation for each number of samples, i.e. (48,14), (64,18) and (96,27) spatial-frequency samples. It is observed that most of the time, all the three cases give the highest peak at the right position of the metal sphere. However, the case with smaller sample gives some noise at the other pixel positions, and the rate of fail detection is higher compared to the case using larger number of sample.

Eventhough CS gives result in more than one pixel, we can still get the impression that there is only one target in the scene, because the peaks are located in the neighbouring pixels. As an example, Fig. 3.15 shows 3D image and the slices of the CS results by using 1% sample of the measurement data. In this result, CS gives three peaks result that located closely together.

(a)   (b)

(c)   (d)

(e)
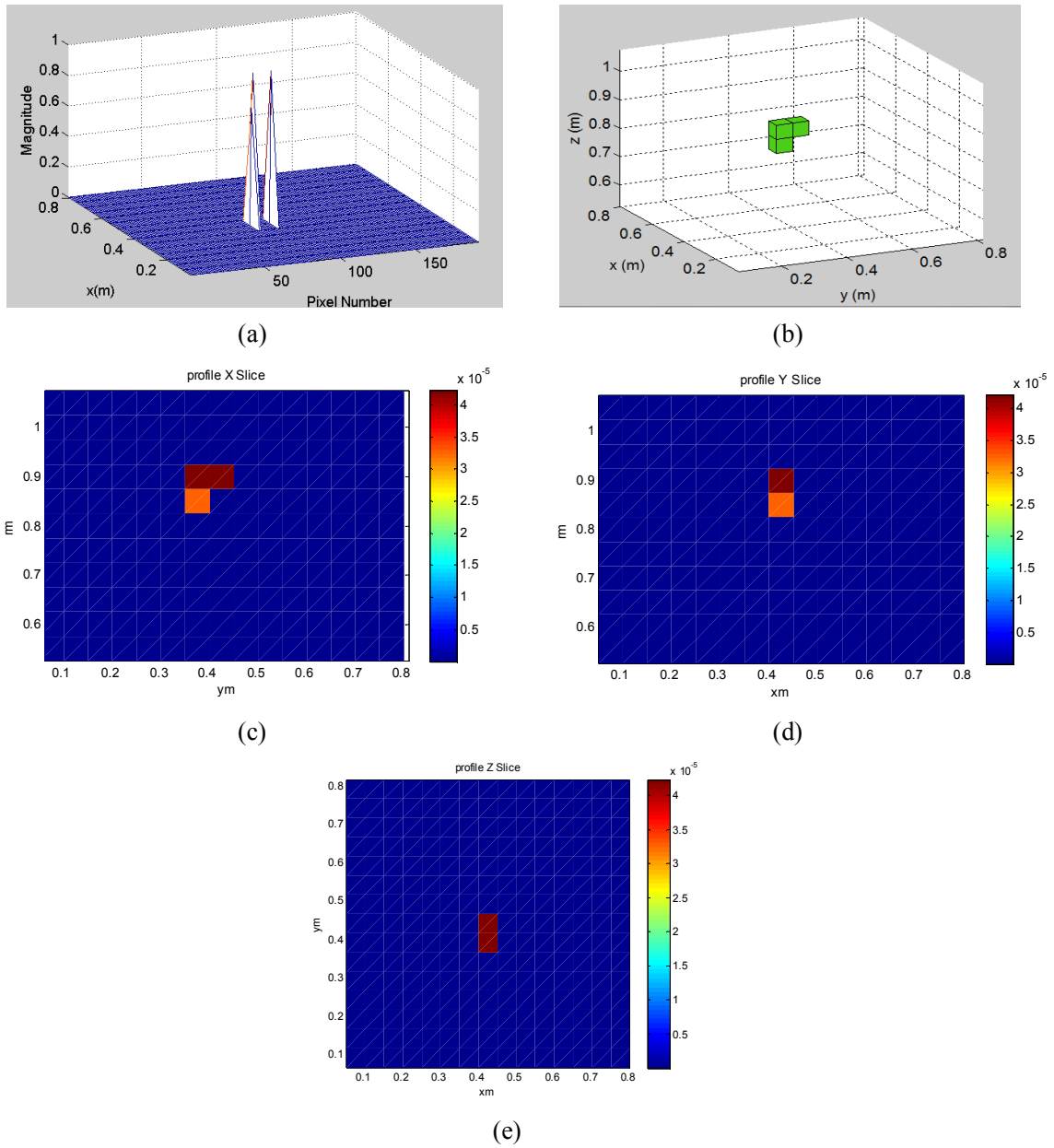
Fig. 3.15. The reconstructed GB-SAR image with 1% data by CS processing using pixel size 5x5x5 cm. (a) Magnitude of each pixel of GB-SAR image, (b) 3D GB-SAR image with imaging threshold = 0. (c) X Slice. (d) Y slice. (e) Z Slice

Fig. 3.16 shows an example for the case where CS fail to give correct reconstruction of the GB-SAR image. This result is derived by using 0.5% of the measurement data. In this result, there are two peaks detected at the location of the sphere, but another high peak is also detected at the wrong location. The X, Y, and Z slices cannot be shown because the target and the wrong peak are located in the different slices.

| (a) | (b) |
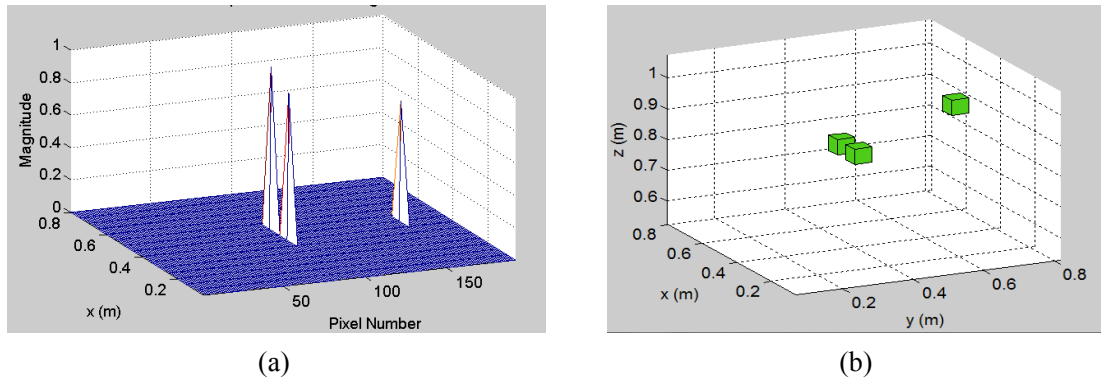
Fig. 3.16. Example of fail image reconstruction by CS using 0.5% data. (a) Magnitude of each pixel of GB-SAR image. (b) 3D GB-SAR image with imaging threshold = 0

3.4.6. Stability Measurement

To measure the stability of CS performance, the CS processing is repeated 100 times, each time with different sampling matrix, and accurate noise parameter. The results are summarized in Table.3.1. From the simulation results, it is observed that the CS result can be divided into 4 categories as given below:

1. Target Detection A means that the highest detected peak is located in the right position of the sphere. The location is considered right if the peak is located at one of the highest 6 peaks in the GB-SAR image derived by conventional SAR processing.

2. Target Detection B is the condition where the CS gives a peak at 1 or 2 pixels difference from the location of the 6 highest peaks.

3. Condition C means the target is detected at the wrong location or no target is detected.

4. And condition D means the CS gives peak at the right location, but also gives high peak at another wrong location.

In this work, the condition A and B are regarded as the acceptable results.

Table. 3.1. Performance of CS in 100 Processes

(Spatial Sample, Frequency Sample)	Target Detection			
	A	**B**	**C**	**D**
(48,14) = 0.5% Data	62	15	8	15
(64,18) = 0.75% Data	85	11	1	3
(96,27) = 1% Data	94	6	-	-

From Table.3.1, it is noticed that eventhough the sampling matrix is generated randomly, most of the time CS gives good performance. Using more samples can help stabilize the performance of CS. As can be seen at 1% sample case, the success rate is almost 100%. And it is also noticed that using enough measurement samples, the reconstructed noise and clutter in the resulted CS-GB-SAR image is also reduced, compared to the conventional processing.

3.4.7. The Effect of Noise Parameter

In this section, the effect of noise parameter will be shown. Fig. 3.17(a) shows CS result with accurate noise parameter ($\epsilon = 0.12$), while Fig. 3.17(b) shows CS result with slightly error in noise parameter ($\epsilon = 0.15$). It is noticed that using inaccurate noise parameter, CS was not able to give sparse result and only output noise distributed at all the pixels. This shows that the accuracy of noise parameter is one important factor that determines the quality of CS results.

(a)	(b)
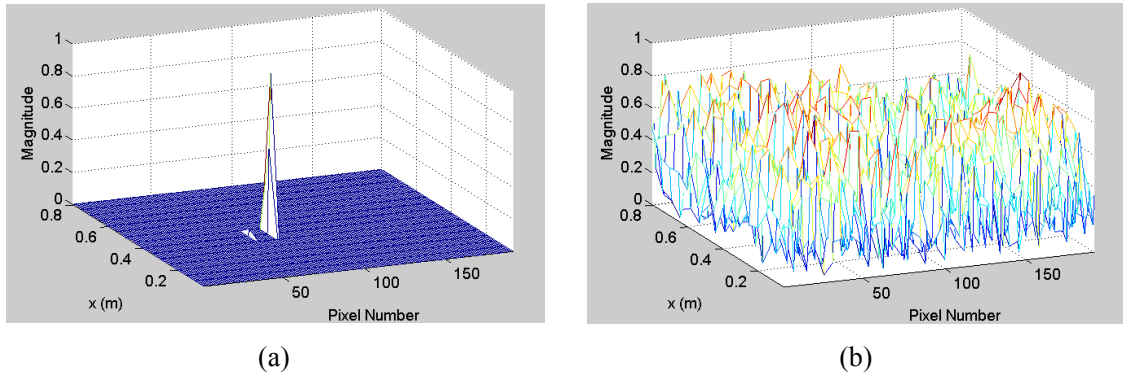
Fig. 3.17. Two reconstructed images showing the importance of accurate noise parameter in CS processing by convex programming. (a) Reconstructed image using accurate noise parameter, ($\epsilon = 0.12$). (b) Reconstructed image using inaccurate noise parameter ($\epsilon = 0.15$)

3.4.8. Processing Time

All the CS processing is performed on a 2.66 GHz Intel computer with 96 GB RAM. The processing time for each case of sampling number is shown in the Table3.2. For comparisons, the conventional migration process needs about 5.2561 minutes to generate the reconstructed GB-SAR image.

Table. 3.2. Processing Time

(Spatial Sample, Frequency Sample)	Processing Time (Minutes)
(48,14) = 0.5% Data	18.36
(64,18) = 0.75% Data	31.92
(96,27) = 1% Data	131.84

It is observed from Table.3.2 that compared to the processing time of conventional SAR processing, CS processing time by using convex programming requires a long computation time. Furthermore, the computation time increases significantly when the number of sample increases.

3.5. Summary

In this chapter, the CS implementation for 2D-scan GB-SAR system has been presented. The CS reconstruction by using convex programming is evaluated by using experimental data. The result shows that CS can reconstruct GB-SAR image even by using only 1% of the measurement data. The GB-SAR image generated by CS processing has a better quality than the image generated by conventional SAR processing. First, the sidelobe around the target reflection is eliminated in CS images. Second, the clutter in other imaging area is also reduced.

However, the CS reconstruction using convex programming is very dependent on the noise parameter, which is usually unknown in the real measurement. Small error in the noise parameter may cause the target reflection cannot be detected. Therefore, for the CS based image reconstruction for application such as GPR where the noise and clutter is usually high, the use of convex programming may be difficult. Another problem of using convex programming is that it requires a long computation time, which makes it unreliable for real time applications. Considering these problems, an alternative of CS algorithm by using greedy algorithm will be discussed in the chapter 4.

4. Detection and Localization of Subsurface Targets Using CS Processing by GPR

4.1. Introduction

The implementation of CS for SAR imaging using GB-SAR system has shown to have a good performance, hence it has a promising future in real implementation. However, for subsurface target imaging, the implementation of CS is more challenging, because it is expected to combat the high level of noise and clutter, signal attenuation and ground reflection in GPR signal.

This chapter discussed the way to improve CS performance in GPR system by selecting the most suitable data acquisition method and CS algorithm. Data acquisition method should be designed to enable GPR signal pre-processing to remove most of the unwanted reflection from the GPR signal. In this thesis, the focus in selecting data acquisition method is in reducing the number of observation points during the measurement. It is considered that reducing the number of observation points is more advantageous in GPR system then reducing the frequency points during the measurement, especially for future implementation in 2D GPR survey.

Beside data acquisition method, this chapter also discusses the CS algorithm which is able to give best solution in high clutter condition. Previous chapter has shown that convex programming gives good CS result when the noise parameter is known. However in GPR application it is difficult to estimate the noise parameter accurately. Another concern is that most of GPR application requires that the imaging result can be immediately seen in the measurement spot, such as for landmine detection case. In this case, the fast processing is preferred. Therefore, convex programming which has long processing time may not be suitable for these applications. In this chapter, the GPR imaging by greedy algorithm which has faster computation time with guaranteed performance is discussed. In this thesis, the selection of CS algorithm is limited for the purpose of the detection of specific subsurface target with known size.

4.2. Conventional Image Reconstruction by GPR

Image reconstruction by GPR can be regarded as a near range SAR system. The antenna moves along a survey line and illuminates the subsurface target from many different positions and angles. Therefore, a point target will be represented in a hyperbolic diffraction curve in a GPR profile. The SAR processing is performed to focus each hyperbolic curve to their original points to show the true shape and position of the reflectors in the imaging area. The SAR processing for GPR is the same as explained in Chapter.2.3, with the only difference is the wave velocity of propagation.
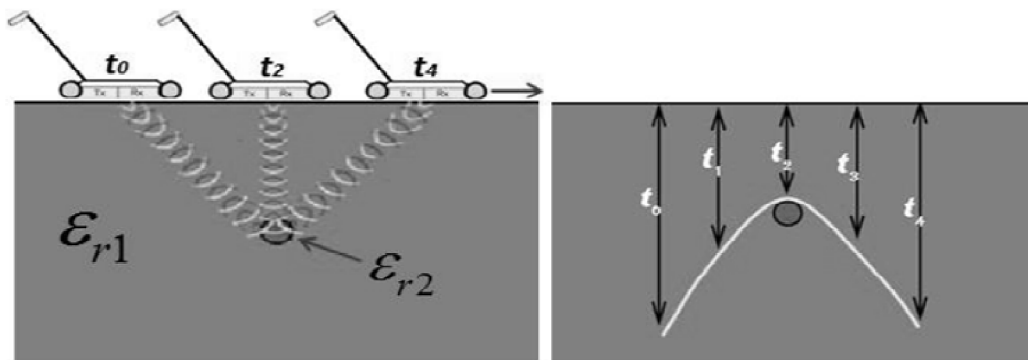
Fig. 4.1. GPR hyperbolic diffraction from a point scatterer (Gaber, 2012)

However, compared to GB-SAR system, GPR imaging has some problems is creating a high quality subsurface image. Like GB-SAR system, GPR works by transmitting an electromagnetic wave and analyze the reflected wave. The reflection of the electromagnetic wave occurs because of the change of dielectric properties along the signal propagation path, which is expected to come from the existence of subsurface object. However, in GPR system, there are many unexpected reflection contains in the returned signal, for example; the reflection from the ground surface, inhomogeneity of the soil, the change of moisture in the soil, etc.

4.3. Implementation of CS to GPR Imaging

4.3.1. Problems in implementing CS to GPR Imaging

At least, there are four factors that make CS implementation for GPR imaging becomes difficult:

1. High level clutter

   As explained before, the inhomogeneity of the soil may cause the GPR signal to contain high level of clutter, as well as the change of soil moisture in some part of imaging area. And in most condition, soil usually contains small objects like stones or tree roots which can also reflect the electromagnetic wave.

2. The ground reflection

   For CS imaging, the ground reflection must be removed before processing. If the signal still includes ground reflection, then the SAR image will contains many high value pixels at the air-ground border, which cause the signal cannot be classified as a sparse signal anymore. Furthermore, in GPR the reflection from the target is much weaker than the reflection from the ground surface, and it will be difficult to reconstruct by CS algorithm.

3. Signal Attenuation

   Wave propagating in soil is severely attenuated during the propagation. Without compensating the attenuation, the target in the deeper region will have much weaker reflection, and CS algorithm may regard it as noise.

4. The estimation of wave velocity

   In real application, it is difficult to measure accurately the wave velocity in the subsurface medium. The inaccurate velocity used in SAR processing will result in the SAR image does not focused perfectly. In CS system, this will reduce the sparsity of the signal which will affect the CS solution.

The importance of pre-processing in CS implemented to GPR system is demonstrated by using an experiment of a pipe detection, as shown in Fig. 4.2. Two bowtie antennas with separation 30cm are used to acquire data along 3m scanning line, with separation between each data points is about 1cm. The SFCW signal uses frequency from 10MHz to 1.5GHz, with 137 frequency points.

Fig. 4.2. GPR experiment configuration for a buried pipe detection. The scanning line is shown with an arrow line
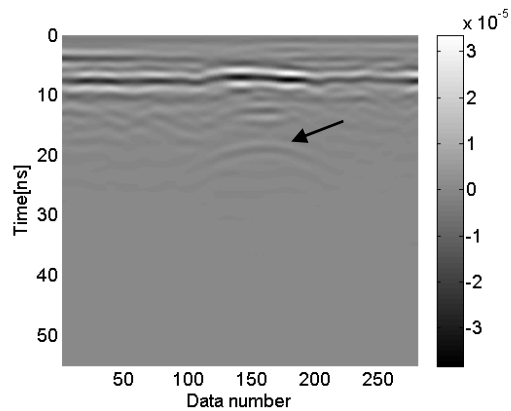
(a)
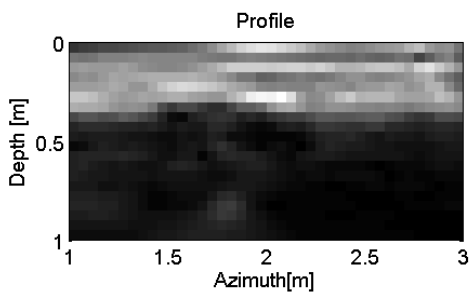
(b)
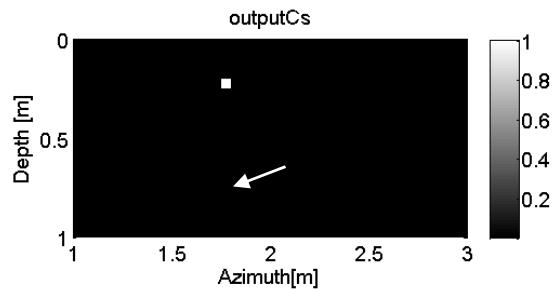
(c)

Fig. 4.3. Processing results without removing the ground surface reflection. (a) GPR time domain traces. (b) The reconstructed GPR image by conventional SAR processing using 100% data. (c) The reconstructed GPR image by CS processing using 2% of data

Fig. 4.3(a) shows GPR traces without any pre-processing step. In this figure, it is shown that the reflection from the ground surface is very strong. The reflection from the pipe is very weak compared to the reflection from the ground surface. The location of the pipe is shown by a black arrow in the figure. Fig. 4.3(b) shows the reconstructed GPR image by using all the measurement data. Most of the high value pixels are located in the shallow depth, and the pipe cannot be seen clearly. Fig. 4.3(c) shows the CS result by using 2% random measurement data. In this simulation, convex programming is used and the noise parameter that gives the sparsest solution is used. It is shown that CS reconstructs one single peak, but the location of this pixel does not show the correct position of the pipe. The location of the pipe in the GPR image is shown by a white arrow in the figure.

(a)   (b)

(c)   (d)
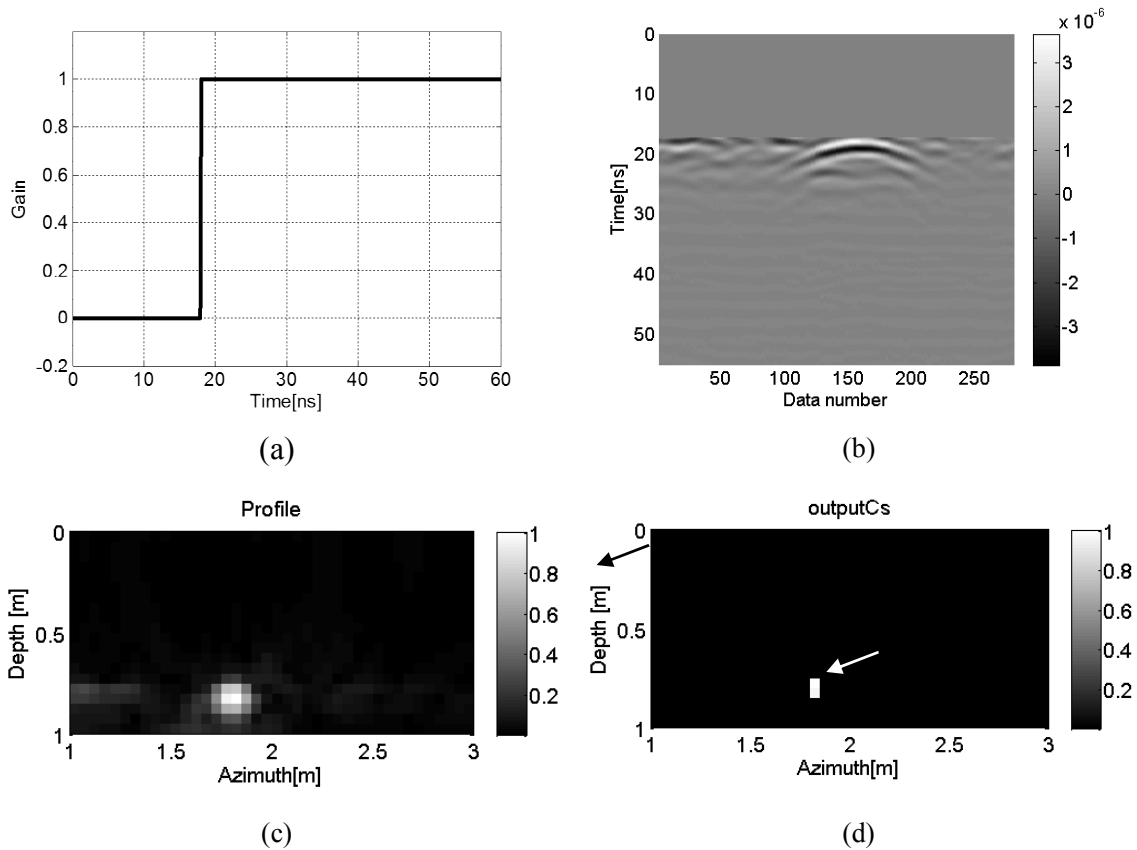
Fig. 4.4. Processing results after removing ground surface reflection by time gating. (a) Time windowing function. (b) GPR time domain traces. (c) The reconstructed GPR image by conventional SAR processing using 100% data. (d) The reconstructed GPR image by CS processing using 2% of data

Fig. 4.4 shows the result after performing ground reflection removal from the GPR data.

In this example, the ground reflection is removed by using time gating in time domain. The windowing function is shown in Fig. 4.4(a), which shows that signal before 18 ns will be multiplied by zero. Fig. 4.4(b) shows the GPR time domain traces after performing time gating. Compared to Fig. 4.3(c), in this figure, the ground reflection has been removed and the reflection from the pipe can be clearly seen. Fig. 4.4(c) shows the reconstructed GPR image by conventional SAR processing using all the measurement data. Fig. 4.4(d) shows the result of CS reconstruction by using 2% of data. In this image, the reconstructed pixels are reconstructed at the correct location of the pipe. Compared to the conventional imaging result, CS result has better resolution and lower level of clutter in the image.

From the two results shown in Fig. 4.3 and Fig. 4.4, it is concluded that pre-processing step is important in CS based image reconstruction. The existence of unwanted reflection such as the ground surface reflection may cause CS to give inaccurate result. Gurbuz *et al* [31] gives another solution to overcome the problem of ground surface reflection by excluding the near surface region from the imaging area. However, this method will limit the implementation of CS for imaging of shallow subsurface object. Tuncer *et al* [34] proposed a ground reflection removal method by using sampled frequency data. However, in this thesis, the purpose is to reduce the spatial data and reducing the frequency data is not a main concern.

4.3.2. Proposed Data Acquisition Method

The choice of data acquisition method presents an interesting topic within a discussion about CS. Previous studies ([32],[35]) showed a random data acquisition technique by reducing the number of frequency steps in each scan position, which enabled much faster scanning times. Other papers ([16],[31]) showed an alternative technique that exploited the spatial sparsity of the data by sampling not only in the frequency domain but also in the spatial domain. Unfortunately, even though the previous CS-GPR studies [31]-[35] has presented real experimental results, they are mostly focused only on reducing the frequency sample, and have not shown the effect of reducing spatial sampling to the performance of the CS-GPR experiment. Reducing frequency sampling would increase scanning speed, which is important in a number of applications where the target is in motion, such as ISAR. In this case, the observable interval of a target is usually very limited, thus high speed data acquisition is required. Another motivation is

fast scanning guarantees that during each scanning period, the target can be considered not moving, hence minimizing the motion effects in the signal processing.

In this work, a condition where reducing spatial sampling is more important than reducing the frequency sampling is considered, especially for GPR survey in a very large area such as landmine clearing operations. High scanning speed is not considered a priority in this case, because the subsurface target is stationary. This study will focus on the more interesting feature that CS can offer, which is the ability to reconstruct high reconstruction image using random and sparse spatial sampling. In the conventional measurement system, a dense and uniformly spaced spatial sampling is strictly required in order to satisfy the Nyquist criterion. If this condition is difficult to achieve during data acquisition, the interpolation is performed during the signal processing to estimate the data that is located exactly in the regular grid. On the other hand, CS based measurement can directly use the random and sparse spatial data and still acquire better image quality. This property of CS will be useful in saving acquisition time and work during the measurement. Furthermore, reducing the spatial data will also provide significant advantage in GPR surveys where the dense spatial observations are not possible due to difficult terrain in the observed area.

Several studies have investigated data acquisition schemes for radar applications. Suksmono *et al* [32] showed a prototype of a SFCW GPR system using a frequency synthesizer to automatically choose a different set of frequency points for each observation location. The sampled frequency information is used to reconstruct the time domain signal in each spatial position. This sampling method does not perform sampling in spatial domain, hence it will not be discussed further in this study.

Gurbuz *et al* [31] proposed another data acquisition scheme which consists of spatial sampling, followed by random frequency sampling in each selected spatial sample, as shown in Fig. 4.5(a). Huang *et al* [16] proposed a data acquisition schemes that is more conducive to hardware implementation by selecting the same set of frequency samples for each spatial position, as shown in Fig. 4.5(b). The results show that these proposed data acquisition methods work as well as the random sampling method. However, there is no guarantee that this sampling scheme will work for any randomly chosen spatial and frequency samples. If the samples are not carefully selected, the result may be decreased incoherency between the sampling matrix and the representation matrix.

Our concern with these approaches is that radar data, especially that from GPR, suffers a lot of noise and attenuation that needs to be pre-processed before imaging to obtain good quality of images. Some of these steps require processing in the time domain, but the time domain signal cannot be generated without full frequency data. Not many studies have tried to solve this problem.

Tuncer *et al* [35] has proposed a method to mitigate the GPR signal attenuation in the medium of propagation, but this method requires the knowledge about the attenuation model in the medium, which is usually difficult to estimate. In some cases, it is also necessary to select only a specific portion of the signal in the time domain, corresponding to the depth of interest and to remove the noise or clutter from other depth areas.

In the experiment on GPR explained in section IV, for example, the deeper target is almost invisible due to signal attenuation. This problem can be solved using automatic gain control (AGC) in the time domain, but if the frequency information has been sampled in the data acquisition process, this step is not possible to perform.

Based on these considerations, a different sampling scheme is proposed, where only spatial sampling is performed during the data acquisition. In each spatial sample, full frequency information is measured. Beside the less significant benefit from performing frequency sampling, the full frequency information is more beneficial to improve the quality of the GPR data. By having the full frequency information, the attenuation problem can be mitigated correctly while the noise and clutter suppressed. After pre-processing the frequency data is sampled to reduce complexity in CS processing.

We propose a CS-based data acquisition which is explained in these following steps:
1. Perform spatial sampling in the data acquisition process.
   Several spatial observation points are randomly selected, and all the frequency information at each point is measured. The small number of frequency points can be chosen to fix the acquisition rate; in our experiment we use 137 points. The sweeping time for all 137 frequency points is less than one second, so measuring all frequency points will not affect data acquisition time much.
2. Perform necessary pre-processing in frequency domain, e.g. band pass filter, ground reflection removal, etc.
3. Calculate the time domain signal at each spatial sample by using IFFT.

4. Use the time domain signal to perform necessary signal processing in time domain, e.g. AGC, time gating, etc.

5. Use FFT to calculate the frequency domain signal from the pre-processed time domain signal.

6. Perform random frequency sampling for each spatial sampled. This process is performed to ensure the incoherency between representation matrix and the sampling matrix, while at the same time reducing the amount of processed data.
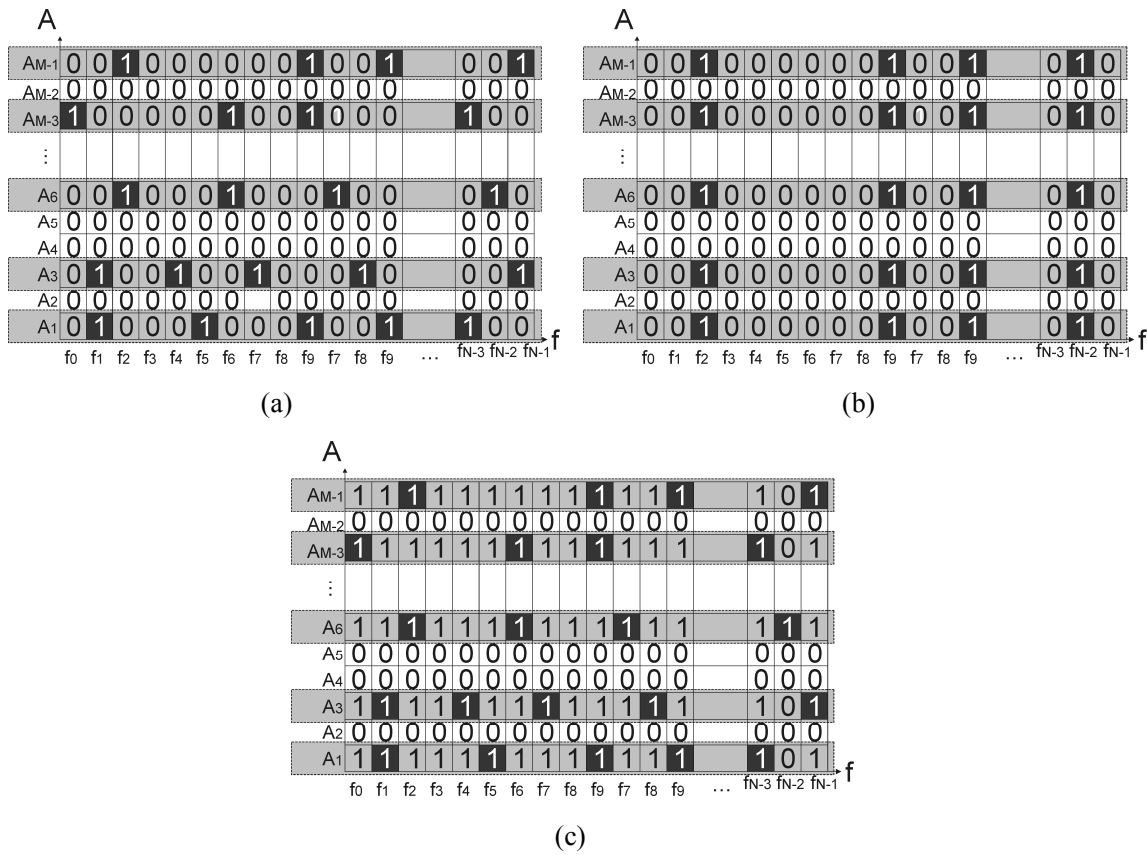
Fig. 4.5. Data acquisition methods for spatially sampled measurement. The selected spatial samples A are shown in the gray cells. At each of these spatial samples, frequency samples f are acquired, shown with '1's. And the frequency samples used in CS processing are marked black. (a) Random frequency selection. (b) Uniform frequency selection. (c) Proposed data acquisition techniques

Fig. 4.5(a) and Fig. 4.5(b) respectively illustrate the data acquisition schemes proposed by Gurbuz et al and Huang et al as explained above. A represents the observation points and f the frequency points. The gray cells showed the selected spatial positions for data acquisition. The '1's in the gray boxes showed the frequency data measured during the

data acquisition for that spatial position. The '1' in the black boxes shows frequency data used in CS processing. From Fig. 4.5(a) and (b), we can see that all the acquired frequency data is used in CS processing.

Fig. 4.5(c) illustrates the proposed sampling matrix. Unlike the two previous sampling schemes, in this method, all the frequency information is acquired during data acquisition (all frequency points have the value '1' in the gray boxes). But only some randomly selected frequency information (marked by '1' in the black boxes) is used in CS processing.

4.3.3. Proposed CS Algorithm

Under conditions of high clutter and non-sparse targets, noise will be a significant contribution to the sampled data; further affecting the solution of CS. For this reason, our application requires a CS algorithm that is not highly dependent on the knowledge of the noise level in the measurement, which offers fast computation time and provides a decision that is robust to noise.

In this paper, we compare the performance of some CS algorithms for application on our GPR data. The first two, orthogonal matching pursuit (OMP) and Bayesian fast RVM, are based on the greedy algorithm. The third is the compressive sampling matching pursuit mentioned above. The OMP and CoSaMP algorithms do not need any knowledge on noise level in the data, but they do require knowledge about the sparsity level S of the signal. The Bayesian RVM requires a rough estimation on the noise level, but it is not highly dependent on it. A rough noise estimation based on the variance of the sampled measurement is sufficient.

Our study proposes a modified Bayesian RVM, based on the Bayesian fast RVM described in [41]-[44], using the source code developed by Ji *et al* [44] and available online at http://www.ece.duke.edu/~shji/BCS.html. Fast Bayesian RVM works based on a Bayesian statistics approach. In each iteration, fast RVM tries to maximize the marginal likelihood (ML) of the Bayesian problem. This algorithm divides the indices of the sparse matrix into two groups, those included in the model and those outside the model. Initialized from an 'empty' model, this algorithm sequentially estimates a support and adds the index and its corresponding basis functions to the model. An index inside the model can also be re-estimated or deleted if in the process it is found to be redundant.

The change of ML is calculated for all the indices of the sparse signal. For the group inside the model, the change of ML is calculated for the action of re-estimation or deletion. For the outside model group, it is calculated for the adding task. The change of ML due to these actions is compared, and the execution is performed on the index which gives the largest increase in ML. According to the action chosen (add/delete/re-estimate), the support and the values of the Bayesian parameters are updated. The iteration continues until the halting criterion is satisfied.

The halting criterion in the original algorithm is observed from the changes of ML in the last two iterations. If the change is small enough, the solution derived is considered stable and the algorithm is terminated. However for a GPR application in which the target is not truly sparse and the signal has a high level of noise and clutter, using this halting criterion may result in some later estimated supports only reconstructing the unwanted noise. To improve the quality of the image, we modified this algorithm by adopting the principal of CoSaMP by stopping the process of adding a new support to the model after the algorithm has reconstruct $2S$ supports. Before terminating the algorithm, the $2S$ coefficients are pruned to an S- sparse matrix. This modification gives us faster computation time with better visualization of the real position of the target in the image.

Since in GPR case, $\mathbf{y}$, $\mathbf{A}$ and $\mathbf{p}$ matrices are all complex, they should be transformed beforehand to real value vectors as proposed in [16]. Then the solution can be derived using the modified sparse Bayesian algorithm as explained in the following steps:

1. Initialize noise variance σ^2 to some reasonable value (e.g. $\text{variance}(\mathbf{y}) \times 0.1$)

2. Initialize with a single basis vector A_i, i.e the i-th column of $\mathbf{A}$. Compute α_i and set all other α_m to infinity. The condition $\alpha_i < \infty$ shows that the basis vector A_i is in the model otherwise the A_i is excluded from the model. The set $\boldsymbol{\alpha} = (\alpha_1, \ldots, \alpha_L)$ consists of L independent hyperparameters, each one of which individually controls the strength of the sparsity prior over its associated weight [14].

3. Compute all Bayesian parameters. One of the important parameters, θ_i, is used to decide whether the basis vector A_i should be included in the model or excluded from the model.

4. For all i : if $\theta_i > 0$ and $\alpha_i < \infty$, compute ΔML_i for re-estimating α_i where ΔML_i is the change of ML.

5. For all i : if $\theta_i \leq 0$ and $\alpha_i < \infty$, compute ΔML_i for deleting A_i from the model and setting $\alpha_i = \infty$.

6. For all i : if $\theta_i \leq 0$, $\alpha_i < \infty$, and $N_s < 2S$, compute ΔML_i for adding A_i to the model and updating α_i. N_s is the number of the support that has been included in the model.

7. For all i : if $\theta_i \leq 0$, $\alpha_i < \infty$, and $N_s \geq 2S$, prune the S supports with lowest weight, then terminate.

8. Execute the selected action (re-estimate, add or delete) for i with the highest ΔML_i and update the value of α_i.

9. Update all Bayesian parameters, including the weight for each support i in the model.

10. If algorithm has converged, terminate it, otherwise go to 4.

Note that because of this modification, we now need an estimation of the sparsity level S of the signal. In the case of a compressible target, the sparsity level cannot be simply regarded as the same as the number of targets in the scene, because one target can be represented by more than one pixel in the CS result. The value of S should be chosen to be large enough to cover all the targets in the scene and small enough to discard noisy components in the image. For this reason, the proposed algorithm is more suitable for the detection of a specific subsurface object, which quantity and size is know, for example for finding the accurate location of a subsurface pipe.

4.4. CS-Based GPR Implementation for Pipes Detection

In this section, a real application of SFCW GPR is presented, in which GPR is used to detect two buried pipes in sand.

4.4.1. Experiment Setup

The experiment was conducted to detect two pipes buried under dry sand. The experiment setup and the position of the two pipes are shown in Fig. 4.6. The first pipe with a diameter of 2.2 cm was located at depth 20 cm. The second pipe, diameter 5 cm, was

located 75 cm under the sand, giving a very weak reflection to the GPR system due to signal attenuation in the sand. Two wideband bow tie antennas separated by 30 cm were used for data acquisition.
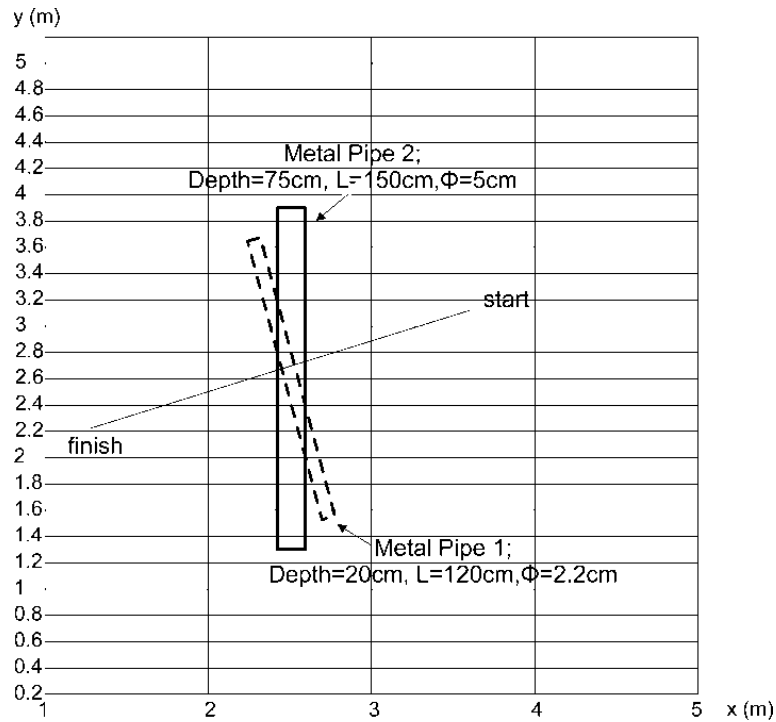
Fig. 4.6. GPR experiment configuration, with two pipes located at different depth as targets.

A vector network analyzer (VNA by Anritsu) was used to generate the step frequency signal and record the reflecting signal. The SFCW signal uses a frequency range from 50 MHz to 1500 MHz, with 137 frequency points and a 10.66 MHz frequency step. With a bandwidth 1450 MHz, the range resolution of the system is about 4 cm. The data was collected at 201 spatial observation points along a 1-D straight line on a flat ground surface. Each consecutive observation point was separated by 1.03 cm. The purpose of this study is to reduce the number observation points to hasten the data acquisition while maintaining the ability to detect any sparse or compressible object in the scene with high probability.

4.4.2. Signal Pre-Processing

As explained in section 2B, we perform signal pre-processing in frequency domain and followed by pre-processing in time domain. The pre-processing in frequency domain includes band pass filter, and mean subtraction for ground reflection removal. The

pre-processing in time domain includes automatic gain control (AGC) and time gating to select only the earlier part of the signal.

To simulate the CS-based data acquisition, the experiment data was sampled in the spatial domain before the pre-processing was performed. In this simulation, we used 70 spatial positions out of 201 positions, or about 35% of the full spatial data. After pre-processing, the frequency data was down-sampled by choosing a different set of 40 frequency points, or about 29% of the full frequency data, for each spatial point. In the real CS measurement, spatial sampling can be directly performed during the experiment's data acquisition, and the frequency sampling is performed during signal processing. Using this configuration, a total of 10.17% of the data was used in CS processing.

For a fair comparison, we will compare the amount of data used in CS processing with the amount of data required by the Nyquist sampling theorem. The Nyquist criterion for this measurement is calculated as follows. For the spatial step, the sampling theorem in Equation (1.3) gives that the distance (d) between two spatial sampling points should be smaller than 4 cm. Given the observation line from 0m to 2.06m, the sampling should be conducted at about 53 observation points.

For the frequency step, the sampling theorem is given in (1.4). In our measurement, the required unambiguous time duration (T) is about 20 ns from the beginning of the GPR traces, corresponding to the estimated depth of the sand pit. From (1.3), it is derived that the frequency step should be smaller than 25 MHz. Using a bandwith from 50 to 1500 Mhz and applying a 25 MHz frequency step, the number of frequency points needed according to the Nyquist theorem is 59 equally spaced frequency points.

4.4.3.   Imaging Result by Conventional SAR Processing

In this section, as a reference for the CS result, we show the GPR image resulted from the conventional Fourier Based SAR processing. In this conventional way, all the spatial-frequency measurement data is used and pre-processed as explained in the previous section. The resulted GPR image is shown in Fig. 4.7(a). The image used a high pixel resolution of 1mm x 1mm.   In this image two targets are clearly seen at different depths. The reflection of the ground surface has been completely removed and the reflection of the second pipe has been enhanced. However, a significant level of clutter and noise still remains especially in the deeper region around the second pipe.
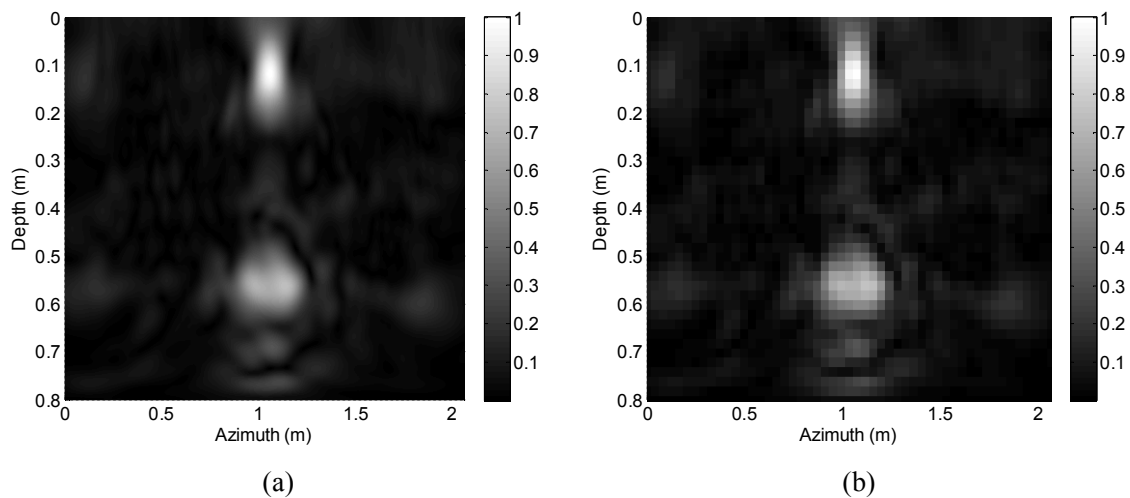
Fig. 4.7. The reconstructed GPR images by Fourier based SAR processing, using 100% pre-processed data. (a) Resolution 1x1mm. (b) Resolution 2x4cm

Compared to the layout of the pipes in Fig. 4.6, there is a small shift in the vertical position of the detected pipes. This difference is caused by some error in the estimated velocity of electromagnetic waves in the medium of propagation, which commonly occurs in GPR measurement. This condition can add more difficulties in CS processing. But in the next section, it is shown that CS is still able to detect the pipes with this condition.

4.4.4. CS Results with the Proposed Sampling Scheme and Algorithm

For CS processing, a lower resolution than that used in the aforementioned GPR profile was used. For better performance of CS, it is preferred that the target is represented by as few pixels as possible to maintain the high sparsity level of the problem. In this study, we chose a CS image pixel size of 2cm x 4 cm, where the vertical pixel size was about half the range resolution of the system and also smaller than the diameter of the pipes. Using this pixel size, the CS problem of a not-truly-sparse target can be simulated.

As a reference to judge the quality of the CS results, the conventional GPR image using the resolution of 2cm x 4 cm is shown in Fig. 4.7(b).

1. CS Results using the Proposed Data Acquisition Method and Algorithm
During the processing, OMP, CoSaMP and modified Bayesian RVM algorithms need the

information on the sparsity level S of the signal, which is not available in this case. In this simulation, the sparsity level is calculated from the known size of the target and the pixel size of CS image. By assuming the worst scenario where the target is located off-grid, as shown in Fig. 4.8, the two pipes should be represented by about 10 pixels in the CS image. Hence, $S = 10$ is chosen.
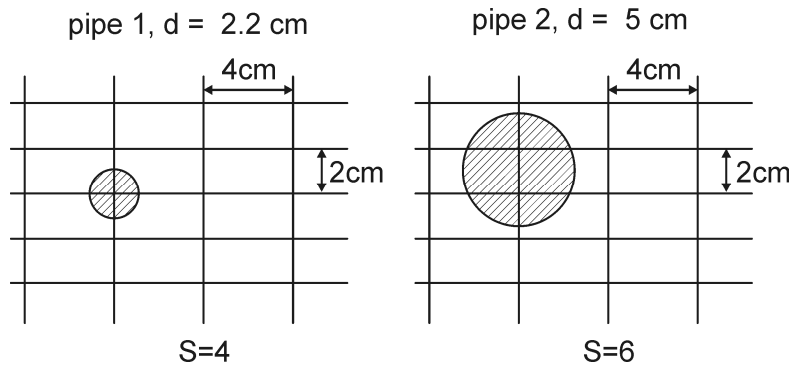
Fig. 4.8. The estimation of the sparsity level of the pipes. First pipe has S=4 and the second pipe has S=6, resulted in total S=10

Results with the 10% sample are shown in Fig. 4.9. Fig. 4.9(a) shows the reconstructed GPR image using the sampled measurement by Fourier based SAR Processing. Eventhough we use full frequency information and the number of spatial samples is still larger than the Nyquist criterion, we can see that the reconstructed image contains significant amount of noise and the target reflection is not focused.

CS algorithms are used to process the sampled measurement data, and the outputs are shown in Fig. 4.9(b)-(d). The targets are considered detected if some reconstructed pixels are grouped around the center position of the pipes and there is no pixel with significant amplitude reconstructed in another area. The results show that all four algorithms can successfully detect the two pipes in the GPR image.

The original Bayesian algorithm gives image which contains noise scattered over the scene. Compared to the original Bayesian algorithm, the modified Bayesian RVM shows the targets more clearly, reduces the reconstructed noise, and also reduces the processing time. The OMP algorithm also gives a clear image of the two targets, but compare to the other algorithms, it requires the longest processing time. CoSaMP algorithm gives clear image and the processing time is the shortest.
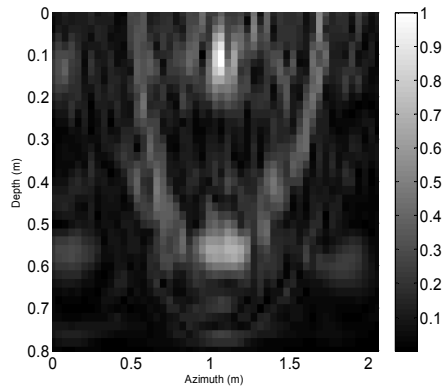
(a)
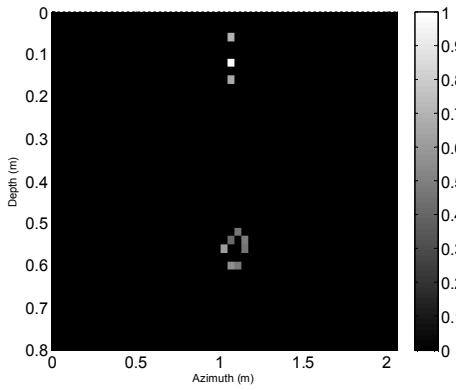
(b)
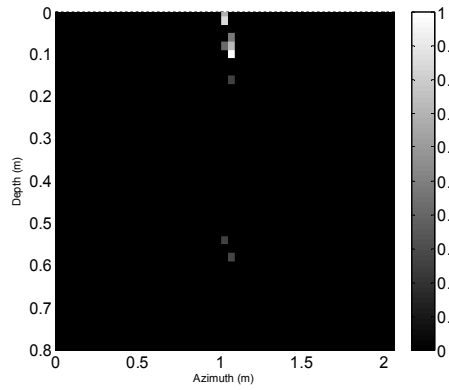
(c)
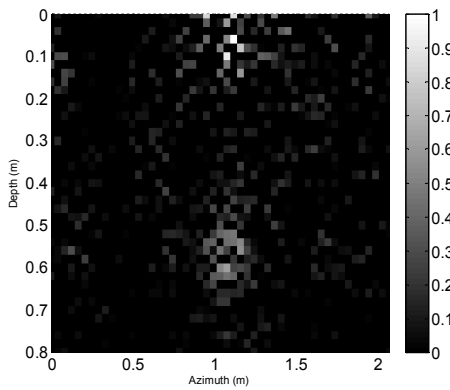
(d)
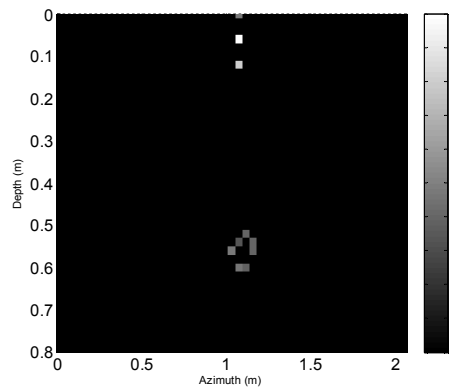
(e)

Fig. 4.9. The reconstructed GPR images using 10% sample by the proposed sampling scheme. (a) Conventional back projection method. (b) OMP, CPU time = 243.49s. (c) CoSaMP, CPU time = 0.50s. (d) Bayesian, CPU time = 94.26s. (e) modified Bayesian, CPU time = 0.70s

Table. 4.1. Performance of CoSaMP and Modified Bayesian

	CoSaMP	Modified Bayesian
Both 2 Targets Detected / 100 simulation	59/100	100/100
Only 1 Target Detected / 100 Simulation	41/100	0/100
Max CPU Time (s)	91.0s	2.7s
Min CPU Time (s)	0.4s	1.3s
Average CPU Time (s)	13.9s	1.5s

For the stability measurement, the performance of the two superior algorithms, i.e. CoSaMP and the modified Bayesian RVM, is further compared. Simulation was performed 100 times by selecting different samples in each run. The results are shown in Table. 4.1, where it can be seen that the Bayesian RVM can always detect both targets, while CoSaMP sometimes misses one target. This result shows that the performance of the proposed algorithm is more stable.

2. CS Results using Previously Proposed Data Acquisition Method

In this section, we will analyze the performance of the other sampling schemes shown in Fig. 4.5. By using sampling scheme in Fig. 4.5(a), we cannot perform background subtraction by simple mean averaging, because frequency information in each trace is located in different frequency. Without background subtraction, the ground reflection will be very strong and the target reflection will be hidden. Another background subtraction method using the sampled frequency data is available at [9], but is outside the scope of this study. However, eventhough the ground reflection removal can be removed using another method, this sampling scheme still have the same problem as the sampling scheme in Fig. 4.5(b), as explained below.

Using sampling scheme in Fig. 4.5(b), the pre-processing step in frequency domain, i.e. BPF and mean subtraction can be performed. But, the pre-processing in time domain, i.e. AGC and time gating, cannot be performed, because the full frequency information is not available. As the result, the reflection of the second target is very weak, and CS will not be able to detect it. Fig. 4.10(a) shows the result of CS using this sampling scheme by conventional SAR processing and Fig. 4.10(b) shows the CS result using the modified Bayesian RVM. This figures show only the reflection from the first target, while the second target is completely missed. This result confirms that the proposed sampling

scheme has better performance in detecting the target in a deeper location.

(a)	(b)
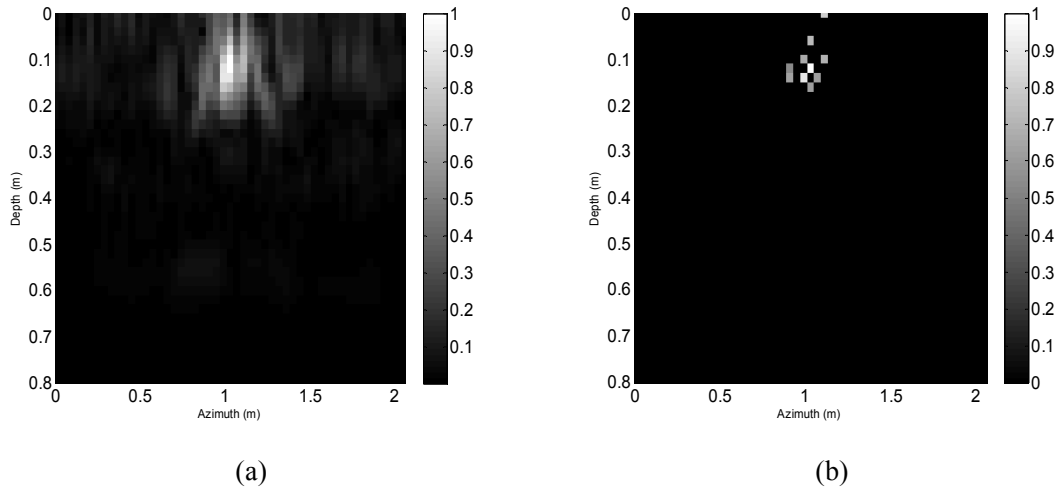
Fig. 4.10. The reconstructed GPR images using 10% sample by the sampling scheme in Fig. 4.5(b). (a) Conventional back projection method. (b) Modified Bayesian, CPU time = 1.19s

4.4.5. The Effect of Parameter Selection

The results presented showed that CS offers acceptable performance in detecting object under high clutter conditions. However, a new question arises, whether good results can be derived with some changes in CS parameters. For optimum performance of the CS system, the selection of some parameters should be more fully considered. Two parameters will be discussed: the pixel size and the number of samples.

A pixel size too small will result in a large matrix of α, and further requires longer CS computation time. If the pixel size is much smaller than the size of the target, the sparsity level of the problem will be reduced. On the other hand, using a large pixel size would reduce the resolution of the image. Fig. 4.11 shows the CS result using finer resolution, i.e., 1cm x 2cm. Since the sparsity level will decrease due to the finer resolution, in this processing we use $S = 20$. The result given in Fig. 4.11 shows that the Bayesian learning approach is still able to detect both targets with this resolution.
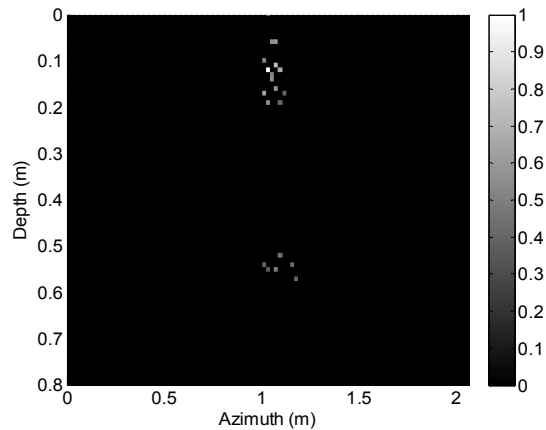
Fig. 4.11. CS result using 10% sample by modified Bayesian algorithm, resolution 1x2 cm, CPU time = 2.75s

It is known that more samples will give better results for the CS system. However, there are constraints on the data acquisition time and processing time that require us to choose as small a number of samples as possible without degrading the quality of the CS result. In this study, four simulations were conducted using 70, 40, 30, 20 and 10 observation points to show the effects on the CS result of reducing the measurement sample size. In each case, 40 frequency points were used. The simulation was repeated 100 times to show the stability of the simulated parameter. The probability of detection (POD) and the processing time are shown in Fig. 4.12. The figure clearly shows how fast the performance of CS degrades as the number of observation points is reduced.

The CS result in Fig. 4.12 shows that CS can still image the two pipes when the Nyquist sampling theorem is violated. The graphic shows that with about 26% of the required spatial-frequency data, using 37.7% of the required observation points, CS can still give good results with a probability of success higher than 70%.

In Fig. 4.12 the performance of CS using accurate propagation velocity is also presented. The accurate velocity in the medium was calculated from the known position of the target in the sand. Aside from the more accurate location of both pipes in the image, it is shown that CS performs better detection using accurate velocity, especially when the number of observation points is very small.
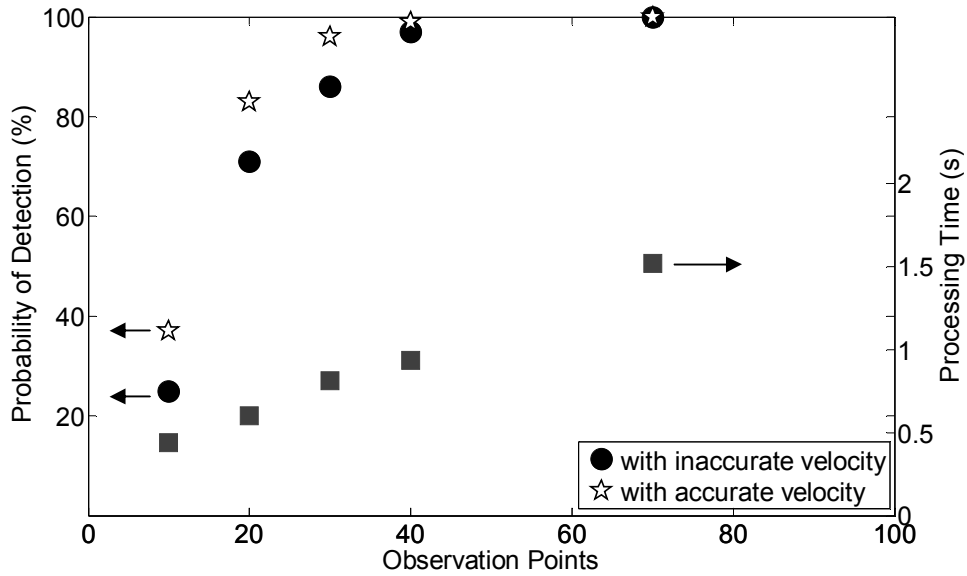
Fig. 4.12. POD and processing time as functions of the number of observation points in the data acquisition

4.5. Summary

In this chapter the implementation of CS for GPR imaging is evaluated. Due to the high level of clutter in GPR signal, pre-processing step is needed to remove most of the unwanted reflection from the signal. A data acquisition method is proposed to enable the pre-processing methods while reducing the number of observation points in the measurement. In the proposed data acquisition method, the full frequency information is measured at each selected observation points. This full frequency information is used for necessary pre-processing in frequency and time domain. Before CS processing the frequency data is downsampled to reduce the computation complexity in CS processing and also to maximize the incoherency between the sampling matrix and the representation matrix.

A CS algorithm which is modified from Bayesian RVM algorithm is also proposed, with the limited application on the detection and localization of specific subsurface object with known size and quantity. This algorithm is shown to have more stable performance then the other greedy CS algorithms. The proposed algorithm also has the short processing time, which makes it suitable for real time application of CS based GPR system.

5. Model Based CS Applied to Landmine Detection by GPR

5.1. Introduction

Landmine clearing is still an important issue in several places around the world. GPR is one of the techniques used to detect the buried landmine for the clearing purpose. In this chapter, we analyze the possibility to apply CS for landmine detection. In case of landmine detection, the landmines are usually spread over a very large area. Therefore, a smaller GPR measurement area only contains a small amount of landmine, which makes it a sparse problem that should be able to be solved by CS.

Chapter 4 has analyzed the implementation of CS for a detection of sparse subsurface objects by 1D GPR survey. For landmine detection by GPR, in order to recognize the reflection from landmine, a 2D survey is needed. In addition to its capability in reconstructing high resolution image, the implementation of CS to 2D GPR survey gives the following advantages:

1. For high resolution imaging, Nyquist criterion requires dense measurement data, which requires lot of work and time. For example, in GPR survey using frequency from 100 MHz to 6 GHz, in an area with wave velocity in the subsurface is 1.2 m/ns, Nyquist criterion requires 1 cm separation of data acquisition points. Therefore, to acquire subsurface image in 1m by 1m area, 100 B-scan need to be performed. A laboratory experiment with a positioner, requires about 8 hours to acquire all the data. By implementing CS, the amount of data needed can be reduced, and the data acquisition time can be shorten.

2. The GPR data needs to be located in a gridded location, with uniform separation between each data acquisition points. Without using mechanical positioner, it is almost impossible to acquire a very fine gridded data in real measurement. At present, there are many GPR systems that use accurate positioning system to record the data acquisition position. However, in signal processing, the data is interpolated to make a gridded data set. By using CS, the randomly acquired data can be directly used in CS processing for image reconstruction. The advantages of using CS system will more interesting for the survey of a rough terrain area. By using CS, the data

can be acquired in sparse positions and the difficult spot can be avoided.

This chapter presents the limitation of landmine detection by using conventional CS processing and proposed a solution by using model based CS. Laboratory and field experiments are used to evaluate the proposed algorithm.

5.2. Model Based CS-GPR for Landmine Detection

In landmine detection problem, there is an additional problem to CS image reconstruction caused by the size of landmine which is much larger than the resolution of the system. Thus, this problem is not a truly sparse problem. Experiments in this chapter show that CS processing may reconstruct artifacts in the GPR image where no target exists. It is also found that CS cannot accurately reconstruct the shape of the landmine, which can cause difficulty in recognizing the reflection of a landmine in real application. In order to acquire better CS image reconstruction, in this study we propose model based CS for landmine detection with GPR system.

Model based CS is originally proposed by Baraniuk *et al* [46]. Model based compressive sensing works by exploiting the special characteristic of the signal to further increase the performance of CS system by reducing the number of degrees of freedom of a sparse signal by permitting only certain configuration of the large and zero/small coefficients [46]. It is shown in this study that the model based CS can reduce the number of measurements required to stably recover a signal and better differentiate true signal information from recovery artifacts, which leads to a more robust recovery.

The study in [46] gives two examples of signal structure that commonly found in the sparse signals: the tree structure and block sparse signals. The block sparse signal includes signal ensembles and signal with its large coefficients clustered together.

5.2.1. Block Sparse Model for Landmine

In this study, the implementation of CS for landmine detection using GPR system is presented. The landmine size is usually much larger than the resolution of GPR system, the landmine is represented by several pixels grouping together in the GPR image. For this case, the model based CS for block sparse signal is implemented.

[46] defines a block sparse signal as a signal vector $\boldsymbol{x} \in \mathfrak{R}^{JN}$, with J and N integers. This signal can be reshaped into a $J \times N$ matrix $\boldsymbol{X}$. Signal $\boldsymbol{X}$ in a block sparse model have entire columns as zeros or nonzeros. The measure of sparsity for $\boldsymbol{X}$ is its number of nonzero columns, which defines the block sparsity level (K) of the signal. Mathematically, [46] defines the set of K-*block sparse signals* as

$$S_K = \left\{ X = [x_1 ... x_N] \in \mathfrak{R}^{J \times N} \text{ such that } x_n = 0 \text{ for } n \notin \Omega, \Omega \subseteq \{1, ..., N\}, |\Omega| = K \right\}$$

(5.1)

Using this definition of block sparse signal, it is important to know how to divide the sparse signal so that the non-zero components will be grouped correctly and do not mixed with the zero components. However, in the case of GPR imaging, the exact location of the target is unknown. Therefore, it is difficult to divide the imaging area into blocks that would put the target exactly inside one block, eventhough the target size and the pixel size are known,

Fig. 5.1 shows an illustration of the blocking process in GPR imaging. Fig. 5.1(a) shows some part of two dimensional GPR image showing 18 pixels. Suppose a target is modeled by a 3x3 pixels cube. The model based algorithm requires that these 18 pixels are divided into 2 blocks of 3x3 pixels as shown in Fig. 5.1(b), then the block sparse set is defined in (5.3), with x_n is the pixel value at the *n*-th pixel:

$$\boldsymbol{x} = \left\{ x_1, x_2, ..., x_{18} \right\}$$

(5.2)

$$X^T = \left\{ \begin{matrix} x_1, x_2, x_3, x_4, x_5, x_6, x_7, x_8, x_9 \\ x_{10}, x_{11}, x_{12}, x_{13}, x_{14}, x_{15}, x_{16}, x_{17}, x_{18} \end{matrix} \right\}$$

(5.3)

According to the definition of the block sparse given above, the target should be located exactly either in the first block given by the first column of X or in the second block given by the second column of X. Therefore, if the target is located in the middle of these two blocks, as shown in Fig. 5.1(c), the target cannot be perfectly represented by any block, which will be a problem during the model based CS processing.
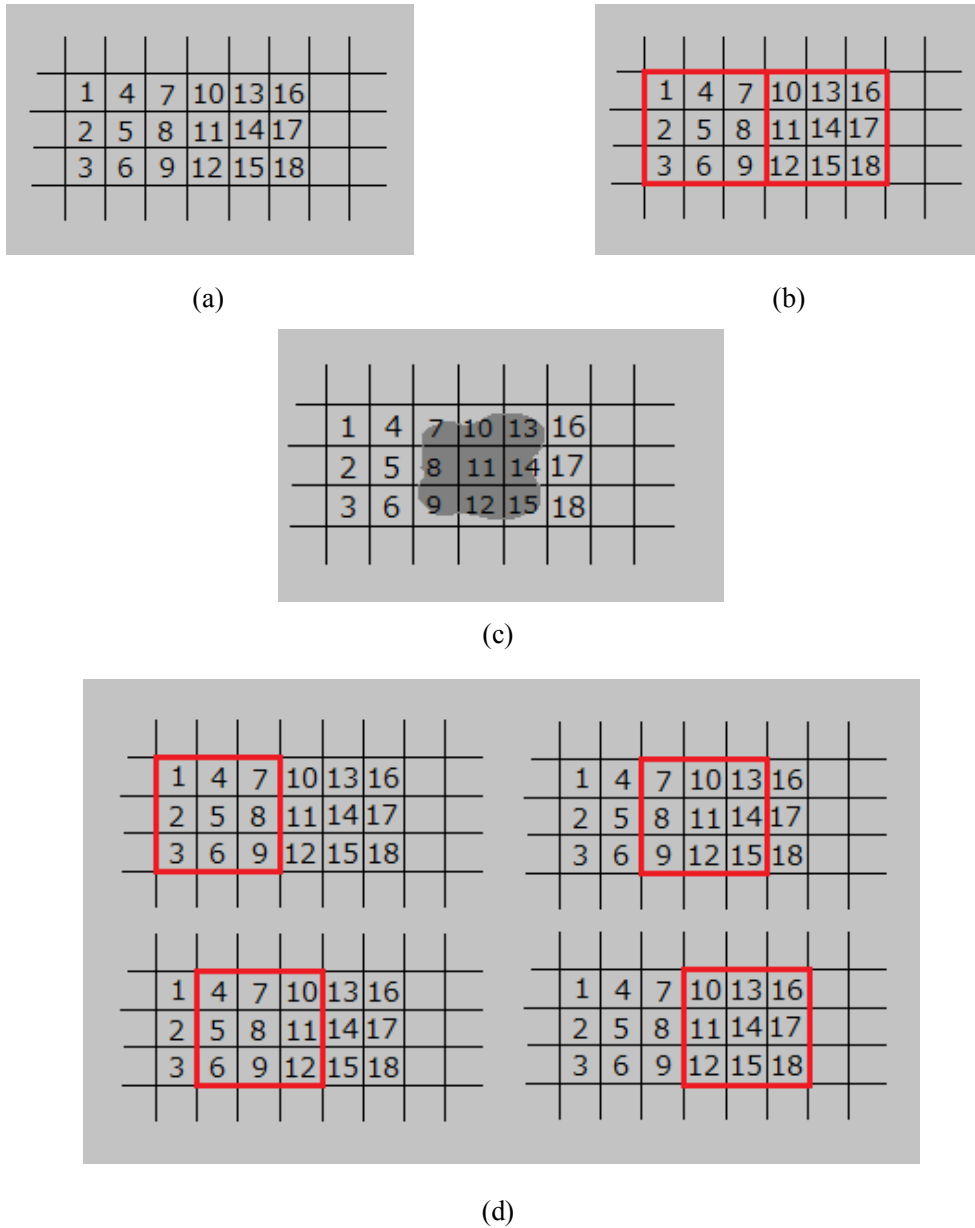
Fig. 5.1. Blocking process in GPR imaging by model based CS algorithm. (a) Some pixels in GPR image. (b). Blocking process in original algorithm. (c). Example of target position in GPR image, which can not perfectly defined by the blocks in original algorithm. (d) Proposed overlapped blocking process. The target in Fig. 5.1(c) can be represented by the second block.

In this study, we propose a blocking process where the blocks are overlapped each other, so that the accurate position of the target can be detected. This blocking process is shown in Fig. 5.1(d), which shows four overlapped blocks in the imaging area. In this case, the block sparse set is given by (5.4). By using this configuration, the target illustrated in Fig. 5.1(c) can be perfectly defined by the third column of the block set X.

$$X^T = \begin{Bmatrix} x_1, x_2, x_3, x_4, x_5, x_6, x_7, x_8, x_9 \\ x_4, x_5, x_6, x_7, x_8, x_9, x_{10}, x_{11}, x_{12} \\ x_7, x_8, x_9, x_{10}, x_{11}, x_{12}, x_{13}, x_{14}, x_{15} \\ x_{10}, x_{11}, x_{12}, x_{13}, x_{14}, x_{15}, x_{16}, x_{17}, x_{18} \end{Bmatrix} \qquad (5.4)$$

(a)

(b)

(c)
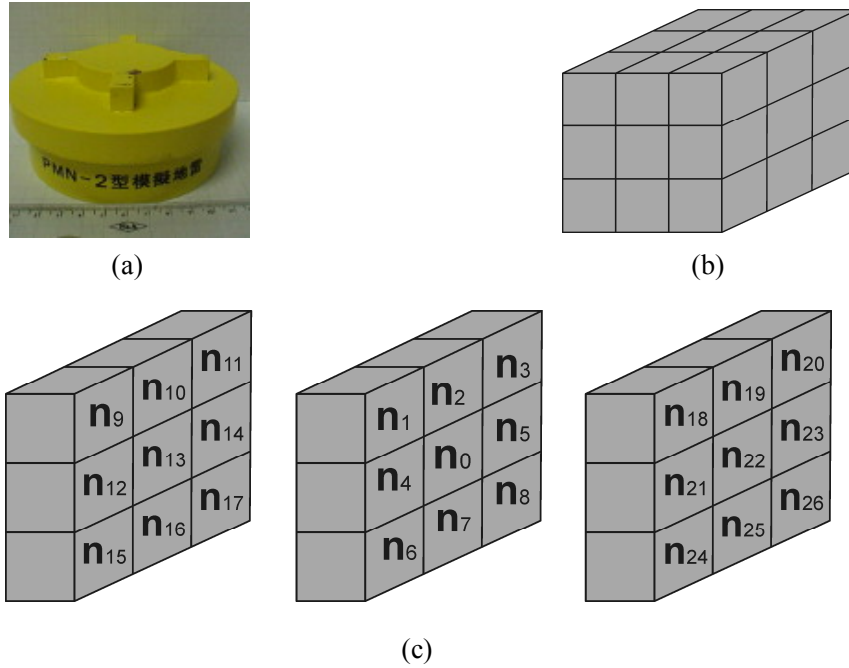
Fig. 5.2. Landmine and the landmine model used for model based CS processing. (a) PMN-2 landmine buried in the experiment site. (b) The 3x3x3 model of landmine. (c) The index of each pixel in the 3x3x3 landmine model

In this study on landmine detection, the purpose is to reconstruct a three dimensional GPR image. Ideally, the model should be the same size with the real size of the landmine, but in this study we will simplify the model to reduce the computation complexity. The landmine is modeled as a cube consists of 3x3x3 pixels grouping together, as shown in Fig. 5.2, with n_0 shows the index of the center pixel, and n_1 to n_{26} shows the index of surrounding pixels in three dimensional plane. Therefore, the member of each block can be written in (5.5). As shown in the example before, in the model based CS the whole three dimensional imaging area will be divided into several overlapped blocks. Therefore we do not need to know where the location of the target in the image. The blocks which contain the target will have highest signal proxy, and the blocks which partially contain

object can have lower signal proxy and can be eliminated from the CS solution using the known sparsity level during the CoSaMP processing.

$$\boldsymbol{Index} = \{n_0, n_1, n_2, ..., n_{26}\} \tag{5.5}$$

5.2.2. Model Based CoSaMP Algorithm

To find the CS solution, the model based CoSaMP as proposed in [37] is used. This algorithm is modified from the CoSaMP (Compressed Sampling Matching Pursuit) algorithm developed by Needell *et al* [31]-[32]. The structure shown in Fig. 5.2 is used in step 3 of the algorithm. The algorithm works on iteration as explained in the following steps:

1. Initialize residual $\boldsymbol{r} = \boldsymbol{y}$, $t = 0$, and $\boldsymbol{supp} = \varnothing$, with $\boldsymbol{supp}$ shows the location of nonzero components of $\boldsymbol{p}$.

2. Set $t = t + 1$ and calculate signal proxy for each pixel.

$$\boldsymbol{x}_p = \mathbf{A}^{\mathrm{T}} \boldsymbol{r}_{t-1} \tag{5.6}$$

3. Calculate signal proxy for each block structure, and derive the new supports by selecting 2*K* largest signal proxy, with *K* is a predefined block sparsity level.

$$\boldsymbol{x}_{pBlock}(n) = \sum\nolimits_{Index} \boldsymbol{x}_p \left(n \mid_{Index} \right) \tag{5.7}$$

$$\boldsymbol{x}_{pBlock}(n) = \boldsymbol{x}_p(n_0) + \boldsymbol{x}_p(n_1) + ... + \boldsymbol{x}_p(n_{26}) \tag{5.8}$$

$$\lambda_t = \mathrm{supp}\left(\boldsymbol{x}_{pBlock(2K)} \right) \tag{5.9}$$

4. Merge support with the previously estimated support from last iteration.

$$\boldsymbol{supp}_t = \boldsymbol{supp}_{t-1} \cup \lambda_t \tag{5.10}$$

5. Form signal estimate $\boldsymbol{b}$

$$\boldsymbol{b}_{(supp_t)} = \mathbf{A}_{supp_t}{}^+ \boldsymbol{y} \tag{5.11}$$

$$\boldsymbol{b}_{(supp_t)^c} = 0 \tag{5.12}$$

6. Prune signal estimate by selecting *K* largest component of $\boldsymbol{b}$

$$\boldsymbol{p}'_t = \boldsymbol{b}_{(K)} \tag{5.13}$$

7. Calculate the new residual

$$\boldsymbol{r}_t = \boldsymbol{y} - \mathbf{A}\boldsymbol{p}'_t \tag{5.14}$$

8. If the new residual satisfy the halting criterion, end algorithm. Otherwise, go to 2.

The halting criterion should be selected to find the optimal solution of the CS problem. The example of halting criterion is by checking the consistency of the solution given by two consecutive iteration, as shown in (5.15), with $EstSig(n)$ is the estimated sparse signal derived from the n-th iteration. This halting criterion will be used in most of the processing of experimental data in this chapter.

$$\text{Halting Criterion} = \frac{\left\| EstSig(n) - EstSig(n-1) \right\|}{\left\| EstSig(n) \right\|} \leq 5 \times 10^{-3} \qquad (5.15)$$

It is also important to note that in the model based CS algorithm, the block sparsity level K is required. In GPR imaging, the block sparsity level shows the estimation of the number of target exists in the imaging area.

5.3. Laboratory Experiment

5.3.1. Experimental Setup

A laboratory experiment is conducted to acquire a regular grid data to detect a PMN-2 landmine buried in dry sand. The experiment is conducted by performing data acquisition in a two dimensional plane. Two spiral antennas, separated by 9 cm, are used. The antenna movement is controlled by a mechanical positioner to acquire the perfectly regular grid data.

A vector network analyzer (VNA by Anritsu) was used to generate the step frequency signal and record the reflected signal. The SFCW signal uses a frequency range from 10 MHz to 6 GHz, with 137 frequency points and a 43.72 MHz frequency step. The data was collected on a flat ground surface at 61 observation points in x and y direction, with separation between two consecutive observation points is 1 cm. The total number of observation points in the two dimensional area is 3721 points.

Pre-processing including Bandpass filter, and ground surface reflection removal is performed before image reconstruction. The ground surface reflection removal is performed by mean subtraction, considering that the ground surface in the experiment is almost flat. Fig.5.3 shows one slice of GPR time domain traces after pre-processing in

the center of landmine position. It can be seen that the ground surface reflection has been successfully removed.
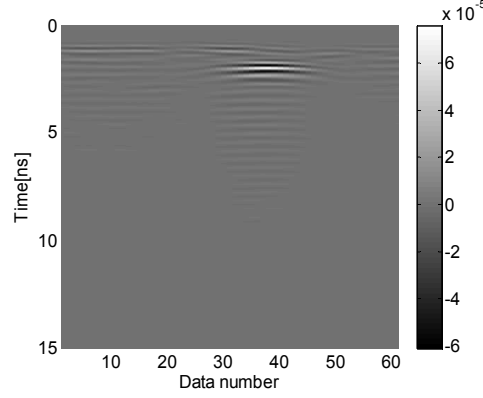

Fig. 5.3. 2D GPR time domain traces after pre-processing step in the center of landmine position

Before performing sampling for CS processing, the Nyquist criterion of spatial sampling for this experiment is calculated below :

$$\Delta x = \frac{\lambda_{\min}}{2} = \frac{v/f_{\max}}{2} = \frac{1.22 \times 10^8 / 6 \times 10^9}{2} = 0.01\,\mathrm{m} = 1\,\mathrm{cm} \qquad (5.16)$$

This result shows that the measurement setup is the same with the Nyquist criterion. To acquire a high quality GPR image, this requirement should be satisfied.

Before CS processing, the measurement data in spatial and frequency domain is sampled. In this study, 10% sampling is performed to the observation points, and 50% sampling to the frequency data. The total sample used is 5% from the full measurement data, with 372 random observation points and 69 random frequency data for each observation points.

For the GPR imaging, the pixel size of 1x1x1 cm is used. The diameter of a PMN-2 landmine is 12 cm and the height is 5 cm. Considering these two parameters, the landmine should be represented by about 12x12x5 pixels. Ideally, the model for model based CS should be the same with the size of the object. However, in this work we use a simplified landmine model of 3x3x3 pixels cube.

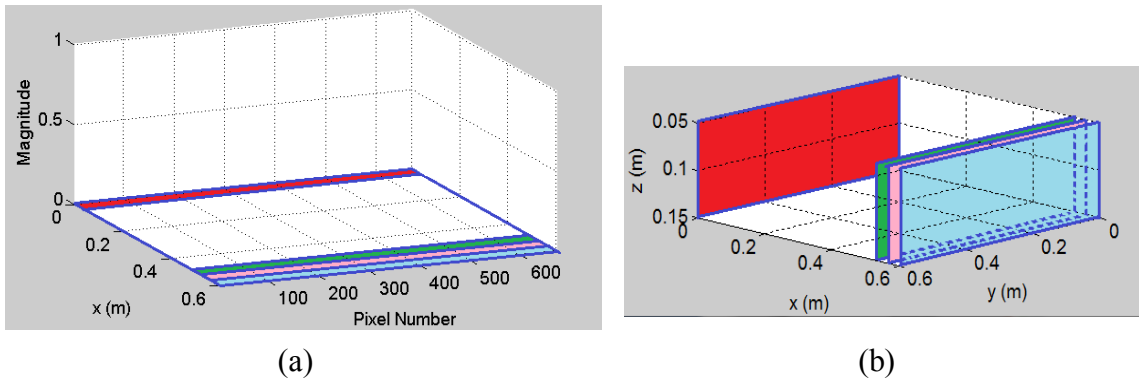(a)   (b)

Fig. 5.4. Two images used to evaluate the image reconstruction results. (a). Magnitude plot to show the magnitude of each pixel in each vertical slice. (b) 3D image showing pixels exceeding the threshold value

5.3.1.   Imaging Results

As in Chapter 3, to show the imaging results, the magnitude plot and three dimensional plot as shown in Fig. 5.4 are used. Fig. 5.5 shows the reconstructed GPR image using conventional full measurement with SAR processing. The reflection of landmine is visible at depth 12 cm, represented by several pixel grouping together in the three dimensional planes, as can be seen in the horizontal slice of GPR image in Fig. 5.5(c).

Fig. 5.6 shows the CS reconstruction of the GPR image by using 2% sample of data, with Bayesian RVM algorithm [41]-[44]. This algorithm does not need the knowledge about the sparsity of the signal, but it requires the rough estimation of the noise level in the measurement. The figure shows weak reflection around the location of the landmine, and there are several high magnitude peaks in other region where no target exists. These false detected peaks may give wrong interpretation during the real measurement.

(a)   (b)
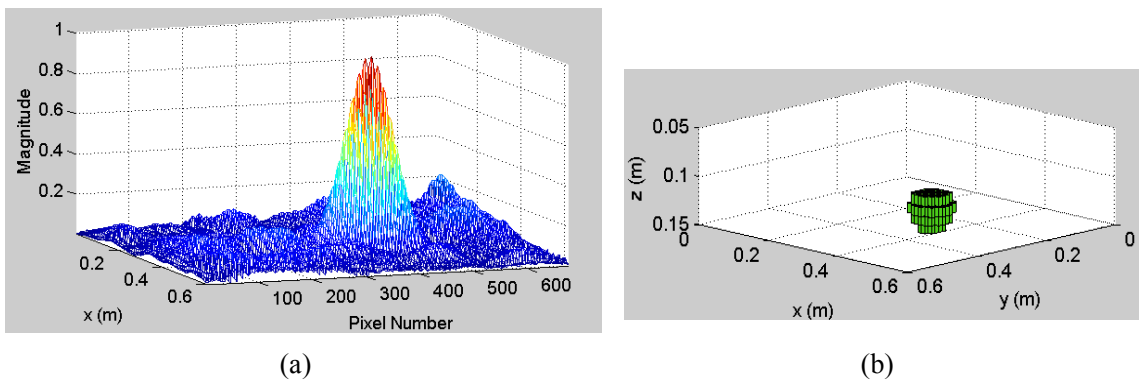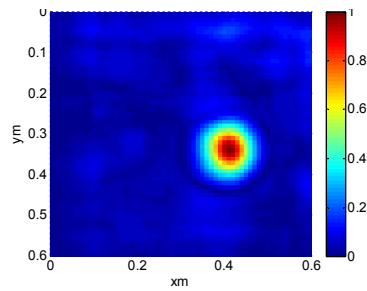
(c)

Fig. 5.5. The reconstructed landmine image using 100% data by Fourier Based SAR processing. (a) The magnitude of each pixel. (b) 3D image shows the location of landmine in the imaging area, imaging threshold = 0.5. (c) The horizontal slice at depth 12 cm.
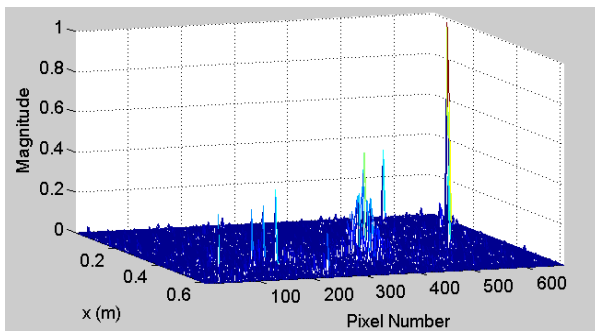
(a)   (b)

Fig. 5.6. The reconstructed landmine image using 10% spatial data by conventional CS processing (Bayesian RVM algorithm). (a) The magnitude of each pixel. (b) 3D image shows the location of landmine in the imaging area, imaging threshold = 0. This figure contains some high peaks in the wrong location.
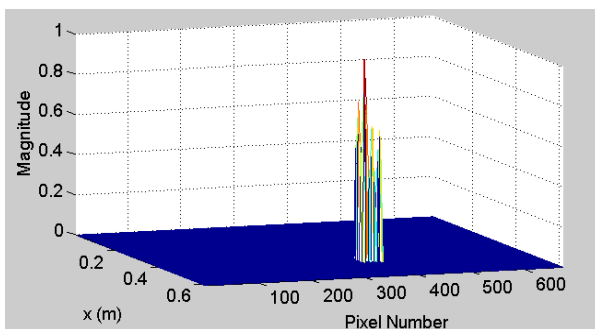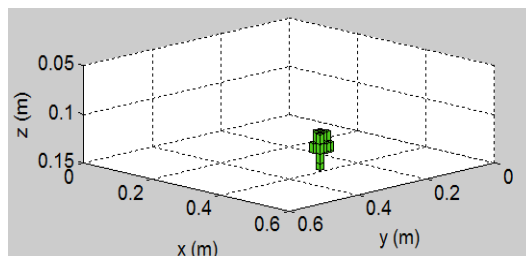
(a)   (b)

Fig. 5.7. The reconstructed landmine image using 10% spatial data by model based CS processing. (a) the magnitude of each pixel. (b) 3D image shows the location of landmine in the imaging area, imaging threshold = 0.
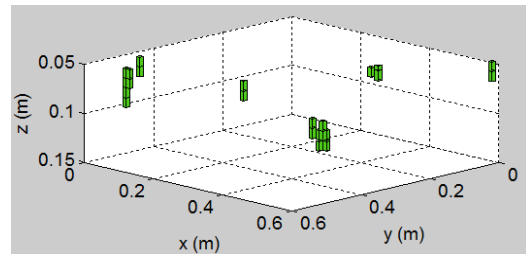
Fig. 5.7 shows the reconstructed GPR image using model based CS with the proposed model. In the model based CS processing, it is assumed that the block sparsity level K is known. Since only one landmine exists in the imaging area, then $K = 1$. Fig. 5.7 shows that eventhough the landmine model is much smaller than the size of the real PMN-2 landmine, the reflection of landmine is reconstructed at the correct position and there is no false detected peak in other locations. And compared to conventional SAR imaging shown by Figure 4, the GPR image reconstructed by model based CS contains less clutter and has better resolution. More importantly, this image is generated by using only 10% random spatial sample, which will contribute to reduce the data acquisition time significantly in the real measurement.

5.4.   Laboratory Experiment with Multiple Targets

This experiment is conducted to evaluate the performance of model based CS when multiple target is located in the imaging area. The effect of inaccurate estimation of the block sparsity level K is also observed.

5.4.1. GPR Experiment with Two Landmines

1) Experimental Setup

Fig. 5.8. GPR experiment configuration using two landmines as targets.

In the experiment, a GPR measurement is conducted to detect to two landmines buried in sand, as shown in Fig. 5.8. The data acquisition is performed in a two dimensional plane using mechanical positioner to acquire the perfectly regular grid data. Two spiral antennas, separated by 10 cm, are used. A vector network analyzer (VNA by Anritsu) is used to generate the step frequency signal and record the reflected signal. The SFCW signal uses a frequency range from 100 MHz to 6 GHz, with 591 frequency points and a 10 MHz frequency step. The data was collected on a flat ground surface at 101 observation points in x direction and 91 points in y direction, with separation between two consecutive observation points is 1 cm. The total number of observation points in the two dimensional area is 9191 points. Bandpass filter and mean subtraction is performed before the image reconstruction process. After the pre-processing, the reflection of the two landmines is clearly seen, as shown in Fig. 5.9.
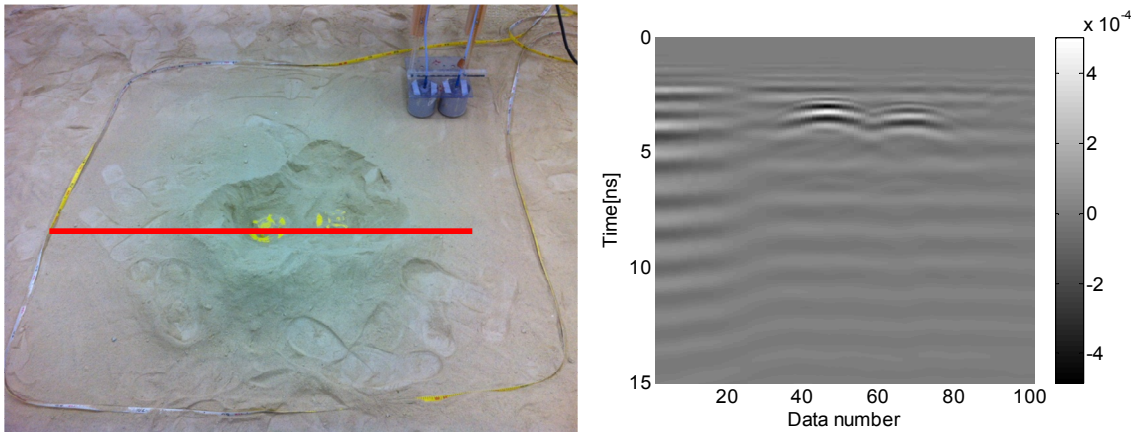
Fig. 5.9. 2D GPR time domain traces after pre-processing at position shown with the red line in the left figure

The same with the experiment in previous chapter, Nyquist theorem requires the separation between the observation points is 1 cm, which is the same with the measurement setup in this experiment. For CS processing, 7% sampling is performed to the spatial data, and 12% sampling to the frequency data, The total sample used is 0.84% from the full measurement data, with 372 random observation points and 69 random frequency data for each observation points.

In the experiment, the imaging results using two pixel sizes are compared. First, the pixel size of 1x1x1 cm is used, to show the imaging result using the same pixel size as the resolution of the GPR system. Second, the pixel size of 2x2x2 cm is used, to show the imaging result when the landmine model is more closely resembles the real landmine size.

2) Imaging Results

Fig. 5.10 shows the GPR image with pixel size 2x2x2 cm reconstructed by conventional SAR processing using 100% of the datasets. The reflection of two landmines are clearly seen, but there is clutter seen in other region in the three dimensional image.

(a)   (b)

Fig. 5.10. The reconstructed landmines image from the laboratory experiment with two landmines, using 100% data and pix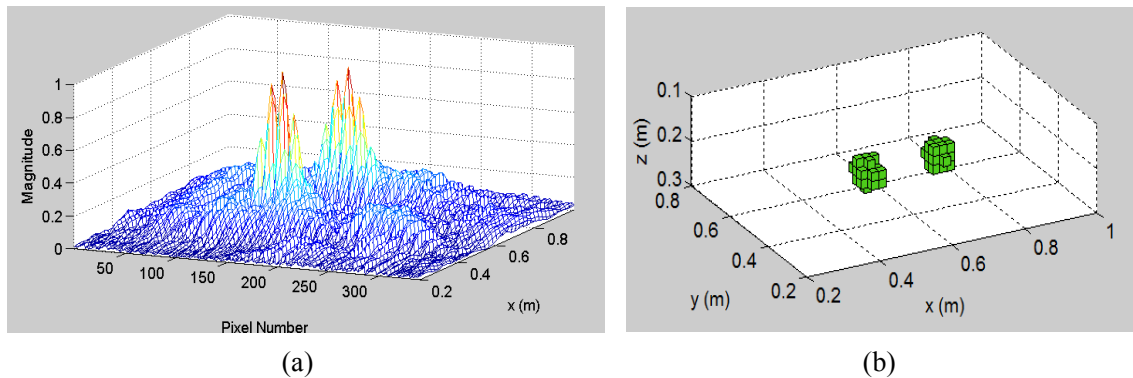el size 2x2x2 cm, by Fourier Based SAR processing. (a) The magnitude of each pixel. (b) 3D image shows the location of landmine in the imaging area, imaging threshold = 0.5

Fig. 5.11 shows the CS imaging result by using pixel size 1x1x1 cm, and Fig. 5.12 shows the CS imaging results using pixel size 2x2x2 cm. Using conventional CS by pixel size 1 cm, some high magnitude pixels are reconstructed around the location of the landmines. But since the location of these pixels is scattered, it is difficult to determine whether these pixels represents two large targets or some small targets. By pixel size 2 cm, some reconstructed pixels are grouping around the location of the landmines, which gives an impression that two large targets are exist, but in this image there are some high magnitude peaks also reconstructed in the false location.

Fig. 5.11(b)-(d) and Fig. 5.12(b)-(d) show the results of model based CS processing, with different estimation of the block sparsity level K. Since in this experiment, there are two landmines as target, then the K should be 2. In both figures, it is shown that the best imaging result is acquired by model based CS processing with $K = 2$, which gives two clear reflections of landmine in the correct position with less clutter in the other area. Model based CS with $K = 1$ also reconstruct two reflection of landmines, but one of the landmine appears to be smaller than the other. With $K = 3$, the reflection of the landmines become larger and the figures contain false detected peak in the other region where there is no target exist.

Fig. 5.11. The reconstructed images from the laboratory experiment with two landmines, using 7% spatial data, with pixel size 1x1x1 cm. (a) Conventional CS. (b) Model based CS with estimated block sparsity level $K = 1$, (c) $K = 2$, (d) $K = 3$. The 3D images use imaging threshold = 0
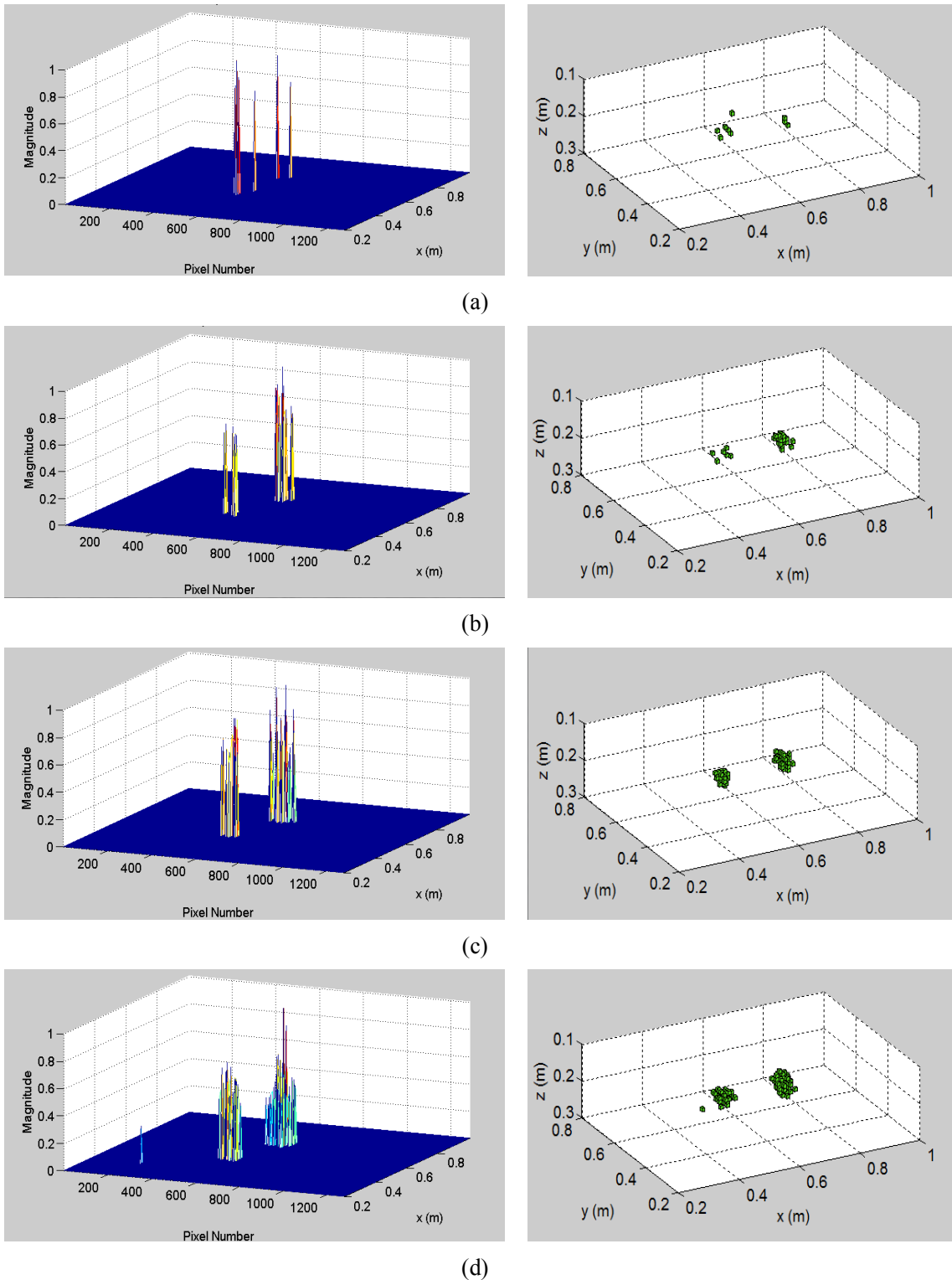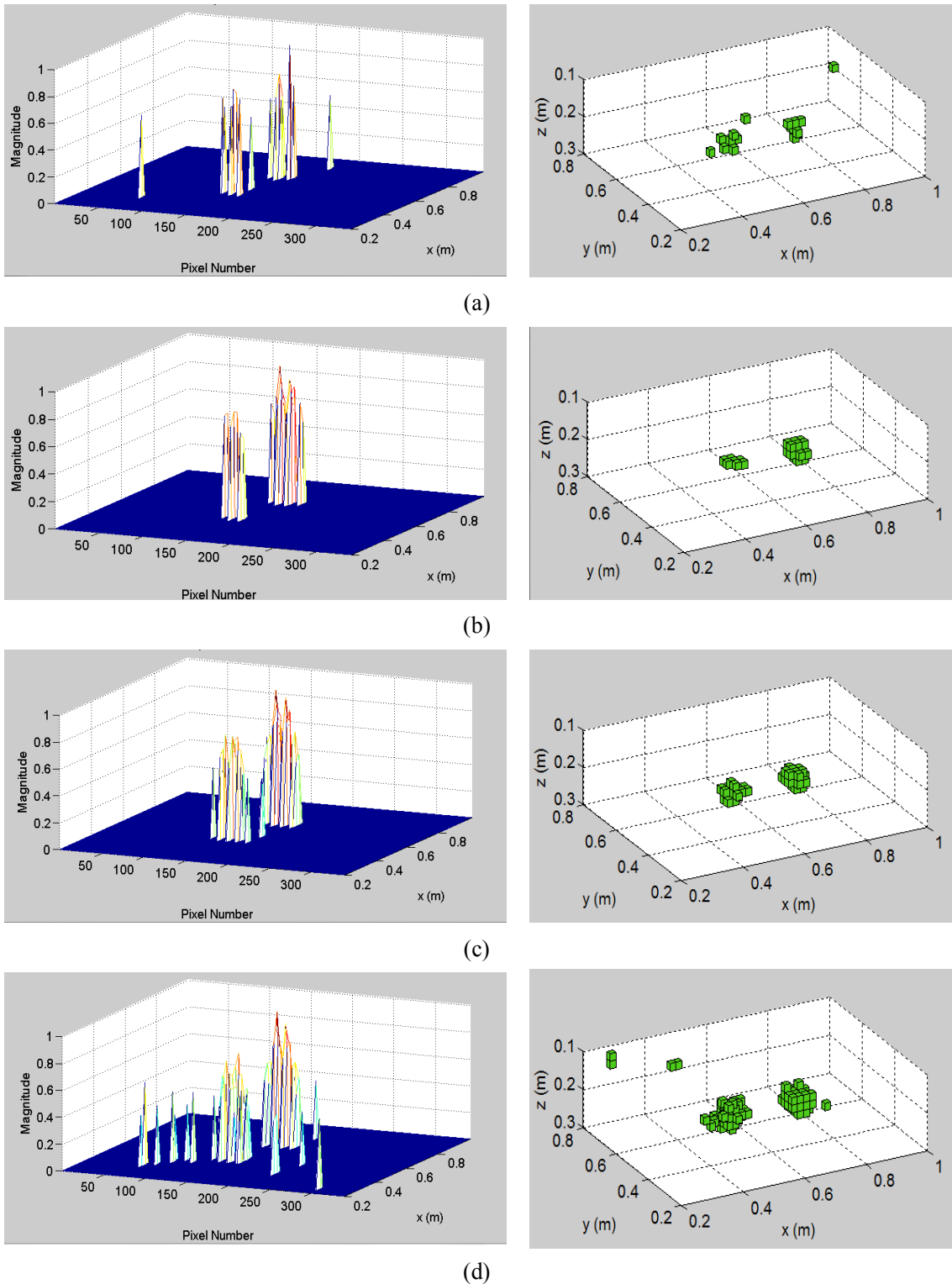
Fig. 5.12. The reconstructed images from the laboratory experiment with two landmines, using 7% spatial data, with pixel size 2x2x2 cm. (a) Conventional CS. (b) Model based CS with estimated block sparsity level *K* = 1, (c) *K* = 2, (d) *K* = 3. The 3D images use imaging threshold = 0

The processing time for each simulation is presented in Table. 5.1. It is shown that by using pixel size 2 cm, the model based CS algorithm can converge faster than by using pixel size 1 cm. The reason for this is because the size of the model is closer to the real size of the target, so that the algorithm can find the solution faster with less iteration.

From the results in this chapter, it is concluded that the accurate block sparsity level is important to acquire correct image reconstruction by the model based CS processing. And it is also noted that the model based CS algorithm will find solution faster if the size of the model closely resembles the real target.

Table. 5.1. Processing Time of Model Based CS by Different Parameters

	Pixel Size = 1 cm	**Pixel Size = 2 cm**
K = 1	Max iterations (1001)	6 iterations
K = 2	62 iterations	9 iterations
K = 3	59 iterations	14 iterations

5.4.2. GB-SAR Experiment with Five Metal Sphere

In order to evaluate the performance of model based CS when more targets exist in the imaging area, a GB-SAR experiment is conducted in laboratory. The experiment is performed using GB-SAR system to create more ideal condition, where there is no problem of ground surface reflection and inaccurate estimation of wave velocity in the processing.
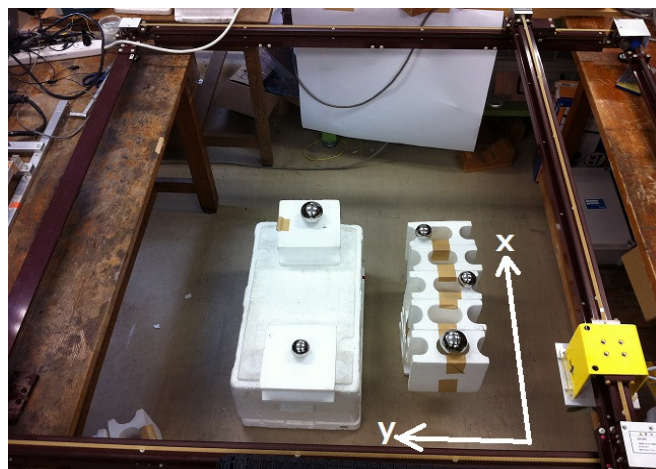
1) Experimental Setup

Fig. 5.13. GB-SAR experiment configuration with five spheres as targets

The experiment uses five metal spheres as targets, with the configuration shown in Fig. 5.13. Three metal spheres have a diameter of 3 cm and the other two have a diameter of 7 cm. Two Vivaldi antennas separated by 8 cm are attached to a *xy* positioner to scan an area of 80cm by 80 cm wide. The separation between two data acquisition points is 1 cm in both *x* and *y* direction. VNA is used to acquire SFCW radar data with frequency from 100 MHz to 6 GHz with 401 frequency points. Before image reconstruction, the GB-SAR data is pre-processed by bandpass filter. The antenna coupling and the reflection from the floor is also removed. After pre-processing, Fig. 5.14 shows that the data still contains significant amount of clutter, which come from the reflection from the frame of the *xy* positioner and also from the staggering position of data acquisition points at different scan lines.
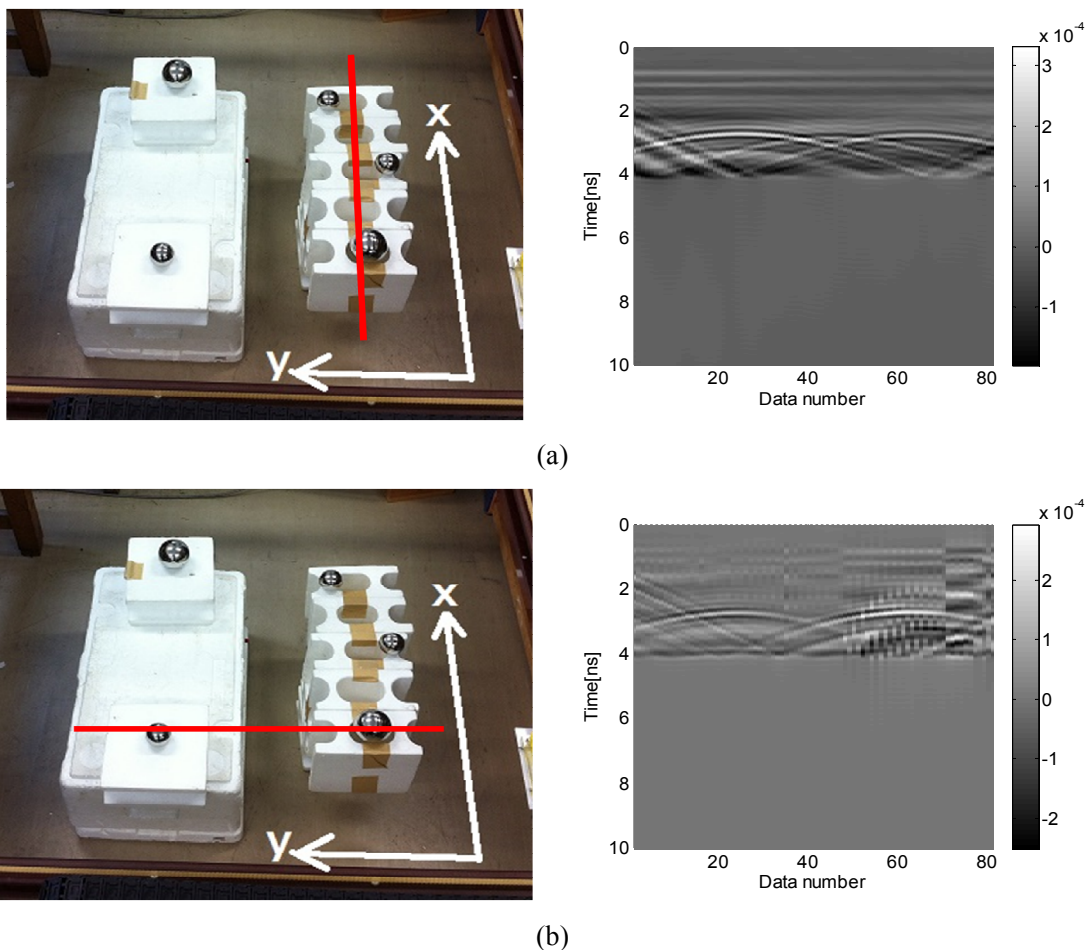

(a)

(b)

Fig. 5.14. 2D GB-SAR time domain traces at the position shown by a red line in the left figures. (a) 2D traces along *x* axis. (b) 2D traces along *y* axis

The Nyquist criterion requires separation between observation points is 2.5 cm. Therefore this experiment has satisfied the Nyquist requirement. For CS processing, 10% sampling is performed to the spatial data, and 25% sampling to the frequency data, The total sample used is 2.5% from the full measurement data, with 656 random observation points and 100 random frequency data for each observation points.

2) Imaging Results

(a)   (b)

Fig. 5.15. The reconstructed landmines image from the laboratory experiment with five metal spheres, using 100% data by Fourier Based SAR processing. (a) The magnitude of each pixel. (b) 3D image shows the location of landmine in the imaging area, imaging threshold = 0.5

Fig. 5.15 shows the reconstructed GB-SAR image by using conventional Fourier based SAR processing, using the pixel size 2x2x2cm. There are five groups of pixels with strong reflection in the image which represent the metal spheres. However, from the magnitude plot, it is shown that each metal sphere reflection has significant sidelobes. It is also shown that the other imaging area contains significant level of clutter.

(a)   (b)
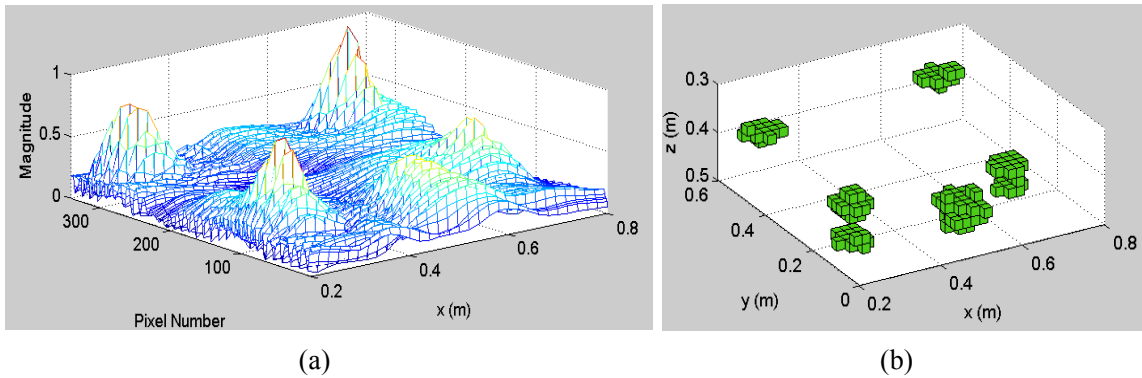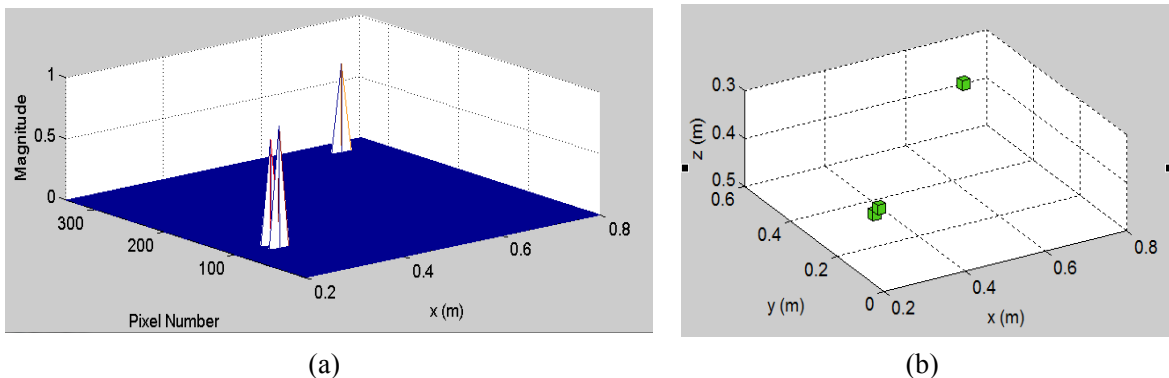
Fig. 5.16. The reconstructed landmines image from the laboratory experiment with five metal spheres, using 10% spatial data by conventional CS processing. (a) The magnitude of each pixel. (b) 3D image shows the location of landmine in the imaging area, imaging threshold = 0

Fig. 5.16 shows the imaging result by conventional CS processing using 2.5% of the measurement data. CS result can only reconstruct two metal spheres reflection, which come from the larger metal spheres with diameter 7 cm.

In the processing with model based CS, the model is modified to fit better with the size of the sphere. In this study, the sphere is modeled by 2x2x2 cube pixels, with each pixel has a size of 2x2x2 cm. It is observed in the processing, the model based CS algorithm is never converged for this five spheres experiment. Furthermore, it is noticed that two consecutive iterations may give very different result. To solve this problem, the halting criterion is reviewed. Fig. 5.17(a) shows the value of the halting criterion given in (5.15) in each iteration of model based CS processing for $K = 5$. This figure shows that the halting criterion value is not converged to zero.

In this five spheres experiment case, we define a different halting criterion based on the residue of signal at each iteration. The solution of model based CS is chosen when the signal residue reach the lowest value for the first time, as shown with a dashed circle in Fig. 5.17(b). Therefore, for $K = 5$, the estimated sparse signal after the second iteration is chosen as model based CS solution.

Halting Criterion

(a)
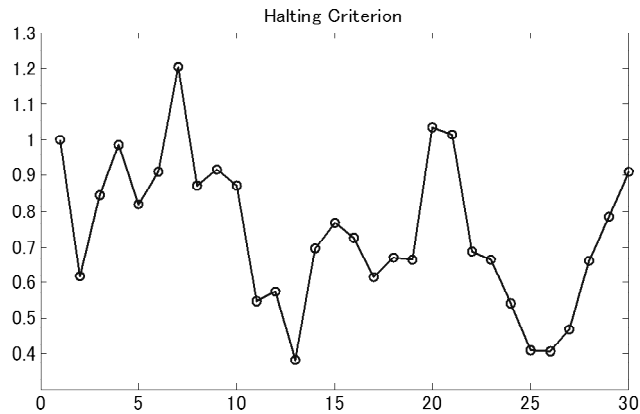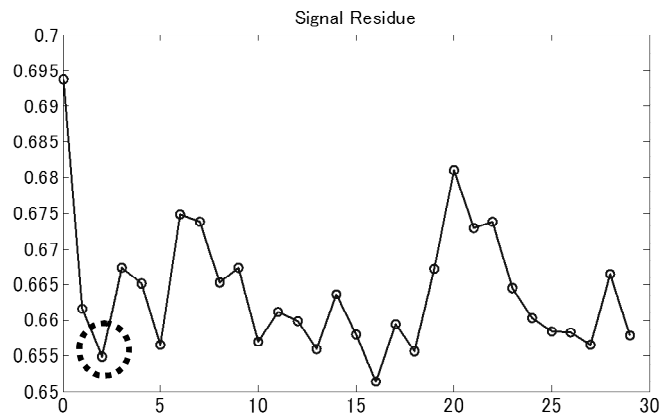
Signal Residue

(b)

Fig. 5.17. The halting criterion and the signal residual in model based CS processing of five spheres image reconstruction, with *K*=5. (a) Halting criterion value in each iteration. (b) Signal residual in each iteration

Fig. 5.18 shows the result of model based CS processing by using different estimation of the number of target (*K*), from 4 to 7. All these figures give an impression that there are five targets in the imaging area, however, the size of each reflection is increasing by the increase of *K*. From these imaging results, it is also noticed that the model based CS cannot be used to differentiate the size of the spheres, because the reconstructed image of each spheres does not represent the real size of each sphere.
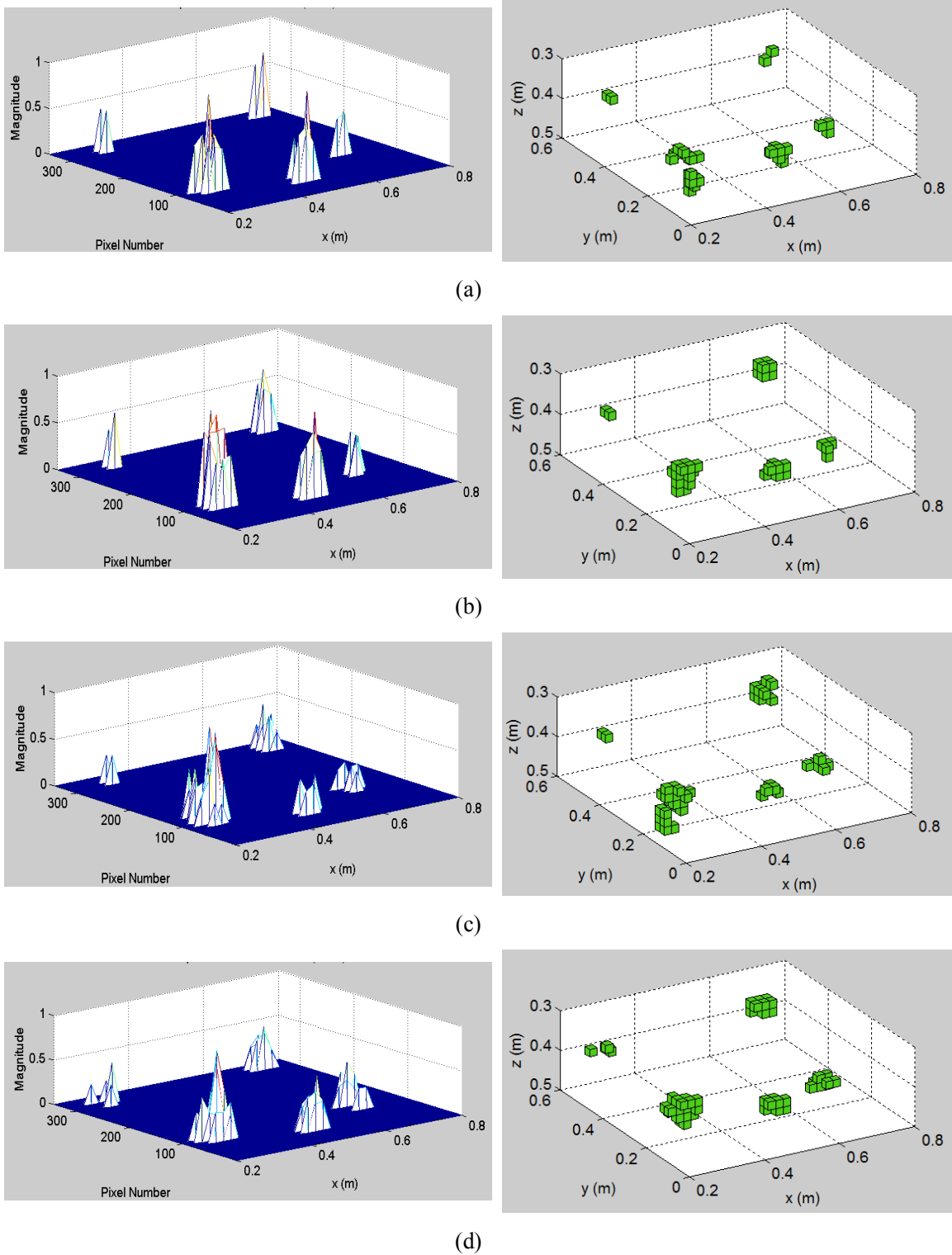
(a)

(b)

(c)

(d)

Fig. 5.18. The reconstructed images from the laboratory experiment with five metal spheres, using 10% spatial data, by model based CS processing, using different value of block sparsity level *K*. (a) *K*=4. (b) *K*=5. (c) *K*=6. (d) *K*=7. The 3D images use imaging threshold = 0

5.5. Evaluation Using Data Sets from a Real Landmine Field in Cambodia

5.5.1. Handheld GPR Sensor System

Metal detectors, which is an Electromagnetic Induction (EMI) sensor, has been widely used for humanitarian demining. However, in order to improve the efficiency of the demining operation, identification of buried landmines and discrimination for metal fragments by Ground Penetration Radar (GPR) is believed to be useful. Although there has been some approached to use unmanned vehicles for sensor scanning in mine fields, most of the mine fields are very small and hand-held sensors are more effective.

Due to very strong clutter from the ground surface and inhomogeneous soil to GPR, combined use of GPR with metal detector is more common approach, and this kind of sensor is normally referred as "Dual sensor" in humanitarian demining. A few dual sensor systems are now available for humanitarian demining in commercial basis. Tohoku University, Japan has been developing one of the dual sensor systems, namely, Advanced Landmine Imaging System (ALIS) since 2002 [47]-[52]. ALIS is unique in its novel technique of tracking the sensor position, even though it is scanned by hand by deminers. Then, ALIS can provide 3-D GPR image and it will help to understand the subsurface conditions much better than the conventional audio signal. It leads to the higher efficiency of detection of buried landmines. Two sets of ALIS have been operated at mine fields in Cambodia by CMAC 8Cambodian Mine Action Center) and more than 80 mines have been detected by ALIS.

An impulse GPR sensor system is equipped in ALIS. The antenna is scanned manually by an operator, as shown in Fig. 5.19. As a result, the scanning position is located randomly in two dimensional planes. In one scanning position, GPR system records the reflected wave and the CCD camera captures the image of the current scanning position. By using these information, the subsurface feature can be imaged. Fig. 5.20 shows the example of recorded random scanning position in a datasets acquired in a minefield in Cambodia on July 2009. The random and sparse scanning position gives disadvantages in the conventional GPR image processing. On the other hand, for CS processing, the random and sparse sampling gives benefits in achieving good imaging result.

Fig. 5.19. ALIS in operation in Cambodia [47]
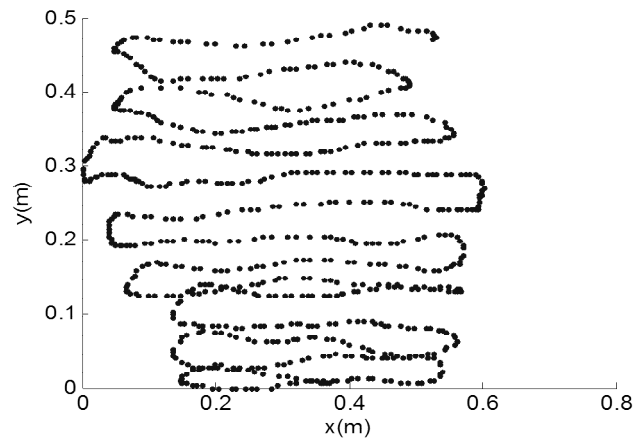
Fig. 5.20. Recorded scanning position in a field data acquisition using handheld GPR sensor system (ALIS)

Beside having an advantage in data acquisition method, by using the ALIS system the problem of estimating the value of K has been automatically solved by the utilization of metal detector (MD). The procedure of landmine detection using ALIS can be explained in the following steps. First, the deminar tries to find a single MD response by the sound. Then, the deminer scan the area using the handheld GPR system and perform signal processing. By following this procedure, the GPR image produced by ALIS system always has $K = 1$.

5.5.2. Measurement Setup and Pre-processing

The data used in this evaluation is one of the ALIS real data sets acquired in a real landmine field in Cambodia where a PMN-2 landmine is buried in sand. The GPR system used in the experiment is an impulse GPR type which acquires data in the time domain, while CS works with the frequency domain data. For this reason, CS processing cannot be directly applied to the raw time domain signal from the GPR system.

In this study, we follow the signal processing flow shown in Fig. 5.21. The raw time domain data from GPR system is transformed into frequency domain by FFT, but before that the time delay is removed from the data and the start and end of the signal is truncated by time domain windowing. The output of FFT is a frequency domain data which conventionally can be used in Fourier based SAR processing to generate the 3D image of subsurface feature. To simulate CS measurement system, the frequency domain data is sampled, both in spatial domain and frequency domain. This sampled data is used in CS processing to reconstruct the sparse information which shows the location of the landmine under the ground surface. The CS result will be compared to the conventional Fourier based SAR processing to investigate the accuracy of the CS reconstruction.

The GPR system acquired data from the total of 723 observation points, with the scanning position is shown in Fig. 5.20. The GPR system recorded time domain signal at each position in 512 samples. The time delay of the system is estimated to be 9.31 ns and is corrected before FFT. To avoid ringing in the resulted frequency domain data, the start and end of the time domain signal is truncated by using time domain windowing. After this step, FFT is performed using 1024 points FFT, with frequency range from 8.4MHz to 4.3GHz.
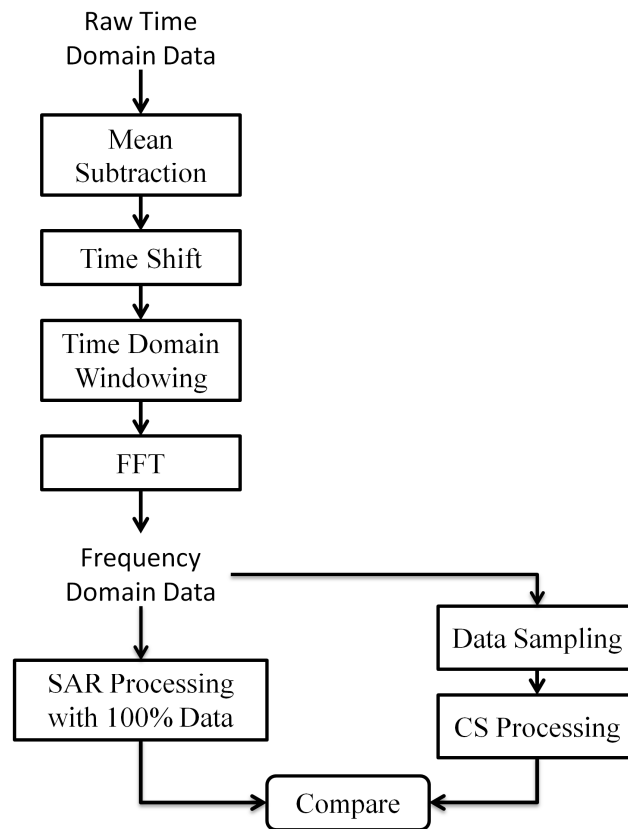
Fig. 5.21. Signal Processing Flow Chart

5.5.3.　Imaging Results

SAR processing using 100% frequency data gives the reconstructed 3D image as shown in Fig. 5.22. Compared to the experiment in chapter V and VI which use the dense and regular gridded datasets, the imaging result using conventional SAR processing gives wider sidelobes and higher level of clutter at all over the imaging area. However, the high reflection from the landmine can still be recognized in this image. This imaging result will be used as a reference to show the correct location of the landmine in the subsurface.

(a)   (b)

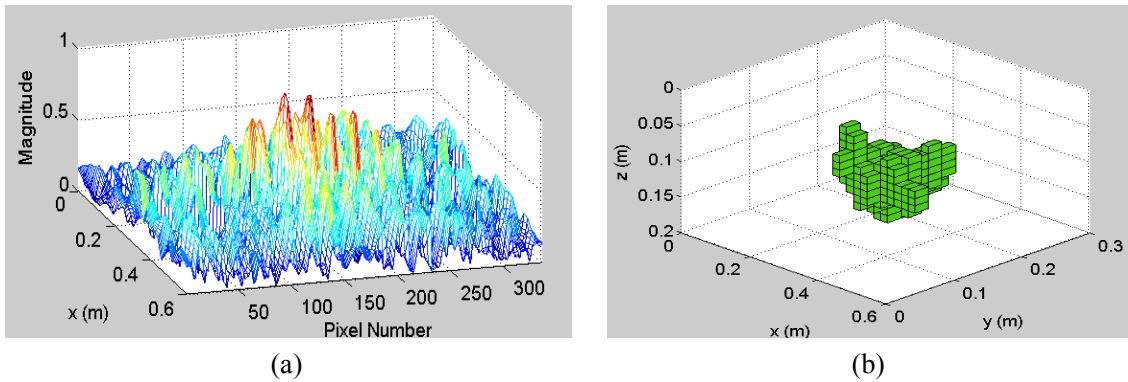**Fig. 5.22. The reconstructed landmine image from the ALIS datasets using 100% data by Fourier Based SAR processing. (a) The magnitude of each pixels. (b) 3D image shows the location of landmine in the imaging area, imaging threshold = 0.6**

CS is applied by first performing sampling process in spatial and frequency domain. 361 spatial positions (50% from the full spatial data) and 69 frequency points are randomly selected to be used in CS processing. Fig. 5.23 shows the reconstructed image using Bayesian Fast RVM. The result shows several reconstructed high magnitude pixels scattered in the three dimensional imaging area. Some of these pixels are located around the location of the landmine but some of the pixels located at the location where no target exists. Eventhough some of the pixels are located where the landmine is, the separated pixels can give confusion whether they come from an object as large as a landmine, or some three small targets scattered in that positions.

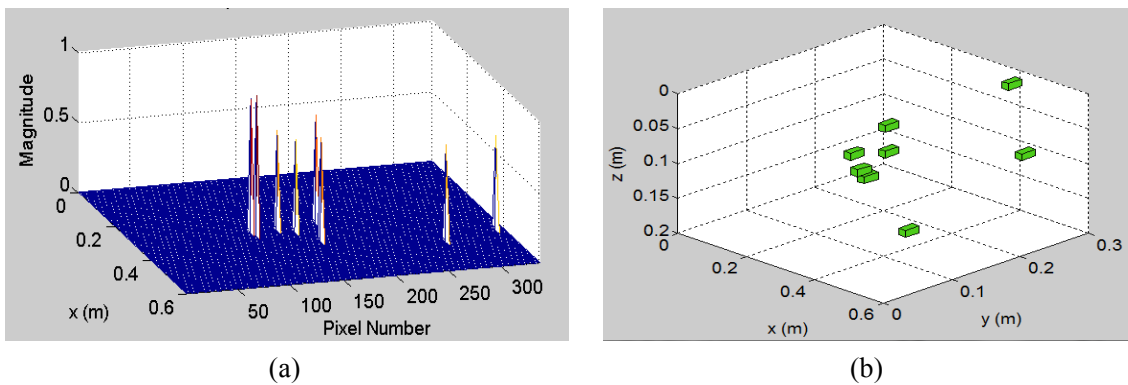(a)   (b)

Fig. 5.23. The reconstructed landmine image from the ALIS datasets using 50% spatial data by conventional CS processing (Bayesian RVM algorithm). (a) The magnitude of each pixel. (b) 3D image shows the location of landmine in the imaging area, imaging threshold = 0. This figure contains some high peaks in the wrong location.
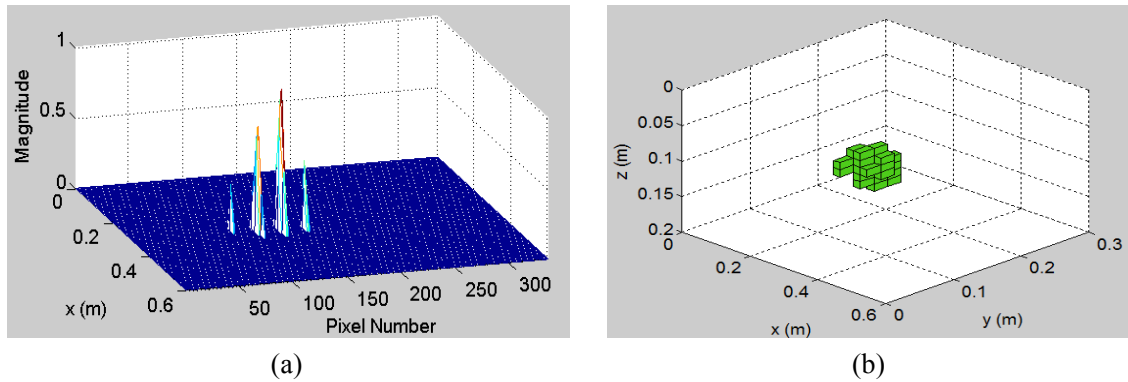
96

Fig. 5.24. The reconstructed landmine image from the ALIS datasets using 50% spatial data by model based CS processing. (a) The magnitude of each pixel. (b) 3D image shows the location of landmine in the imaging area, imaging threshold = 0.

Fig. 5.24 shows the imaging result using model based CS. In this GPR measurement, there is only one landmine buried in the sand, hence $K = 1$ is used. This result shows the reconstructed landmine reflection at the correct location. Compared to the conventional CS processing, the model based CS resulted in a compact reconstructed image of the landmine, which gives better perception about the buried target.

5.6.   Summary

In this chapter, the implementation of CS for a specific purpose of landmine detection is presented. Since a landmine size is much larger than the resolution of GPR system, conventional CS sometimes cannot give the accurate image reconstruction of the landmine. To improve the performance of CS system in landmine detection, a model based CS is proposed. Model based CS works by exploiting special characteristic of a signal. Landmine imaging by small pixel size has a block sparse structure, where several pixels with large values are grouping together. The algorithm is evaluated using several experiment datasets, and the results confirms that the model based CS can give better performance in landmine detection compared to the conventional CS.

6. Conclusions

The main purpose of the research presented in this thesis is to improve the implementation of Compressive Sensing (CS) for high resolution radar imaging, especially in GB-SAR and GPR imaging. The need for high resolution imaging using radar consequently increases the requirement for data density in the measurement. The conventional radar imaging requires that the Nyquist criterion is satisfied during the data acquisition, which resulted in long data acquisition time and a huge amount of data to process. Conventional focusing algorithm using Fourier based SAR processing which basically works based on matching filter, resulted in sidelobe around the target reflection that limits the resolution of the radar image. CS processing which works by exploiting the sparsity of the signal can give higher resolution radar image, by using much reduced measurement.

Chapter 2 presents the fundamental knowledge required in this research. The basic theory of CS is explained. The limitation of CS is described from two basic requirements in implementing CS, i.e. the signal sparsity and the sampling incoherency. Some examples are given to better understand how CS finds the solution by exploiting the sparsity of the signal.

Chapter 3 investigates the implementation of CS for the imaging using 2D-scan GB-SAR system. The representation matrix formulation and the sampling procedure for this application are described. It is confirmed in this chapter that by using CS processing, the higher resolution 3D GB-SAR image can be derived with much less measurement data than the conventional processing. This chapter discussed the use of convex programming to find solution in CS problem. The results show that convex programming requires accurate noise parameter to acquire a good imaging result. However, in the real measurement, this information is usually not available and is difficult to estimate correctly. The convex algorithm also requires long processing time which increases drastically with the increases of the number of data. Therefore, this algorithm is not suitable for the implementation on real time radar imaging.

Chapter 4 discusses the CS implementation for radar imaging using GPR system. Compared to GB-SAR system, the implementation of CS to GPR system is more challenging due to the high level of clutter in the GPR signal, attenuation problem,

ground surface reflection, and inaccurate estimation of the wave velocity in the medium. To improve the performance of CS based GPR imaging, a data acquisition method is proposed. The proposed data acquisition method has a main purpose to reduce the spatial sampling in the measurement. This proposal is based on the consideration that acquiring full frequency information by VNA can be completed in a very short time, usually in the order of millisecond. Furthermore, for imaging of shallow target, the required unambiguous time interval is short, which causes the required frequency sample in the measurement is small. Another concern is that the full frequency information can be used for signal processing to better reduce the unwanted components (e.g. ground surface reflection) and to mitigate the attenuation problem in the signal. Furthermore, reducing spatial sampling is considered more advantageous in reducing the data acquisition time in the measurement.

In chapter 4, some CS algorithm based on greedy procedure is discussed. The greedy algorithm works on iteration, and it is shown that the greedy algorithm can find solution faster than the convex programming with satisfying performance. In this chapter, a modified CS algorithm based on Bayesian learning is also proposed. This algorithm works in limited application for the detection and localization of a specific subsurface object with known size, because this algorithm needs a priori knowledge of the sparsity level of the signal. The processing of an experiment data shows that the proposed algorithm has a better and more stable performance with short processing time.

Chapter 5 discussed the implementation of CS to landmine detection. It is presented in this chapter that conventional CS cannot reconstruct the perfect shape of the target as large as the landmine which size is much larger than the resolution of the GPR system. This can cause difficulty in differentiating the reflection from a landmine with the reflection from other objects. It is also shown that conventional CS may reconstruct strong reflection in false area where no target exists.

A model based CS which works by exploiting the signal characteristic is proposed to improve the image reconstruction by CS especially for landmine detection case. The landmine is modeled as a group of several pixels with large values. Several laboratory experiments are presented to evaluate the performance of the proposed algorithm. The processing results show that the model based CS can give more accurate image reconstruction compared to the conventional CS processing. It is also shown that model based CS can still find solution when multiple target exist in the imaging area. However,

in this thesis the proposed algorithm cannot differentiate the size of each reflector in the imaging area. This problem can be a direction for a further development of this research topic.

Chapter 5 also presented the implementation of CS based imaging using handheld GPR system. This handheld system is one of the examples of a suitable data acquisition method for CS system, since this system directly acquires random and sparse data during the measurement. Besides, by using this system, it is easy to control the spread of data in 2D survey area. The utilization of this handheld system combined with model based processing has shown to give good imaging result in an experiment on landmine detection.

In this thesis, the model based CS presented in chapter 5 is modified from CoSaMP algorithm. However, it is found in chapter 4 that the modified Bayesian based algorithm has better and more stable performance than the CoSaMP algorithm. For further development, there is a possibility that the model based CS based on Bayesian learning may increase the performance of the CS based landmine detection.

7. References

[1] M.A. Davenport, M.F. Duarte, Y.C. Eldar, and G. Kutyniok, "Introduction to Compressed Sensing," in *Compressed Sensing": Theory and Applications,* Cambridge University Press, 2012.

[2] Candès, E. J., & Michael , W. B. (2008). *An Introduction to Compressive Sensing* (Vol. 24). *IEEE. Signal Process. Mag.*, vol. 25,no. 2, pp. 21–30, Mar. 2008.

[3] M.F. Duarte, M.A. Davenport, D. Takhar, J.N. Laska, T.Sun, K.F. Kelly, and R.G. Baraniuk, "Single-pixel imaging via compressive sampling," *IEEE Signal Processing Magazine,* 25(2) pp. 83-91, March 2008.

[4] M. Lustig, D. Donoho, and J. M. Pauly, "Sparse MRI: The application of compressed sensing for rapid MR imaging," *Magn. Reson. Med.*, vol. 58, no. 6, pp. 1182–1195, Dec. 2007.

[5] V.M. Patel, R. Maleh, A.C. Gilbert, R. Chellappa, "Gradient-based Image recovery methods from incomplete fourier measurements," *IEEE Trans. Image Process,* vol. 21, no. 1, pp. 94-105, 2012.

[6] W.U. Bajwa, J. Haupt, A.M. Sayeed, and R. Nowak, "Compressed channel sensing: A new approach to estimating sparse multipath channels," *Proc. Of the IEEE*, vol. 98, no. 6, pp. 1058-1076, Jun. 2010.

[7] C.R. Berger, S. Zhou, J. Preisig, and P. Willett, "Sparse channel estimation for muticarrier underwater acoustic communication: From subspace methods to compressed sensing," *IEEE Trans. Signal Processing,* vol. 58, no. 3, pp. 1708-1721, Mar.2010.

[8] R.G. Baraniuk and P. Steeghs, "Compressive radar imaging," in *Proc. IEEE Radar Conf.*, Boston, MA, Apr.2007, pp.128-133.

[9] N. Hayashi, "Broadband synthetic aperture radar for environment observation," Ph.D. dissertation, Graduate School of Environmental Studies, Tohoku Univ., Sendai, Japan, 2011.

[10] Sato, M., (2012), "Data Sampling Density and Image Reconstruction in Near Range Synthetic Aperture Radar," Korea-Japan EMT/EMC/BE Joint Conference (KJJC-2012), May 18-19, Seoul, Korea, pp. 257-260.

[11] A. Gaber, "High resolution subsurface image reconstruction using near-range synthetic aperture radar," Ph.D. dissertation, Graduate School of Environmental Studies, Tohoku Univ., Sendai, Japan, 2012.

[12] D. Donoho, "Compressed sensing," *IEEE Trans. Inf. Theory*, vol. 52, no. 4, pp. 1289–1306, 2006.

[13] E. Candes, J. Romberg, and T. Tao, "Robust uncertainty principles: Exact signal reconstruction from highly incomplete frequency information," *IEEE Trans. Inf. Theory*, vol. 52, pp. 489–509, 2006.

[14] R. Baraniuk, "Compressive sensing," *IEEE Signal Process. Mag.*, vol. 24, no. 4, pp. 118–121, Jul. 2007.

[15] Y.-S. Yoon and M. G. Amin, "Compressed sensing technique for high-resolution radar imaging," *Proc. SPIE*, vol. 6968, pp. 696 81A.1– 696 81A.10, May 2008.

[16] Q.Huang, L. Qu, B. Wu, and G. Fang, "UWB Through-Wall Imaging Based on Compressive Sensing". *IEEE Trans. Geosci Remote Sens.*, vol. 48, no.3, pp. 1408-1415, Mar.2010.

[17] E. Lagunas, M.G. Amin, F. Ahmad and M. Najar, "Joint wall mitigation and compressive sensing for indoor image reconstruction," *IEEE Trans. Geosci Remote Sens.*, vol. 51, no. 2, pp. 891-906, Feb.2013.

[18] F. Ahmad, M.G. Amin, "Through-the-wall human motion indication using sparsity-driven change detection," *IEEE Trans. Geosci Remote Sens.*, vol. 51, no. 2, pp. 881-890, Feb.2013.

[19] X. Zhu and R. Bamler, "Tomographic SAR inversion by L1 norm regularization—The compressive sensing approach," *IEEE Trans. Geosci. Remote Sens.*, vol. 48, no. 10, pp. 3839–3846, Oct. 2010.

[20] X. Zhu and R. Bamler, "Super-Resolution Power and Robustness of Compressive Sensing for Spectral Estimation With Application to Spaceborne Tomographic SAR," *IEEE Trans. Geosci. Remote Sens.*, vol. 50, no. 1, pp. 247–258, Jan. 2012.

[21] A. Budillon, A. Evangelista, and G. Schirinzi, "Three-dimensional SAR focusing from multipass signals using compressive sampling," *IEEE Trans. Geosci. Remote Sens.*, vol. 49, no. 1, pp, 488-499, Jan.2011.

[22] S. Xilong, Y. Anxi, D. Zhen, and L. Diannong, "Three-Dimensional SAR Focusing Via Compressive Sensing: The Case Study of Angel Stadium," *IEEE Geosci Remote Sens Lett,* vol. 9, no.4, pp. 759-763, July. 2012.

[23] J. Yang, J. Thompson, X. Huang, T. Jin, and Z. Zhou, "Random-frequency SAR imaging based on compressed sensing," *IEEE. Trans. Geosci. Remote Sens.*, vol. 51, no. 2, pp. 983-994, Feb.2013.

[24] L. Zhang, M. Xing, C.W. Qiu, J. Li, and Z. Bao, "Achieving higher resolution ISAR imaging with limited pulses via compressed sampling," *IEEE Geosci Remote Sens Lett,* vol. 6, no.3, pp. 567-571, July. 2009.

[25] L. Zhang, M. Xing, C.W. Qiu, J. Li, J. Sheng, Y. Li, and Z. Bao, "Resolution enhancement for inversed synthetic aperture radar imaging under low SNR via improved compressive sensing," *IEEE. Trans. Geosci. Remote Sens.*, vol. 48, no. 10, pp. 3824-3838, Oct.2010.

[26] H. Wang, Y. Quan, M. Xing, and S. Zhang, "ISAR imaging via sparse probing frequencies", *IEEE Geosci Remote Sens Lett,* vol. 8, no.3, pp. 451-455, May. 2011.

[27] Y. Yu, A.P. Petropulu, and H.V. Poor, "MIMO radar using compressive sampling", *IEEE J, Sel. Topics Signal Process.,* vol. 4, no. 1, pp. 146-163, Feb.2010.

[28] Y. Yu, A.P. Petropulu, and H.V. Poor, "Measurement matrix design for compressive sensing-based MIMO radar", *IEEE J, Sel. Topics Signal Process.,* vol. 59, no. 11, pp. 5338-5352, Nov.2011.

[29] C.Y. Chen, and P.P. Vaidyanathan, "Compressed sensing in MIMO radar", *Proc. 42nd Asilomar Conf. Signals, Syst. Comput.,* pp 41-44, Oct. 2008

[30] Y. Yu, A.P. Petropulu, and H.V. Poor, "CSSF MIMO RADAR: compressive sensing and step-frequency based MIMO radar". *IEEE Trans. Aerosp. Electron. Syst.*, vol. 48, no. 2, pp. 1490-1504, April. 2012.

[31] A. C. Gurbuz, J. H. McClellan, and W. R. Scott, "A Compressive Sensing Data Acquisition and Imaging Method for Stepped Frequency GPRs". *IEEE Trans. on Signal Process.,* vol.57, no. 7, pp. 2640-2650, July. 2009.

[32] A. B. Suksmono, E. Bharata, A. A. Lestari, A. G. Yarovoy, and A. P. Ligthart, "Compressive Stepped-Frequency Continuous-Wave Ground-Penetrating Radar". *IEEE Geosci Remote Sens Lett,* vol.7, no. 4, pp. 665-669, Oct. 2010.

[33] A. C. Gurbuz, J. McClellan, J. Romberg, and W. R. Scott, "Compressive Sensing of Parameterized Shapes in Images," in ICASSP, 2008, pp. 1949–1952.

[34] M.A.C. Tuncer, and A. C. Gurbuz, "Ground Reflection Removal in Compressive Sensing Ground Penetrating Radars". *IEEE Geosci Remote Sens Lett,* vol. 9, no.1, pp. 23-27, Jan. 2012.

[35] M.A.C. Tuncer, and A. C. Gurbuz, "Analysis of orthogonal matching pursuit based subsurface imaging for compressive ground penetrating radars," *Turk. J. Elec. Eng. and Comp. Sci.*, vol. 20, no. 6, 2012.

[36] M. Grant and S. Boyd, CVX: Matlab Software for Disciplined Convex Programming (Web Page and Software) , Dec. 2010. [Online]. Available : http://cvxr.com/cvx/

[37] S.G. Mallat and Z. Zhang. "Matching pursuits with time-frequency dictionary," *IEEE Trans. Signal Process.*, vol. 41, no. 12, pp. 3397–3415, Dec. 1993.

[38] J. A. Tropp and A. C. Gilbert. "Signal recovery from random measurements via orthogonal matching pursuit," *IEEE Trans. Info. Theory*, vol. 53, no. 12, pp. 4655–4666, Dec. 2007.

[39] D. Needell, "Topics in Compressed Sensing," Ph.D dissertation, Dept. Math., Univ. California, Davis, 2009.

[40] D. Needell and J. Tropp, "CoSaMP: Iterative signal recovery from incomplete and inaccurate samples," *Appl. Computat. Harmon. Anal.*, vol. 26, no. 3, pp. 301–321, May. 2009.

[41] M. E. Tipping and A. C. Faul, "Fast marginal likelihood maximization for sparse Bayesian models," in *Proc. 9th Int.Workshop Artificial Intelligence and Statistics*, C.M. Bishop and B. J. Frey, Eds., 2003 [Online]. Available: . http://citeseer.ist.psu.edu/611465.html

[42] A. C. Faul and M. E. Tipping, "Analysis of sparse Bayesian learning," in *Advances in Neural Information Processing Systems (NIPS 14)*, T. G. Dietterich, S. Becker, and Z. Ghahramani, Eds., 2002, pp. 383–389 [Online]. Available: http://citeseer.ist.psu.edu/faul01analysis.html

[43] M. E. Tipping, "Sparse Bayesian learning and the relevance vector machine," *J. Mach. Learn. Res.*, vol. 1, pp. 211–244, 2001.

[44] S. Ji, Y. Xue, and L. Carin, "Bayesian compressive sensing," *IEEE Trans. Signal Process.*, vol. 56, no. 6, pp. 2346–2356, June. 2008.

[45] Y.N. Tang, "*Investigation on Azimuth and Range Dependency of Ground-based Polarimetric SAR*," Master Thesis, Graduate School of Environmental Studies, Tohoku Univ., Sendai, Japan, 2010.

[46] R. G. Baraniuk, V. Cevher, M. F. Duarte, C. Hegde, "Model Based Compressive Sensing," *IEEE Trans. Inf. Theory,* vol. 56, no. 4, pp. 1982-2001, Apr. 2010

[47] M. Sato, "Deployment of GPR system ALIS for humanitarian demining in Cambodia," *Proc. 13th International Conference on Ground Penetrating Radar*, Lecce, Italy, June, 2010.

[48] X. Feng and M. Sato, "Hand-held GPR Imaging Using Migration for Irregular Data," *IEEE J. Sel. Topics Appl. Earth Observ. Remote Sens. (JSTARS)*, vol. 4, no. 4, pp. 799-803, Dec. 2011.

[49] X. Feng, M. Sato and C. Liu, "Subsurface Imaging Using a Handheld GPR MD System," *IEEE Geosci. Remote Sens. Lett.*, vol. 9, no. 4, July 2012.

[50] Sato, M., Yokota, Y. and Takahashi, K., "ALIS : GPR System for Humanitarian Demining and Its Deployment in Cambodia," *Journal of the Korean Institute of Electromagnetic Engineering and Science*", vol. 12, no. 1, pp. 56-62, 2012.

[51] Sato, M. "Dual Sensor ALIS Evaluation Test in Afghanistan, " *IEEE Geoscience and Remote Sensing Society Newsletter*, pp. 22-27, 2005.

[52] http://www.alis.jp/

Acknowledgements

Publications by Author

Conference Presentations:

1. R. Karlina, and M. Sato, "Compressive Sensing Applied to Imaging by Ground Based Polarimetric SAR," Proceedings of 2011 IEEE International Geoscience and Remote Sensing Symposium (IGARSS), Vancouver, Canada, pp. 2861-2864, July 2011. (Poster)

2. R. Karlina, and M. Sato, "Compressive Sensing for 2D Scan GB-SAR System," Proceedings of 1st International Workshop on Compressed Sensing Applied to Radar (CoSeRa), Bonn, Germany, May 2012

3. R. Karlina and M. Sato, "Line Structures Imaging Using CS-Based GB-SAR System," in GCOE Symposium, Sendai, Japan, 2012, pp. 261-262. (Poster)

4. R. Karlina and M. Sato, "Landmine Detection Using Model Based Compressed Sensing with GPR System," 128rd SEGJ Conference, Tokyo, Japan, 2013, pp. 147-150.

5. R. Karlina and M. Sato, "Compressive Sensing Applied for Handheld GPR Sensor System for Landmine Detection," Technical Meeting on Electromagnetic Theory, IEE Japan, Tokyo, Japan, 2013, pp. 39-44.

Journal Papers:

1. R. Karlina, and M. Sato, "Modified Bayesian Algorithm Implemented in Compressive Sensing Applied to Spatially Sampled GPR Measurement Under High Clutter Conditions", *IEEE Trans. Geosci Remote Sens.*, 2013 (under review)

2. R. Karlina, and M. Sato, "Model Based Compressive Sensing Applied to Landmine Detection by GPR", *IEEE Trans. Geosci Remote Sens.*, 2013 (submitted)